

UNIVERSITÀ DEGLI STUDI DI NAPOLI FEDERICO II

FACOLTÀ DI INGEGNERIA



Dottorato di ricerca in Ingegneria dei Materiali e
delle Strutture

Polyimide membranes for alcohols
dehydration: from basic aspects to
separation applications

Coordinatore

Ch.mo Prof. Domenico Acierno

Relatore

Prof. Giuseppe Mensitieri

Correlatore

Dott. Pellegrino Musto

Candidata

Ing. Mariangela Leo

XXIV ciclo - Triennio 2008-2011

Contents

1	Introduction	1
2	Infrared Spectroscopy	6
2.1	Fundamentals	6
2.2	Absorption in the infrared region	10
2.3	Quantitative analysis	13
2.3.1	Peaks separations: <i>curve fitting</i>	15
2.3.2	Two-Dimensional Infrared Correlation Spectroscopy.	16
2.3.3	Molecular interactions: spectral consequences	19
3	Materials and methods	22
3.1	PMDA ODA films preparation	22
3.2	Experimental setups and procedures	25
3.2.1	FTIR apparatus	25
3.2.2	Gravimetric balance	30
4	Methanol Diffusion in PMDA ODA: results	33
4.1	Analysis of IR spectra	34
4.2	Gravimetric tests	41
4.2.1	Comparison with IR	41

4.3	Two Dimensional Correlation Spectroscopy	42
4.4	IR spectra of methanol in CCl_4	46
4.5	Conclusions	49
5	Pervaporation And Vapor Permeation	53
5.1	Fundamentals	53
5.2	Flux Equations for PV and VP processes	56
5.3	Membranes and Membrane Modules for PV and VP	60
6	Bioethanol dehydration	66
6.1	Bioethanol	66
6.2	Conventional distillation	67
6.3	Membrane-based Processes	74
7	Thermally Rearranged Polyimides	79
8	Materials And Methods	84
8.1	Polymer Synthesis	84
8.2	Membrane Preparation	85
8.3	Characterization Techniques	87
8.3.1	Attenuated Total Reflectance Infrared Spectroscopy (FTIR- ATR)	89
8.3.2	Differential Scanning Calorimetry (DSC)	89
8.3.3	Thermogravimetric Analysis (TGA)	90
8.3.4	Wide Angle X-Ray Scattering (WAXS)	91
8.4	Experimental Setups and Procedures	92
8.4.1	Pervaporation tests	92

8.4.2	Stability tests	96
8.4.3	Liquid sorption tests	98
9	Results	100
9.1	Polyimides	100
9.1.1	Exposure effect on pervaporation properties	100
9.1.2	Exposure effect on chemical stability	106
9.1.3	Pure liquids sorption	107
9.2	TR Polyimides	107
9.2.1	Exposure effect on pervaporation properties	113
9.2.2	Exposure effect on chemical stability	113
9.2.3	Pure liquids sorption	116
9.3	Conclusions	118

List of Figures

2.1	Vibrational modes of the H_2O molecule.	9
2.2	OH stretching band shift	20
3.1	PMDA and ODA: reaction of condensation	23
3.2	FTIR spectrum of spin-coated polyimide films	24
3.3	Components of the FTIR cell.	25
3.4	Experimental apparatus scheme	26
3.5	Particular of the experimental apparatus	27
3.6	Quartz spring apparatus	31
4.1	FTIR spectra in the $4000, 400cm^{-1}$ range for the polyimide film in the dry state (red trace) and after equilibration at $a_{met} = 0.5$ (blue trace)	34
4.2	FTIR spectra in the $4000, 2700cm^{-1}$ range at different time intervals	35
4.3	FTIR spectra in the $1060, 960cm^{-1}$ range at different time intervals	36
4.4	Curve fitting of the O-H stretching frequency range	37
4.5	Absorbance of the ν_{OH} band: absorption and desorption kinetics . .	37
4.6	Absorbance of the ν_{CO} band: absorption and desorption kinetics . .	38
4.7	Fick's diagrams of ν_{OH} and ν_{CO} absorption bands	38

4.8	Fick's diagrams of ν_{OH} absorption band for all the activities	39
4.9	Calculated methanol diffusivity compared to water diffusivity in PMDA ODA	40
4.10	Gravimetric sorption curve at $a_{met} = 0.3$	42
4.11	Fick's diagrams of gravimetric sorption tests	43
4.12	Calibration curve of IR data	44
4.13	Spectroscopic isotherm of absorption	45
4.14	Gravimetric isotherm of absorption	46
4.15	2DFTIR synchronous spectrum for absorption and desorption test at $a_{met} = 0.6$ in the range $3800 - 2600cm^{-1}$	47
4.16	2DFTIR asynchronous spectrum for absorption and desorption test at $a_{met} = 0.6$ in the range $3800 - 2600cm^{-1}$	47
4.17	2DFTIR synchronous spectrum for absorption and desorption test at $a_{met} = 0.6$ in the range $1060 - 960cm^{-1}$	48
4.18	2DFTIR asynchronous spectrum for absorption and desorption test at $a_{met} = 0.6$ in the range $1060 - 960cm^{-1}$	48
4.19	Sorption dynamic of the components of the ν_{OH} absorption band . .	49
4.20	Desorption dynamic of the components of the ν_{OH} absorption band	50
4.21	IR spectra and fitting of methanol in CCL_4	50
4.22	Comparison between methanol in CCL_4 and in PMDA ODA	51
4.23	Methanol aggregate forms in CCL_4	52
4.24	Methanol aggregate forms in $PMDAODA$	52
5.1	Pervaporation and vapor permeation processes	54
5.2	Concentration polarization effect	56

5.3	Solution-diffusion theory	57
6.1	Ideal distillation system	68
6.2	Vapor/liquid equilibrium for ethanol-water system at atmospheric pressure	70
6.3	Low energy-consuming high grade hydrous ethanol distillation . . .	72
6.4	High grade anhydrous ethanol system.	74
6.5	Morphology of the pervaporation composite membrane.	76
6.6	Schema of a plate-and-frame module.	77
6.7	Schema of a spiral-wound module.	78
7.1	Thermal rearrangement process	81
8.1	Furnace used for thermal treatment	87
8.2	Heating protocol	87
8.3	Thermal Gravimetric Analyzer	91
8.4	Wide Angles X-Rays Scattering	92
8.5	Schema of pervaporation apparatus	94
8.6	Picture of pervaporation apparatus	94
8.7	Exposure cell	97
8.8	Schema of exposure cell: (1) cell bottom; (2) cell top; (3) clamp; (4) Viton gasket with 10 mesh screen; (5) 0 – 100 psig pressure gauge; (6) bleed valve; (7) relief valve	97
8.9	Picture of polymeric films before and after exposure	99
9.1	Polyimide membranes tested	101
9.2	Pervaporation results of polyimides before and after exposure	102

9.3	Exposure effect on selectivity of polyimide membranes	103
9.4	Exposure effect on water and ethanol permeabilities of BTDA ODA	103
9.5	Exposure effect on water and ethanol permeabilities of BPDA ODA	104
9.6	Exposure effect on water and ethanol permeabilities of KAPTON .	104
9.7	Exposure effect on water and ethanol permeabilities of PMDA ODA	105
9.8	WAXS results on KAPTON membrane	105
9.9	WAXS results on PMDA ODA membrane	106
9.10	TGA results on KAPTON before and after exposure	106
9.11	TGA results on BPDA ODA before and after exposure	107
9.12	Water sorption of polyimides	108
9.13	Ethanol sorption of polyimides	108
9.14	TGA evidences of thermal rearrangement of BPDA HAB	109
9.15	Mass loss during thermal rearrangement of BPDA HAB	111
9.16	Mass loss during thermal rearrangement of BPDA HAB	112
9.17	Permeability vs selectivity graph of BPDA HAB before exposure . .	112
9.18	Density change of BPDA HAB with thermal rearrangement	113
9.19	Pervaporation results of TR polyimides before and after exposure .	114
9.20	Exposure effect on selectivity of TR polyimides	114
9.21	Exposure effect on permeability of TR4504h	115
9.22	Exposure effect on permeability of TR5001h	115
9.23	Exposure effect on permeability of TR5001h	116
9.24	Exposure effect on chemical stability of TR 450	116
9.25	Exposure effect on chemical stability of TR 500	117
9.26	Water sorption of TR polyimides	117
9.27	Ethanol sorption of TR polyimides	118

9.28	Mass loss evidence of thermal rearrangement of APAF ODPA . . .	119
9.29	Termal rearrangement of APAF ODPA	119
9.30	Exposure effect on chemical stability of APAF ODPA TR 400 1h .	120
9.31	Exposure effect on chemical stability of APAF ODPA TR 450 15 min	120

List of Tables

2.1	Regions of the electromagnetic spectrum	7
4.1	Peaks in the synchronous spectrum in the range $3800 - 2600\text{cm}^{-1}$.	45
4.2	Peaks in the asynchronous spectrum in the range $3800 - 2600\text{cm}^{-1}$	46
6.1	Flux and selectivity of ethanol/water mixture through different homogeneous membranes. Feed: 90% ethanol, temperature: 70°C , membrane thickness= $50\mu\text{m}$	76
8.1	Polyimide membranes	88
8.2	Thermally rearranged membranes	88
9.1	Conversion grade estimated from TGA for BPDA HAB	110

Chapter 1

Introduction

Conventional separation techniques have high energy costs; replacing key portions of the process with membranes could provide energy savings. Current membranes suffer from both plasticization and degradation which negatively impact the membrane performance over time.

Polyimides belong to the class of high-temperature polymers with excellent chemical and mechanical properties [14] and superior film-forming properties. They are usually prepared by the so-called two-step method in which a diamine and a dianhydride are allowed to undergo condensation polymerization to form a polyamic acid precursor. Subsequently, the precursor is converted thermally or chemically to the final polyimide. In the past 20 years the polyimide family has become increasingly important in the separation membranes field due to its properties. The versatility of polyimide chemistry, easy synthesis, and simple modification can be a powerful tool for membrane scientists to tailor the polyimide molecular structure with desirable physicochemical properties and separation performance. Furthermore polyimide membranes with high water vapour permeability have attracted great interest for the dehydration of alcohols, especially those derived from biological sources (e.g., bioethanol from renewable biomass feedstocks) which are

usually rich in water. Many studies by several authors have identified polyimides as membrane materials with high separation factors for water/alcohol separations [30]. A very particular kind of polyimides are those aromatic containing ortho-positioned functional groups (e.g., -OH and -SH). They have been demonstrated to undergo a thermal rearrangement to polybenzoxazoles, a class of polymers with excellent thermal and chemical stability but difficult to prepare. These thermally rearranged (TR) polymers have recently shown promising separation properties, due to an unusual free volume distribution. Moreover, polybenzoxazoles and polybenzthiazoles synthesized from aromatic polyimides still exhibit chemically stable structures making them an interesting possibility for alcohol dehydration. The application of membrane-based processes like pervaporation and vapor permeation instead of conventional distillation for alcohol-water mixtures has attracted attention from the perspective of energy saving [26] and has been actively researched in recent years. Pervaporation and vapor permeation are similar separation processes [32] whose basic difference lies in the physical state of the feed side, which is a liquid in the former case and a vapor in the latter. The selective permeation of one of the components of the mixture through the membrane is a mass transfer process so the driving force is a chemical potential gradient. Taking into account that at equilibrium the chemical potential gradient of each component must be the same in all phases, it can be easily understood the similarity between pervaporation and vapor permeation. In pervaporation the chemical potential gradient is due to a vapor pressure difference across the membrane, whereas in vapor permeation it is due to a partial pressure difference. In both processes the permeate side is kept under vacuum in order to maximize the driving force across the membrane. Transport in pervaporation membranes occurs by the solution-diffusion mechanism [36].

Classic transport models [38] describe pervaporation as a three steps- process:

- sorption equilibrium between the liquid feed side and the membrane;
- diffusion through the membrane driven by the chemical potential gradient across the membrane;
- desorption into the vapor permeate side.

Physical-chemical interactions between the membrane material and the permeating molecules and not the relative volatility as in distillation, play a fundamental role [39]. Therefore pervaporation is governed by the chemical nature and the physical structure of the membrane, the physicochemical properties of the water-alcohol mixture to be separated and the permeant-permeant and permeant-membrane interactions.

The first part of this work aimed to the determination of the absorption and desorption kinetics of an alcohol (methanol) inside a commercial polyimide (PMDA ODA) and to the identification of the interactions with polymeric network. The understanding of the molecular mechanisms of diffusion can be helpful in designing the chemical structure of future polymers for optimal transport properties. The diffusion of methanol into polyimide films was studied by in situ FTIR spectroscopy, one of the most used techniques for studying and characterizing polymeric materials thanks to some features such as the high sampling rate and the high accuracy, especially appropriate for studying polymer-low molecular weight compounds transport phenomena. FTIR can be usefully used to study real time and 'in situ' the diffusion phenomenon. Several methods of spectral data analysis

were used, among which difference spectroscopy, least-squares curve fitting, 2D correlation spectroscopy. The results gave an insight into the molecular mechanism of diffusion in terms of number and population of penetrant species present in the system and with respect to the nature of the molecular aggregates.

The second part of this work was focused on the performance of some 'commercial' polyimides (similar to those used industrially) and of these new thermally converted hydroxy-containing polyimides as potential candidates for the production of pervaporation and vapor permeation membranes for alcohols dehydration. As said above, polybenzoxazoles and polybenzthiazoles synthesized from aromatic polyimides are chemically stable structures that have been shown to have both favorable separation properties and high chemical stability making them an interesting possibility for this separation. The work focused on synthesizing and characterizing a range of such polymers to assess their suitability for ethanol dehydration. Some polyimides (PMDA ODA and its commercial version KAPTON, BPDA ODA and BTDA ODA) and some TR polyimides (obtained from the polyimides ODPA APAF and BPDA HAB) were synthesized and studied as potential membranes for ethanol dehydration. The chemical and thermal stability of the two kinds of polymers was tested: the most aggressive conditions that the membranes would experience were simulated, and the potential hydrolysis of the imide rings was measured. Furthermore, the swelling behaviour of the two materials was analyzed: the swelling and plasticization of the membranes often result in a loss of selectivity. The membranes that showed good stability were tested in a pervaporation system: vapour permeation permeability and selectivity for ethanol and water were obtained for both TR polymers and 'commercial' polyimides.

The second part of the work was conducted at Center for Energy and Environ-

mental Resources, The University of Texas at Austin under the supervision of Dr. Benny Freeman.

Chapter 2

Infrared Spectroscopy

2.1 Fundamentals

Infrared (IR) spectroscopy is one of the most common spectroscopic techniques used by organic and inorganic chemists. The energy of a molecule consists of translational energy, vibrational energy and electronic energy [7]. For a first approximation these contributions can be considered separately. Electronic energy transitions give rise to absorption or emission in the ultraviolet and visible regions of the electromagnetic spectrum; pure rotation give rise to absorption and emission in the microwave and far infrared regions; molecular vibrations give rise to absorption bands in the infrared region. Simply, infrared spectroscopy is the absorption measurement of different IR frequencies absorbed by a sample positioned in the path of an IR beam. The main goal of IR spectroscopic analysis is to determine the chemical functional groups in the sample. Different functional groups absorb different characteristic frequencies of IR radiation.

Infrared radiation spans a section of the electromagnetic spectrum having wavenumbers from roughly 13000 cm^{-1} to 10 cm^{-1} , or wavelengths from 0.78 to $1000\text{ }\mu\text{m}$. It is bound by the red end of the visible region at high frequencies

Region	$\lambda[cm]$	$\bar{\nu}[cm^{-1}]$	$\nu[Hz]$
Ultraviolet			
far	$[1 \cdot 10^{-6}, 2 \cdot 10^{-5}]$	$[1 \cdot 10^6, 50,000]$	$[3 \cdot 10^{16}, 1.5 \cdot 10^{15}]$
near	$[2 \cdot 10^{-5}, 3.8 \cdot 10^{-5}]$	$[50,000, 26,300]$	$[1.5 \cdot 10^{15}, 7.9 \cdot 10^{14}]$
Visible	$[3.8 \cdot 10^{-5}, 7.8 \cdot 10^{-5}]$	$[26,300, 12,800]$	$[7.9 \cdot 10^{14}, 3.8 \cdot 10^{14}]$
Infrared			
near	$[7.8 \cdot 10^{-5}, 2.5 \cdot 10^{-4}]$	$[12,800, 4,000]$	$[3.8 \cdot 10^{14}, 1.2 \cdot 10^{14}]$
middle	$[2.5 \cdot 10^{-4}, 5 \cdot 10^{-3}]$	$[4,000, 2,000]$	$[1.2 \cdot 10^{14}, 6 \cdot 10^{12}]$
far	$[5 \cdot 10^{-3}, 1 \cdot 10^{-1}]$	$[200, 10]$	$[6 \cdot 10^{12}, 3 \cdot 10^{11}]$
Microwave	$[1 \cdot 10^{-1}, 1 \cdot 10^2]$	$[10, 0.01]$	$[1 \cdot 10^{12}, 3 \cdot 10^8]$

Table 2.1: Regions of the electromagnetic spectrum

and the microwave region at low frequencies. IR absorption positions are generally presented as either wavelengths (λ), or frequency (ν) or wavenumbers ($\bar{\nu}$). Wavenumber defines the number of waves per unit length. Thus, wavenumbers are directly proportional to frequency, as well as the energy of the IR absorption. Wavenumbers and wavelengths can be inter converted using the following equation:

$$\bar{\nu} = \frac{\nu}{c/n} \quad \bar{\nu} = \frac{1}{\lambda} \quad (2.1)$$

where c is the velocity of light in vacuum and c/n is the velocity of light in a medium whose refractive index is n . According to the quantum theory the energy of a photon E_p is given by:

$$E_p = h\nu \quad (2.2)$$

where h is Planck's constant. This photon energy may be absorbed or emitted by a molecule causing a change in the energy of the molecule of an amount ΔE_k . According to the principle of conservation of energy:

$$\Delta E_k = E_p = h\nu = hc\bar{\nu} \quad (2.3)$$

If the molecule absorbs energy, ΔE_k is positive and a photon is absorbed, while if the molecule loses energy ΔE_k is negative and a photon is emitted. In other words the wavenumber of the absorbed or emitted photon is equal to the change in the molecular energy term expressed in cm^{-1} . The detailed study of the interaction of the electromagnetic radiation with the matter permits to have a lot of information regarding the characteristics of the matter itself; in this sense the IR spectroscopy is a valuable analysis technique both qualitative and quantitative used for studying the composition and the structure of the matter. The atoms of a molecule vibrate around their equilibrium positions with characteristic vibrational frequencies; according to the principle of the quantization of energy when a radiation hits a molecule, only the frequencies correspondent to the natural frequencies of vibration will be absorbed. The analysis of the absorbed frequencies and the measure of the correspondent energy permit to identify the molecule and its shape (its symmetry). In the study of molecular vibrations one can start with a classical model of the molecule where the nuclei are represented by mathematical points with mass. The internuclear forces holding the molecule together are assumed to be similar to those exerted by massless springs which tend to restore bond lengths or bond angles to certain equilibrium values. If there are N atomic nuclei in the molecule, there will be a total of $3N$ degrees of freedom of motion for all the nuclear masses in the molecule, of which 3 are rotational, 3 translational and $3N - 6$ vibrational ($3N - 5$ if the molecule is linear). Among the $3N - 6$ vibrational modes the most important are:

stretching of the chemical bonds;

bending which is the change of the bond angles;

torsion which is the change of the torsional bond angles;

Figure 2.1 illustrates the vibrational modes of the H_2O molecule.

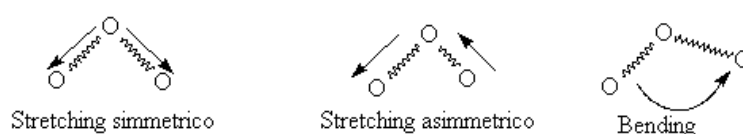


Figure 2.1: Vibrational modes of the H_2O molecule.

It can be shown that the $3N - 6$ internal degrees of freedom of motion of a non linear molecule correspond to $3N - 6$ independent normal modes of vibrations. In each normal mode of vibration all the atoms in the molecule vibrate with the same frequency and all the atoms pass through their equilibrium positions simultaneously. To describe the vibrational modes is necessary to solve the mentioned problem of classical dynamics which describes the molecule constituted by N atoms as a system with N masses hold together by massless springs. If the hypothesis of small vibrations around the equilibrium position holds, each couple of atoms can be considered as an harmonic oscillator. Thanks to the laws of the classical dynamics it is possible to calculate the frequencies of vibration of the atoms for each vibrational mode, by using parameters as the bond strength, the atomic mass, the geometry and the interactions with the other atoms. Once the vibrational frequencies are known, from quantum mechanics it is possible to obtain the energy associated with each vibrational mode (thanks to the so called analysis in normal coordinates). By considering each couple of atoms as a harmonic oscil-

lator, the vibrational modes (stretching, bending, etc) are linked to the quantized energy levels through the following relation:

$$E_{\nu_k} = \left(n_k + \frac{1}{2} \right) h\nu_k \quad (2.4)$$

where h is Planck's constant, ν_k is the vibrational frequency of the k th normal mode and n_k is the quantum number (or vibrational level) which values are only integer numbers.)

2.2 Absorption in the infrared region

In a spectrometer the molecule is irradiated with a whole range of infrared frequencies but is only capable of absorbing radiation energy at certain specific frequencies which match the natural vibration frequencies of the molecule itself, and these occurs in the infrared region of the electromagnetic spectrum. While the absorption frequency depends on the molecular vibration frequency, the absorption intensity depends on how effectively the infrared photon energy can be transferred to the molecule, and this depends on the *change in the dipole moment* that occurs as result of molecular vibration. The equality of the frequency of the radiation with that of vibration of the molecule, is not enough to cause the absorption of the infrared radiation: the so called *selection rules have to be satisfied*. The dipole moment is defined, in the case of a simple dipole, as the magnitude of either charge in the dipole multiplied by the charge spacing. In a complex molecule this simple picture can be retained if the positive particle represents the total positive charges of the protons concentrated at the center of charge of the protons, and the negative particle represents the total negative charge of the electrons concentrated

at the center of charge of the electrons. The center of charge of protons coincides with the center of gravity of the protons, and the center of charge of the electrons coincides with the center of gravity of the electrons. Since the wavelength of infrared radiation is far greater than the size of most molecules, the electric field of the photon in the vicinity of a molecule can be considered uniform over the whole molecule. The electric field of the photon exerts forces on the molecular charges and by definition the forces on opposite charges will be exerted in opposite directions. Therefore the oscillating electric field of the photon will exert forces tending to change the spacing between the proton and electron centers of charge, thereby tending to induce the dipole moment of the molecule to oscillate at the frequency of the photon. The more the dipole moment changes during a vibration, the more easily the photon electric field can activate that vibration. If a molecular vibration should cause no change in dipole moment then a forced dipole moment oscillation cannot activate that vibration. This is summarized in the selection rule that *in order to absorb infrared radiation, a molecular vibration must cause a change in the dipole moment of the molecule*. It can be shown that the intensity of an infrared absorption band is proportional to the square of the change in dipole moment, with respect to the the change in normal coordinate of the molecular vibration:

$$I_k = C \left[\frac{\partial^2 \mu}{\partial Q^2} \right] \quad (2.5)$$

where I_k is the k th vibrational mode of the molecule, C is a proportional μ is the dipole moment and Q is the direction of the mote (expressed in normal coordinates). If the dipole constituted by the two charges centers of symmetry of the total negative and positive charges, is made of a group of atoms highly polar with great difference in electronegativity, the the dipolar moment will be high in

magnitude as well as the IR absorption. It is straightforward that without the dipole moment there is no IR absorption. A simple rule is that high polar chemical bonds result in high IR absorption. That is why a polymeric chain made up mainly of C has a weak IR absorption, while its side groups like $C - H$, $C - F$, $C = O$ have a strong IR absorption, due to the high difference in electro negativity. Up to now we have been discussing only harmonic vibrations. Mechanical anharmonicity results if the restoring force is not linearly proportional to the nuclear displacement coordinate. Electrical anharmonicity results if the change in dipole moment is not linearly proportional to the nuclear displacement coordinate. If a vibration is mechanically harmonic, the classical picture of a plot of a nuclear displacement versus time is a sine or a cosine wave. One result of mechanical anharmonicity is that the vibrational frequency will no longer be completely independent of amplitude as it is in the harmonic case. If a plot is made of dipole moment versus time for a classical vibration, a periodic but non sinusoidal wave will result if either mechanical or electrical anharmonicity is present. However, any such periodic function can be resolved into simple sine or cosine components where the frequencies are integral multiples of the fundamental vibrational frequencies (Fourier analysis). This means that if the molecular vibration is anharmonic, the dipole moment will oscillate with the fundamental frequency and integral multiples thereof. These are called the fundamental *overtone*s; the intensity of an overtone absorption is dependent on the amount of anharmonicity in the vibration. Overtone bands can be detected approximately at frequencies $2\nu_i$ where i is one of the fundamental modes of vibration of the molecule. At frequencies of $\nu_i + \nu_j$, where i e j are fundamental modes of vibration, the so called *combination bands* can be found: they are another consequence of the anharmonicity. *Overtone bands*

and *combination bands* are always less strong in intensity than the corresponding fundamental bands.

The parameters which characterize an IR absorption band are:

position : it is indicated with its greatest wavelength (λ_{max}) or (more frequently) with the correspondent wavenumber (ν_{max}); (λ_{max}) depends on the force constant of the chemical bond: the stiffer the chemical bond, the higher the energy necessary to cause the vibration;

intensity : it coincides with the height of the absorption band and corresponds to the probability that the functional group is subjected to the energetic transition from the fundamental state to the excited one. As mentioned above, the intensity of the IR absorption is related to the variation in the dipole moment: for example the carbonyl group which has a strong dipolar moment results in a strong IR absorption. Bands are often classified in *strong*, *medium* and *weak*;

shape : e.g. *sharp* or *broad*.

2.3 Quantitative analysis

According to the theory by Lambert e Beer, a monochromatic radiation of intensity I_0 which hits a body, is partly absorbed by the body and partly transmitted. The ratio between the emitted intensity I and the incident one I_0 defines the *transmittance*

$$T = \frac{I}{I_0} = 10^{-kl} \quad (2.6)$$

where l is the optical path of the radiation through the body and k is the absorption coefficient. There exists a relation between k and the concentration C of the absorption medium:

$$k = \epsilon C \quad (2.7)$$

where ϵ is the so called *molar absorptivity*. More often than the transmittance as in 2.6, the logarithm of the inverse of the transmittance (indicated as absorbance) is used:

$$A = \log \frac{I_0}{I} = \epsilon Cl \quad (2.8)$$

The Beer law is additive: in a mixture the absorbance at a certain wavelength is due to the sum of the absorbance of the different components:

$$A = \sum_i \epsilon_i l C_i \quad (2.9)$$

The Beer law permits to use the spectrophotometry in a quantitative manner. In particular, FTIR spectroscopy was used in this work to measure the concentration of a solvent in a polyimide. The use of FTIR spectroscopy for diffusion studies has many advantages, among which:

- fast and accurate quantitative determination of sorption and desorption kinetics;
- molecular level information (polymer-penetrant interactions, penetrant self-interactions, conformational equilibrium);

- possibility to look at structural modifications of the polymeric substrate as a consequence of penetrant diffusion.

2.3.1 Peaks separations: *curve fitting*

Even with a high spatial resolution IR spectrometer, very often it happens that broad absorption bands overlap with each other; it is, in this case, very difficult to separate and attribute them to the corrispective functional groups. However, as the reader will see in chapter 4 it is very important to distinguish the individual peaks to fully understand the diffusion mechanisms and the nature of the molecular interactions between the polymeric matrix and the solvent molecules; when absorption bands overlap a deconvolution is necessary.

In the case of unresolved, multicomponent bands, a curve resolving algorithm based on the Levenberg-Marquardt method was used to separate the individual peaks (peaks deconvolution was realized through the software GRAMS32) The absorbance $A_i(\nu)$ of the i th peak is given by:

$$A_i(\nu) = \xi A_i^{max} \cdot \frac{\gamma_i^2}{\gamma_i^2 + (\nu_i^0)^2} + (1 + \xi) A_i^{max} \exp \left[\frac{\gamma_i}{(\nu - \nu_i^0)_i} \right]^2 \quad (2.10)$$

where A_i^{max} is the highest absorbance of the i -th peak, $2\gamma_i$ is the full width at half-height (FWHH) of the peak, ν_i^0 is the frequency of the peak and ξ the fraction of lorentzian component. In order to reduce the number of adjustable parameters, the baseline, the band shape, and the number of components were fixed and the curve-fitting analysis yielded the height, the FWHH, and the position of the individual components. The minimum number of components was determined by visual inspection and by a second-derivative analysis of the experimental profile. The peak function used throughout was a Gaussian line-shape.

2.3.2 Two-Dimensional Infrared Correlation Spectroscopy.

Two-dimensional correlation analysis is a perturbation based spectroscopy in which a system, initially at equilibrium, is subjected to the action of an external perturbing force and the response of the IR signals to this perturbation is analyzed. The basic scheme used in 2D IR spectroscopy consists in applying an external perturbation with fixed waveform and analyzing the dynamic response of the system in the form of spectroscopic signals. Typical spectroscopic responses to external stimuli are observed in the form of changes in peak positions, intensities and directional absorbances (dichroic effects). In its original formulation 2D IR analysis was developed for the specific case of a sinusoidally varying perturbation for which a relatively simple analytical solution is available. However, it was soon recognized that the particular excitation waveform does not alter the basic principles of 2D IR analysis, and, more recently, Noda introduced a generalized formalism which can be applied, in principle, to any excitation waveform. Considering a time-dependent spectral intensity $y(\nu, t)$ observed for a period between $-T/2$ and $T/2$, the dynamic spectrum $\tilde{y}(\nu, t)$ is defined as:

$$\tilde{y}(\nu, t) = \begin{cases} y(\nu, t) - \bar{y}(\nu), & \text{for } -T/2 \leq t \leq T/2 \\ 0 & \text{otherwise} \end{cases}$$

$\bar{y}(\nu)$ is the *reference spectrum* and can be selected in a number of ways depending on the specific excitation waveform. In dealing with non-periodic time-dependent behavior, as in the present case, the most effective choice of the reference spectrum is the ground-state spectrum of the system, well before the application of the excitation. Thus, the complex cross-correlation function between dynamic spectral intensities at wavenumbers ν_1 and ν_2 can be expressed as:

$$\Phi(\nu_1, \nu_2) + i\Psi(\nu_1, \nu_2) = \frac{1}{\pi} \int_0^\infty \tilde{\Upsilon}(\nu_1, \omega) \tilde{\Upsilon}^*(\nu_2, \omega) d\omega \quad (2.11)$$

In the above equation 2.11 $\Phi(\nu_1, \nu_2)$ is the synchronous spectrum, $\Psi(\nu_1, \nu_2)$ is the asynchronous spectrum, $\tilde{\Upsilon}_1(\omega)$ represents the forward Fourier transform (FT) of the dynamic spectral intensity $\tilde{y}(\nu_1, t)$, that is

$$\tilde{\Upsilon}(\nu_1, \omega) = \int_{-\infty}^\infty \tilde{y}(\nu_1, t) e^{-i\omega t} dt \quad (2.12)$$

and $\tilde{\Upsilon}^*(\nu_2, t)$ is the conjugate of the FT of the dynamic spectral intensity $\tilde{y}(\nu_2, t)$, i.e.

$$\tilde{\Upsilon}^*(\nu_2, t) = \int_{-\infty}^\infty \tilde{y}(\nu_2, t) e^{i\omega t} dt \quad (2.13)$$

If the response function of the system has a well defined form, it is possible to directly derive the expression for the corresponding 2D correlation spectrum in a closed analytical form. This provides further insight into the significance of the linear and nonlinear correlations between the variables, as revealed by 2-D analysis. The dynamic component of the response function of the investigated system, $\tilde{y}(\nu, t)$ is an exponential decay of the form:

$$\tilde{y}(\nu, t) = \begin{cases} \tilde{y}(\nu, t) = A(\nu) e^{-k(\nu)t}, & \text{for } t \geq 0 \\ 0 & \text{otherwise} \end{cases}$$

where $A(\nu)$ is the initial absorbance value and $k(\nu)$ is the rate constant for the signal at wavenumber ν . Applying equation 2.11 to such a situation, we obtain:

$$\Phi(\nu_1, \nu_2) = \frac{A(\nu_1)A(\nu_2)}{T} \frac{1}{k(\nu_1) + k(\nu_2)} \quad (2.14)$$

$$\Psi(\nu_1, \nu_2) = \frac{A(\nu_1)A(\nu_2)}{\pi T} \frac{\ln k(\nu_2) - \ln k(\nu_1)}{k(\nu_1) + k(\nu_2)} \quad (2.15)$$

and, if the two signals at ν_1 and ν_2 have relatively similar decay constants, equation 2.15 further simplifies to:

$$\Psi(\nu_1, \nu_2) = \frac{2A(\nu_1)A(\nu_2)}{\pi T} \frac{k(\nu_2) - k(\nu_1)}{k(\nu_1) + k(\nu_2)} \quad (2.16)$$

Equations 2.14, 2.15 and 2.16 clarify the meaning of the synchronous and asynchronous spectra in the case of an exponential decay response function. In the synchronous spectrum $[\Phi(\nu_1, \nu_2)]$ a peak will appear at coordinates (ν_1, ν_2) whenever there are two peaks located at ν_1 and ν_2 undergoing intensity changes during the sampling interval, irrespective of their rate constants. The synchronous spectrum is symmetric [i.e., $\Phi(\nu_1, \nu_2) = \Phi(\nu_2, \nu_1)$] and consists of autopeaks located along the main diagonal (i.e., at coordinates ν_i, ν_i) and cross-peaks appearing at off-diagonal positions. The autopeaks identify the signals that undergo changes during the experiment. They are always positive, and their intensity can be considered as a measure of the susceptibility of the relative signals to the external stimulus. The crosspeaks, on the other hand, are positive if the two signals change in the same direction (they both increase or decrease) and are negative otherwise. It appears from the above that, in this specific case, the synchronous spectrum is relatively less interesting than the asynchronous since any changing feature produces a correlation intensity, with no specificity and limited gain in resolution. Conversely, the asynchronous correlation spectrum $[\Psi(\nu_1, \nu_2)]$ identifies decay processes having different rates as a result of the term $\ln k(\nu_2) - \ln k(\nu_1)$ or $k(\nu_2) - k(\nu_1)$, which assumes nonzero values only if the rate constants for the decay processes at the two

wavenumbers are different. This effect is responsible for the resolution enhancement of the asynchronous spectrum. It contains no autopeaks but only cross-peaks at offdiagonal positions and is antisymmetric [i.e., $\psi(\nu_1, \nu_2) = -\psi(\nu_2, \nu_1)$]. The intensity of an asynchronous peak increases as the difference between the decay rates of the relative signals increases. From equation 2.16, it also emerges that an asynchronous cross-peak located at coordinates (ν_1, ν_2) is positive if the intensity change at ν_1 is accelerated with respect to that at ν_2 and is negative otherwise. This is verified whenever $\Phi(\nu_1, \nu_2) > 0$; the opposite occurs if $\Phi(\nu_1, \nu_2) < 0$.

2.3.3 Molecular interactions: spectral consequences

One of the most important aspects in the diffusion of low molecular weight compounds into polymeric system, is the establishment of molecular interactions between the penetrant molecules and the polymeric matrix. When this occurs the perturbed IR spectrum will be different from the unperturbed one. In particular there may be *shift of the absorption frequencies* and *variation of the molar absorptivity* of some species. In these cases the *spectral difference* is very helpful: it is possible, infact, to perform a subtraction between a spectrum of the sample with the above mentioned molecular interactions and a spectrum of the same sample before the interactions were formed. When a variation of the molar absorptivity occurs, the spectral difference will show a residual absorbance in correspondence of the interested frequencies: this difference will be positive or negative depending on whether the new molar absorptivity is higher or smaller. The spectral regions whose frequency shift due to molecular interactions, do not cancel out upon spectral difference. The shape of an absorption band subjected to frequency shift is very similar to the shape of a derivative curve, with the occurrence of a maximum

and a minimum. From a molecular perspective, it is clear that the establishment of molecular interactions result in the modification of the force constants.

Infrared spectroscopy is one of the best means to detect hydrogen bonding, an interaction between an $X - H$ group of a molecule with a Y atom, usually of another molecule, so that a single hydrogen atom is associated with two atoms $X - H \cdots Y$. The atoms usually involved in strong hydrogen bond formation are those with high electronegativities such as F, O, N and Cl . The unbounded $X - H$ stretching band is usually relative sharp when a compound such an alcohol is run in a dilute solution in CCl_4 , for example, or in the vapor state. In more concentrated solutions or in the condensed phase, the hydrogen bond $X - H \cdots Y$ is formed. Then the hydrogen stretching band shifts to lower wavenumbers and becomes much broader and much more intense.

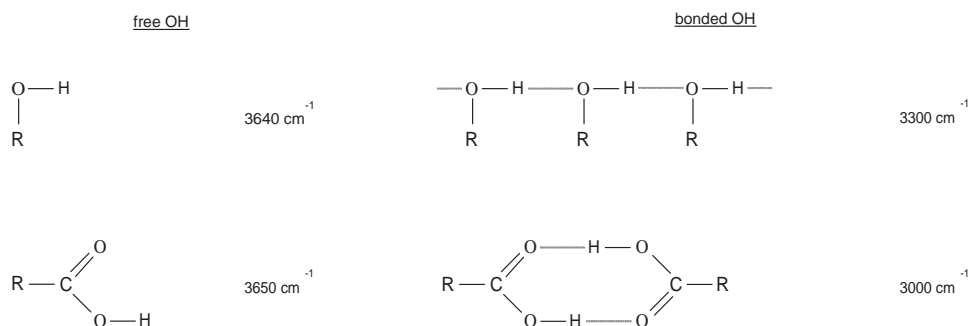


Figure 2.2: OH stretching band shift

The amount of the $X - H$ stretch wavenumber shift on formation of the $X \cdots Y$ hydrogen bond has been correlated with the bandwidth and band intensity for certain cases. Bands involving $X - H$ bending usually increase in wavenumber on the formation of the hydrogen bond, the shift being in the opposite direction from that in stretching vibration, and the magnitude of the shift being much smaller. After the formation of the hydrogen bond, new low frequency bands can be seen

which involve the stretching and bending of the $H \cdots Y$ hydrogen bond. Also, vibrations involving the Y atom may be altered since the force field around Y is altered as a result of the formation of the hydrogen bond. An example is the shift in a $C = O$ (carbonyl) wavenumber in hydrogen bonding solvents.

Chapter 3

Materials and methods

Polyimide films were prepared and tested with a FTIR apparatus and a gravimetric one. Two different PMDA ODA films were prepared: thin films (3.2-1.0 μm) and thick ones (20-30 μm). The molecular probe chosen to study the mechanism of diffusion and interaction with the polymeric matrix was methanol. Methanol 99.8% pure was obtained Lab-Scan Analytical Sciences (Methanol Analytical Reagent); it had a H_2O content less than 0.1%.

3.1 PMDA ODA films preparation

The polyimide precursor used in this study was a polyamic acid, Pyre-ML RK 692, from I.S.T (Indian Orchard, MA). This has molecular weights \overline{M}_w 1.0×10^5 and \overline{M}_n 4.6×10^4 and is supplied as a 12 wt% solution in a mixture of N-methyl-2-pyrrolidone (NMP) and xylene (weight ratio 80/20). The polyamic acid is obtained by condensation of pyromellitic dianhydride (PMDA) and oxidianiline (ODA), whose structures are reported in 3.1.

Polyimide films (30-40 μm) were obtained by spreading the polyamic acid solution onto a glass plate with the aid of a Gardner knife. The cast films were allowed

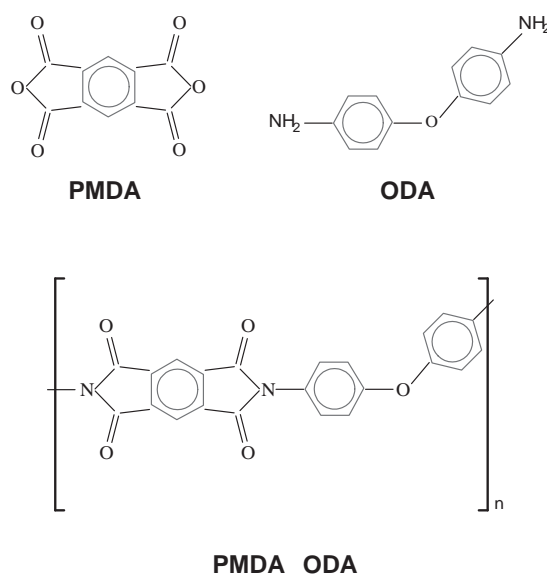


Figure 3.1: PMDA and ODA: reaction of condensation

to dry for 1 h at room temperature and then for 1 h at 80 °C to allow most of the solvent to evaporate. Imidization reactions were carried out in successive isothermal steps of 1 h each at 100, 150, 200, 250, and 300 °C. Finally, the cured films were peeled off from the glass substrate by immersing in distilled water at 80 °C. Thinner films (3.2-1.0 μ m) were obtained by spin-coating a prescribed amount of the polyamic acid solution onto a glass substrate. The spin-coating was a two-step process performed with a Chemat KW-4A apparatus equipped with an automated fluid dispenser (KW-4AD), from Chemat Technologies Inc., Northridge, CA. The spinning conditions were 12 s at 700 rpm for the first step and 20 s at 1500 rpm for the second step. Curing conditions for the spin-coated films were the same as those for the thick films. The spectra collected on different spin-coated films of pure polyimide are reported in Figure 3.2. The evident pattern of interference permits a precise determination of the film thickness, according to the following equation:

$$L = \frac{\Delta n}{2(\nu_2 - \nu_1)\eta} \quad (3.1)$$

where L is the film thickness, Δn is the number of cycles in the wavenumber range between ν_1 and ν_2 , and η is the refractive index of the sample. In the inset of 3.2 is reported the absorbance/concentration ratio as a function of the film thickness for the two main peaks of the imide ring. The calibration curves, in the form of straight lines passing through the origin, confirm that, in the investigated thickness range, the Beer-Lambert relationship is verified and afford the evaluation of film thickness even in the absence of interference fringes.

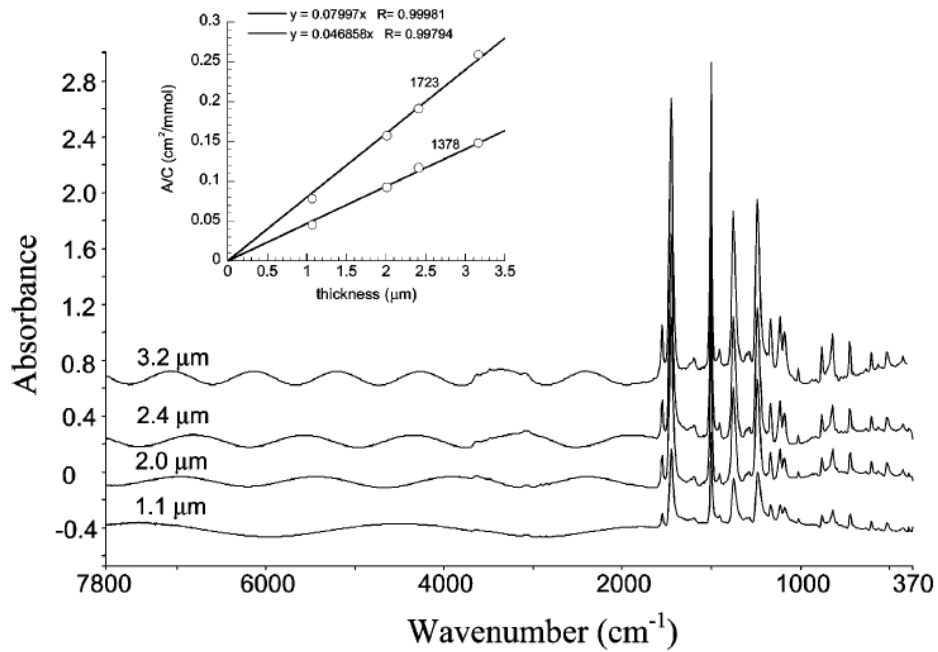


Figure 3.2: FTIR spectrum of spin-coated polyimide films

3.2 Experimental setups and procedures

3.2.1 FTIR apparatus

A vacuum tight FTIR cell designed and developed in our laboratory was used to record the FTIR transmission spectra of the polymer films exposed to methanol vapor at constant pressure. The cell was made of stainless steel and was equipped with a water jacket for temperature control. KBr windows permitted the transmission of the IR beam; the sealing between the windows and the cell itself was warranted by o-rings 3.3. A VCR[®] fitting enabled a leak tight removable closure of the system.



Figure 3.3: Components of the FTIR cell.

The cell was connected through stainless steel 1/8" tube, welded to the VCR cap to the rest of the apparatus which consists mainly of service lines to a liquid methanol reservoir, a vacuum pump, and pressure transducers (a scheme of the apparatus is showed in figure 3.4). Furthermore the apparatus was equipped with a big volume flask used to compensate the changes in the methanol vapor pressure inside the piping due to changes of the external temperature and pressure (figure

3.5). To measure the methanol vapor pressure inside the cell, a pressure transducer MKS Baratron 121 (full scale 100 torr, sensitivity of 0.01*torr* and accuracy of $\pm 0.5\%$ of the reading) was used.

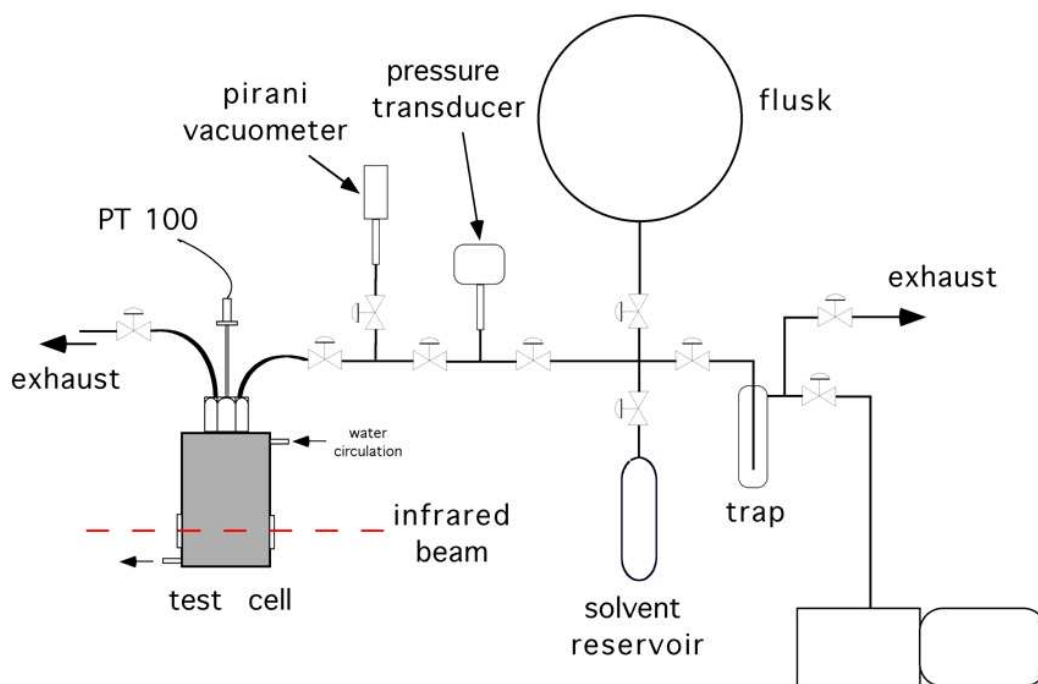


Figure 3.4: Experimental apparatus scheme

The instrument used for the collection of FTIR spectra was a Spectrum-GX from Perkin-Elmer (Norwalk, CT), equipped with a germanium/KBr beam splitter and a wide-band DTGS detector. While the cell was kept at test temperature, the rest of the apparatus remained at room temperature.

Test procedure Before performing a sorption test the methanol was degassed through repetitive freezing and defreezing processes under vacuum and the sample was dried. After the desiccation, connection between the cell and the rest of the apparatus was closed. The solvent reservoir containing degassed methanol was



Figure 3.5: Particular of the experimental apparatus

then opened to let methanol vapor enter the apparatus until the desired level of pressure was reached. In this way the apparatus was pre-loaded at a methanol vapor pressure slightly higher than the desired pressure to take into account the small additive volume of the cell after the opening of the connection. About 120 seconds before the connection to cell was open, the IR computerized acquisition was started (TIME BASE acquisition software package from Perkin ELmer). After a pseudo-equilibrium stage was reached, a desorption test was started. The cell at

the methanol vapor pressure of the sorption stage was isolated through the connection from the rest of the apparatus, which was put under vacuum. When the absolute pressure was lower than 0.001 torr, the connection with cell was opened. The desorption was monitored until an apparent equilibrium was reached.

The instrument used was a Perkin-Elmer interferometer equipped with a Germanium/KBr beam splitter and a wide band DTGS detector. The instrumental parameters for data collection were as follows: resolution 4cm^{-1} , optical path difference (OPD) velocity $0.2\text{cm}/\text{s}$, spectral range $4000 - 400\text{cm}^{-1}$. A single data collection was performed for each spectrum which took 1.5 s to complete under the chosen instrumental conditions. The signals were acquired as single beam spectra at specific time intervals. A typical sorption run lasted about 4 hours, while the acquisition time intervals were 10s during the first 1h of the experiment and 120s thereafter. Automated data acquisition was driven by a dedicated software package for time-resolved spectroscopy (Timebase from Perkin-Elmer). Sorption-desorption tests were performed at 30°C and at relative pressures, p/p_0 , varying from 0.1 to 0.6 (where p is the experimental methanol pressure and p_0 is the saturation pressure of water vapor at 30°C , corresponding to 164.37 torr). The relative pressure was assumed to be equal to the methanol activity, in view of the low value of p_0 .

FTIR Data Analysis. The complete absorbance spectra (i.e., polyimide plus sorbed water) were obtained using the empty cell as background at the test conditions, i.e. at the set methanol vapor pressure. Spectra of sorbed water was obtained by eliminating the spectrum caused by the polymer matrix. This was accomplished by using the ratio method. During an absorption test, the IR beam coming from the source (I) travels across the sample and the methanol vapor

around it. We can define:

$A_p(\nu)$: dry polymer absorbance;

$A_v(\nu)$: methanol vapour absorbance;

$A_c(\nu)$: methanol condensed into the polymer matrix.

Total absorbance $A_{tot}(\nu)$ can be defined as:

$$A_{tot}(\nu) = A_p(\nu) + A_v(\nu)A_c(\nu) \quad (3.2)$$

The contribute of the penetrant inside the cell can be determined choosing I_0 as the intensity of the beam which crosses the cell at the test pressure without the sample:

$$\log \frac{I}{I_0} = A_p + A_c \quad (3.3)$$

As mentioned above, the acquisition of IR spectra starts 120s before the beginning of the absorption test, exactly when the methanol vapour enters the cell. In this way, the dynamic of the diffusive phenomena is followed since its starting instant, correspondent to the cell pressurized at the test pressure and the sample is still dry. If we indicate with I_{dry} the intensity of the IR beam which passes through the cell at the test pressure and through the dry sample, by applying the spectral difference method:

$$A_c = \log \frac{I}{I_0} - \log \frac{I_{dry}}{I_0} \quad (3.4)$$

hence:

$$A_c = \log \frac{I_{dry}}{I} \quad (3.5)$$

Equation 3.4 is valid for unchanged thickness of the sample, i.e when the correlation factor k in the 3.6, introduced to account for changes in sample thickness, is equal

to 1

$$A_c = A_{tot} - kA_p \quad (3.6)$$

The correspondence between equation 3.5 and 3.6 is exact when the change in sample volume due to penetrant absorption is negligible (in this case $k = 1$), as in the present case.

Generalized 2D-IR was performed by a computer program written in house in the Grams/32 environment (Galactic Industries Co., Salem, NH), using the associated programming language Array Basic. A recently developed algorithm was employed, relying on the Hilbert transform,³⁵ which offers an easier and more efficient method for the numerical evaluation of the correlation intensities. The 2-D correlation analysis was performed on an evenly spaced sequence of 20 spectra collected at a constant sampling interval of 12 s. It was found that considering shorter time intervals does not improve the quality and resolution of the resulting correlation spectra.

3.2.2 Gravimetric balance

The equipment used to determine the weight gain of samples exposed to a controlled methanol vapor environment is similar to that used for the on-line FTIR spectroscopy measurements: it is a quartz spring (figure 3.6) placed inside a cylindrical glass vessel equipped with a thermostatic vacuum jacket. The cell is connected to a solvent reservoir and to a pressure transducer. At the end of the spring a small glass punnet was hanged; the polymeric sample was put inside it. The spring elongation was measured with respect to a non deformable reference; that elongation is due to the weight increase of the sample caused by its methanol vapor absorption. The quartz spring used is very sensitive (elastic con-

stant $K = 1.2429 \text{ mg/cm}$ and accuracy 0.01 mm); the polymer mass used was between 0 and 20 mg . The spring elongation was followed thanks to a video monitoring system; a dedicated software in LABVIEW provided data acquisition and storage.

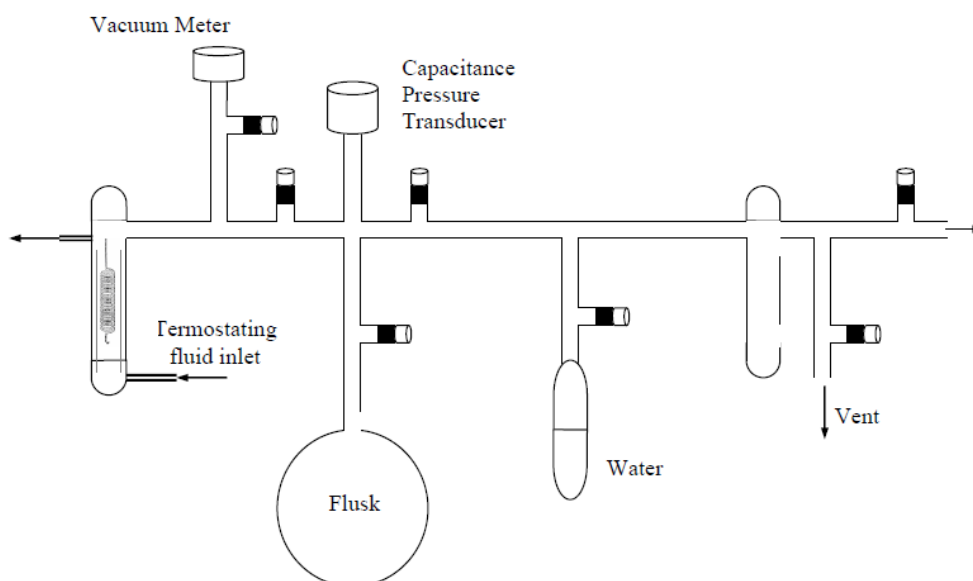


Figure 3.6: Quartz spring apparatus

The experimental procedure was very similar to the one used for the FTIR experiments. Preliminarily, the methanol was degassed with several freezing and defreezing cycles with liquid nitrogen. The experimental procedure was as follow:

- the polymeric sample was dried;
- the cell was isolated from the circuit in which the vacuum was realized;
- the circuit was pressurized at a pressure slightly higher then the one desired;

- the connection between the cell and the circuit was open;
- the spring elongation was followed until a pseudo-stationary steady state was reached.

Chapter 4

Methanol Diffusion in PMDA ODA: results

In this chapter are reported the experimental results of the absorption and desorption tests of methanol in PMDA ODA films. We studied the mechanism of diffusion through “in situ” FTIR analysis and compared the results with gravimetric tests. We used several spectroscopic analysis techniques, among which spectral difference analysis, curve fitting, two dimensional infrared (2D IR) correlation spectroscopy. In particular this last technique permitted us to have further information about the number of penetrant species, their mobility and their interactions with the polymeric matrix.

Sorption and desorption tests were effectuated at $30^{\circ}C$ and at relative pressures p/p_0 of methanol of 0.1, 0.2, 0.3, 0.4, 0.5 and 0.6 (p is the experimental pressure and p_0 is methanol vapor pressure at the temperature of the experiment equal to 163,97 torr). If an ideal behavior of methanol is assumed, the activity of the methanol itself is equal to the relative pressure. For each of the six activities, a sorption and a desorption tests were conducted using a sample cut from the same film of PMDA ODA.

4.1 Analysis of IR spectra

In figure 4.1 are reported the FTIR spectra of a completely dry polyimide film (red trace) and of the same film after equilibration with water vapor at $a_{met} = 0.3$ (blu trace). Sorbed methanol displays characteristic bands in three different regions of the spectrum, i.e., in the $3650 - 3050\text{cm}^{-1}$ range (O-H stretching modes, ν_{OH}), in the $3000 - 2060\text{cm}^{-1}$ range (C-H stretching modes, ν_{CH}) and at around 1000cm^{-1} (correspondent to the C-O stretching modes). The methanol molecules absorbed in the polymer matrix are ideally characterized by two different parts, as showed in the same figure: one insensitive to molecular interactions (CH_3) and the other one sensitive (OH)

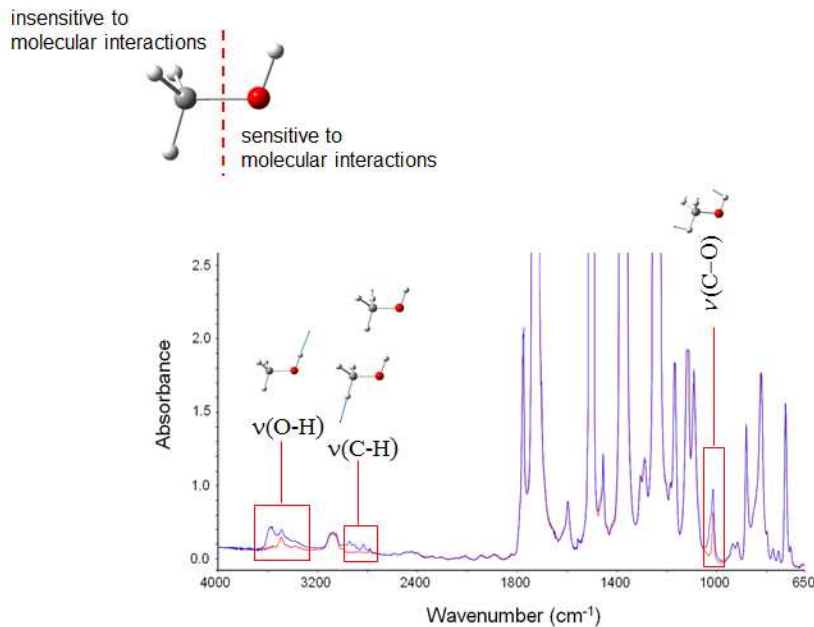


Figure 4.1: FTIR spectra in the $4000, 400\text{cm}^{-1}$ range for the polyimide film in the dry state (red trace) and after equilibration at $a_{met} = 0.5$ (blu trace)

Elimination of the interference from the matrix spectrum, by means of subtraction analysis allows to isolate the spectrum of sorbed methanol in the regions of interest. The difference spectra relative to the stretching modes of $O-H$ and $C-H$ and to the stretching of $C-O$, as collected at different times during a typical sorption experiment ($a_{met} = 0.4$), are reported, respectively, in figure 4.2 and 4.3. The experimental profiles are characterized by the clear presence of two peaks, thus suggesting the concurrent presence of at least two methanol species into the system. A curve fitting analysis of the OH profile has been therefore attempted and is shown in figure 4.4.

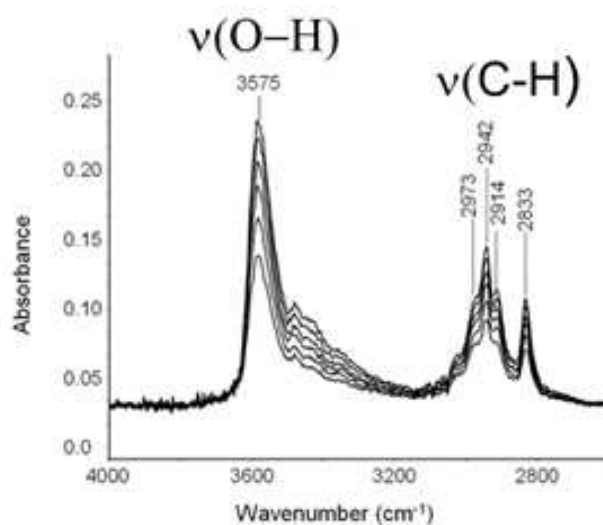


Figure 4.2: FTIR spectra in the $4000, 2700\text{cm}^{-1}$ range at different time intervals

The curve fitting analysis confirmed the presence of at least two peaks (3575cm^{-1} and 3436cm^{-1}) correspondent to two different methanol species, one interacting with the polymer and the other one bonded to other methanol molecules. More on this later: it will be interpreted in detail in a following section, on the basis of

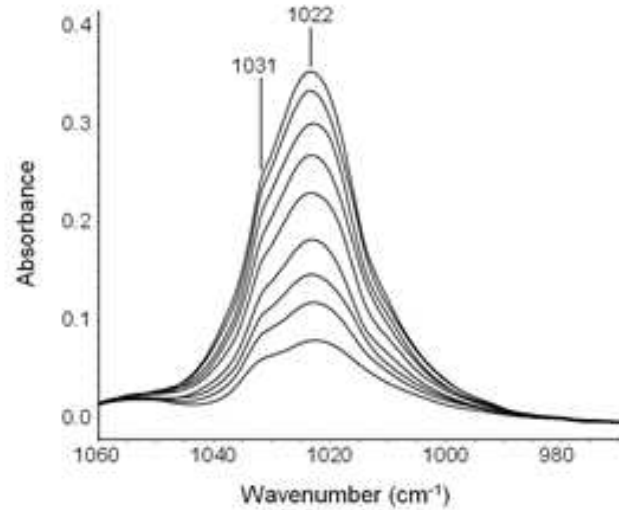


Figure 4.3: FTIR spectra in the $1060,960\text{cm}^{-1}$ range at different time intervals

the additional information gathered from 2D-FTIR spectroscopy.

A typical example of a sorption-desorption cycle, as followed by measuring the absorbance areas in the *OH* region and in the *CO* region, is shown in figures 4.5 and 4.6. In figure 4.7, the same data are plotted in a Fick's diagram, i.e., as the ratio of absorbance at time t over absorbance at equilibrium versus the square root of time. Spectroscopic data as those displayed in figures 4.5 and 4.6 and afford the precise monitoring of the diffusion kinetics. Furthermore, figure evidences the Fickian behavior of the system and indicates that desorption is much slower than sorption. This result is confirmed at all investigated activities and points to a concentration dependence of the diffusivity, D (i.e., D increases by enhancing the penetrant concentration).

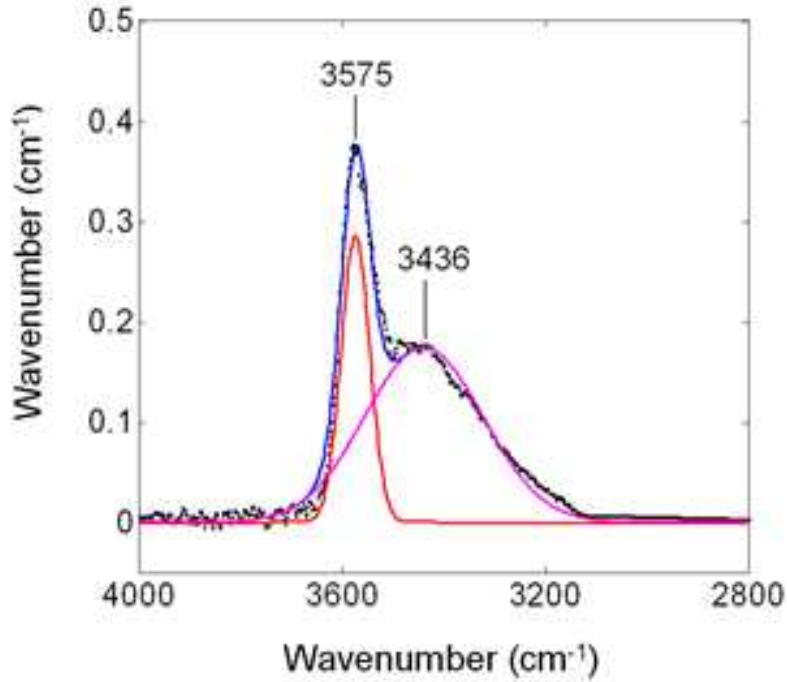


Figure 4.4: Curve fitting of the O-H stretching frequency range

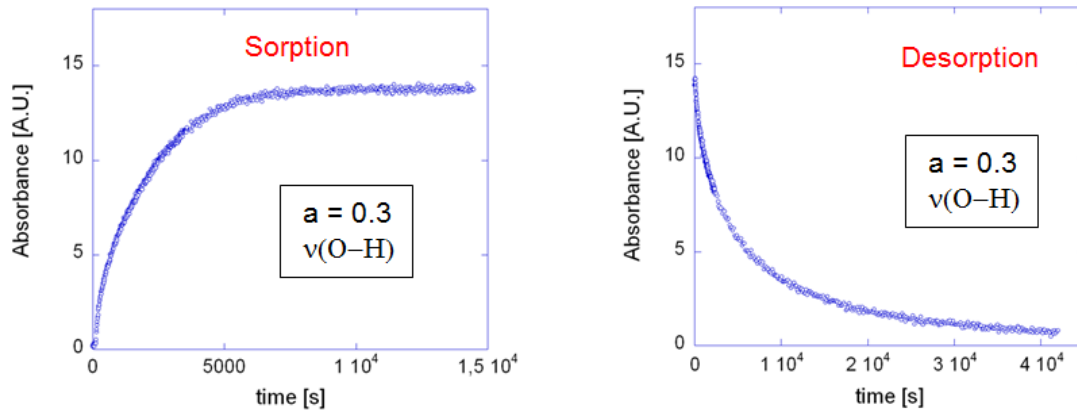


Figure 4.5: Absorbance of the ν_{OH} band: absorption and desorption kinetics

The appropriate solution of the diffusion equation may be written as follow:

$$\frac{M}{M_{\infty}} = 1 - \sum_{n=0}^{+\infty} \frac{8}{(2n+1)^2\pi^2} \exp \left\{ -(2n+1)^2\pi^2 \frac{Dt}{4L^2} \right\} \quad (4.1)$$

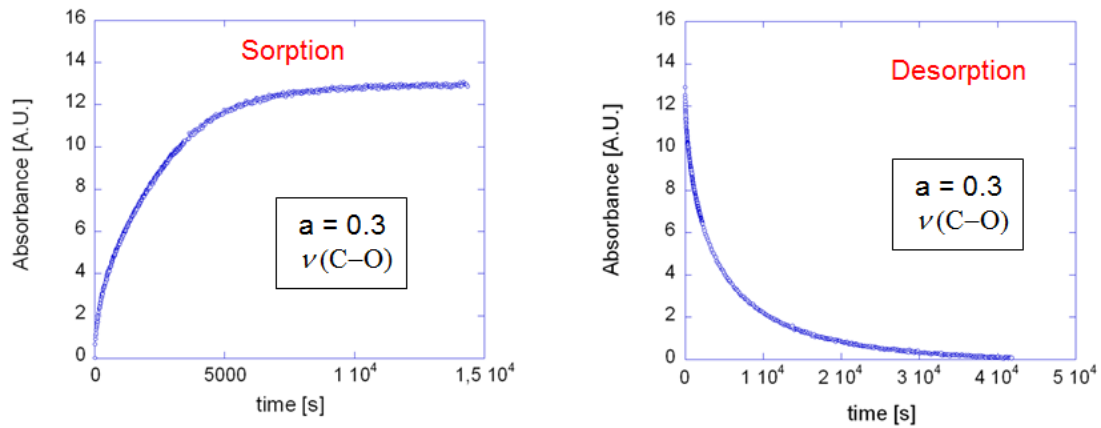


Figure 4.6: Absorbance of the ν_{CO} band: absorption and desorption kinetics

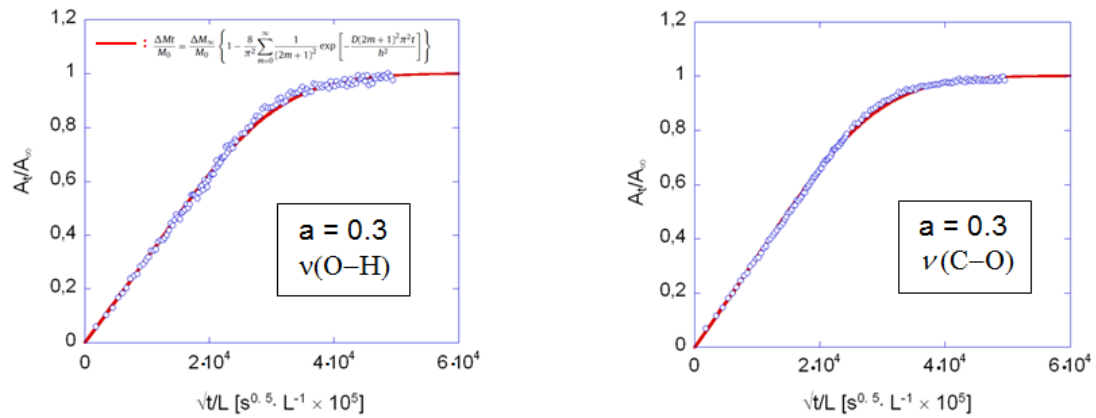


Figure 4.7: Fick's diagrams of ν_{OH} and ν_{CO} absorption bands

if the uptake is considered to be a diffusion process controlled by a constant diffusion coefficient D . Here $M(t)$ and M_∞ represent, respectively, the penetrant mass sorbed at time t and at equilibrium. The application of 4.1 is based on the assumption that immediately the polymer film is placed in the vapor the concentration at each surface attains a value corresponding to the equilibrium uptake for the vapor pressure existing, and remains constant afterwards. The film is considered to be initially free of vapor. The value of t/l^2 for which $M_t/M_\infty = 1/2$, indicated as $(t/l^2)_{1/2}$, is given by:

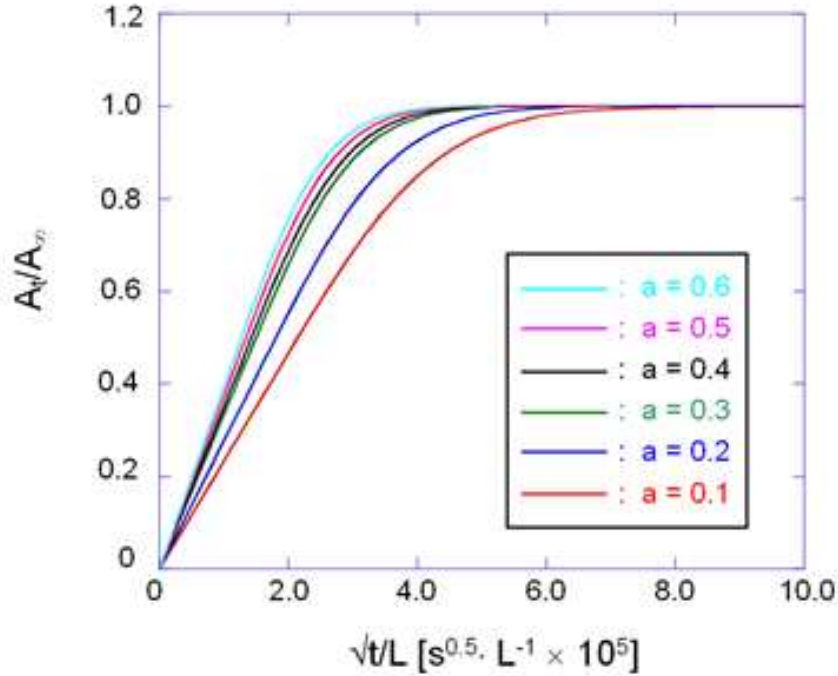


Figure 4.8: Fick's diagrams of ν_{OH} absorption band for all the activities

$$\left(\frac{t}{l^2}\right)_{1/2} = -\frac{1}{\pi^2 D} \ln \left\{ \frac{\pi^2}{16} - \frac{1}{9} \left(\frac{\pi^2}{16}\right)^9 \right\} \quad (4.2)$$

approximately, the error being about 0.001%. Thus we have

$$D = \frac{0.049}{(t/l^2)} \quad (4.3)$$

and so, if the half-time of a sorption process is observed experimentally for a system in which the diffusion coefficient is constant, the value of this constant can be determined from 4.3. However, as we have pointed out above, in our case the diffusion coefficient is not constant, being a function of methanol concentration. The calculation of D to the less simple case in which it is a function of the concentration was carried out by Crank and Park [8]. The 4.3 represents an average diffusivity,

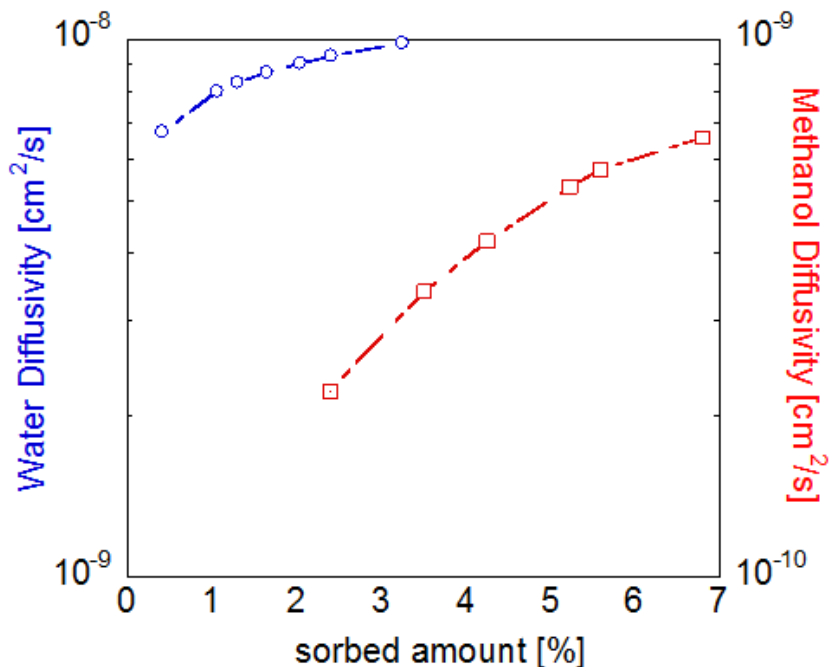


Figure 4.9: Calculated methanol diffusivity compared to water diffusivity in PMDA ODA

\bar{D} , let us say of the variable diffusion coefficient averaged over the range of concentration appropriate to each sorption test. The method devised by Crank and Park (1949) depends on the fact that, for any experiment of sorption, \bar{D} provides a reasonable approximation to

$$\frac{1}{C_0} \int_0^{C_0} D dC \quad (4.4)$$

where 0 to C_0 is the concentration range existing in the polymeric film during the sorption test. This was shown to be so by evaluating numerical solutions of the diffusion equation for a number of variable diffusion coefficients. Thus by deducing a value of \bar{D} from each of the experimental curves of sorption using the 4.3, and

assuming the approximate relationship

$$\bar{D} = \frac{1}{C_0} \int_0^{C_0} D dC \quad (4.5)$$

a graph showing $\bar{D}C_0$ as a function of C_0 can be drawn and numerical or graphical differentiation of the curve with respect to C_0 gives a first approximation to the relationship between D and C . This is reported in figure 4.9, where we reported also the diffusivity for water in PMDA ODA for comparison.

4.2 Gravimetric tests

Gravimetric test were conducted at the same activities of methanol of IR tests; samples cut from the same PMDA ODA film were used. In figure 4.10, a typical gravimetric sorption test is shown. Gravimetric data (i.e mass of methanol absorbed) were corrected taking into account the Archimedes' buoyancy principle. In figure 4.11 we report the Fick's diagram of gravimetric sorption test at different methanol activities.

4.2.1 Comparison with IR

The qualitative analysis of the figures 4.8 and 4.11 allows us to cross-check the reliability of the quantitative analysis and to confirm a linear relationship between absorbance and concentration for both signals. This linear relationship is further demonstrated in figure 4.12, where the intensities of the IR absorption bands (OH , CO and CH), normalized for film thickness, are reported as a function of the concentration of methanol in the sample as evaluated gravimetrically. The straight line passing through the origin confirms that the system obeys the Lambert-Beer relationship, allowing direct conversion between spectroscopic and

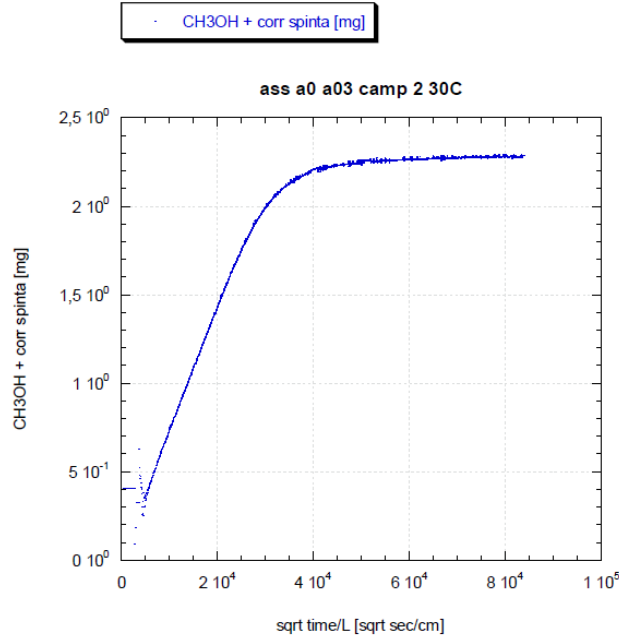


Figure 4.10: Gravimetric sorption curve at $a_{met} = 0.3$

gravimetric data.

Furthermore, IR and gravimetric isotherms (plotted, respectively in figure 4.13 and 4.14) have the same shape, confirming again the reliability of the IR analysis of the diffusive phenomenon.

4.3 Two Dimensional Correlation Spectroscopy

In order to deepen our interpretation of the spectroscopic data, it is advisable to rely on a technique which could improve the resolution and, at the same time, provide information about the dynamics of the evolving system. As discussed above, 2D FTIR is one of these techniques. The analysis produces two distinct

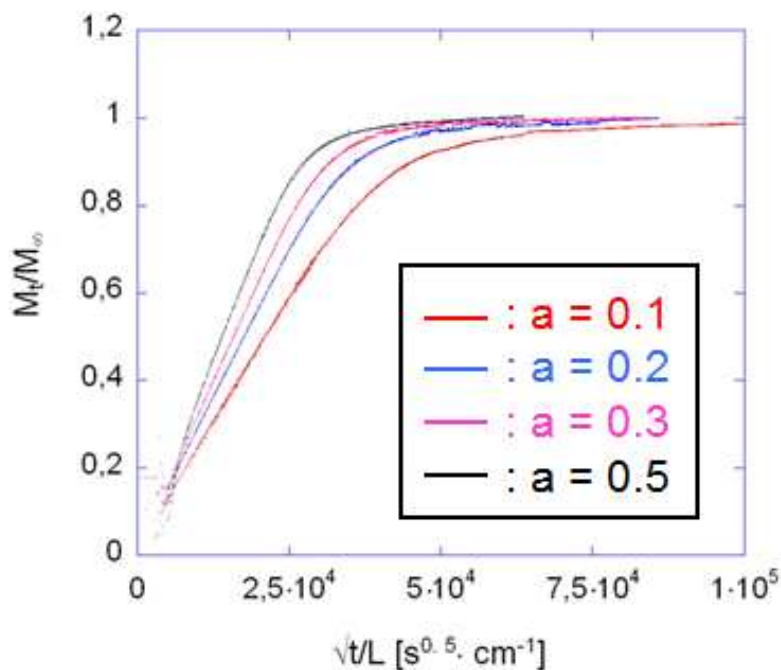


Figure 4.11: Fick's diagrams of gravimetric sorption tests

spectra: the synchronous spectrum and the asynchronous spectrum. The former highlights the peaks that are more sensitive to the perturbation (autopeaks) and the IR signals that change with the same rate. A peak in the asynchronous spectrum corresponds to two IR signals that change at different rates. Conversely, if two signals change at the same rate they will produce zero intensity in the asynchronous spectrum.

Synchronous and asynchronous spectra for the frequency range $3800 - 2600\text{cm}^{-1}$ referred to the absorption and desorption cycle at $a_{met} = 0.6$ are showed in figures 4.15 and 4.16. Peaks that appear in these spectra are summarized in tables 4.1 and 4.2. The tables indicate also the type of the peaks (AutoPeaks and Cross-Peaks) and the sign. The spectra show that there are at least three peaks changing

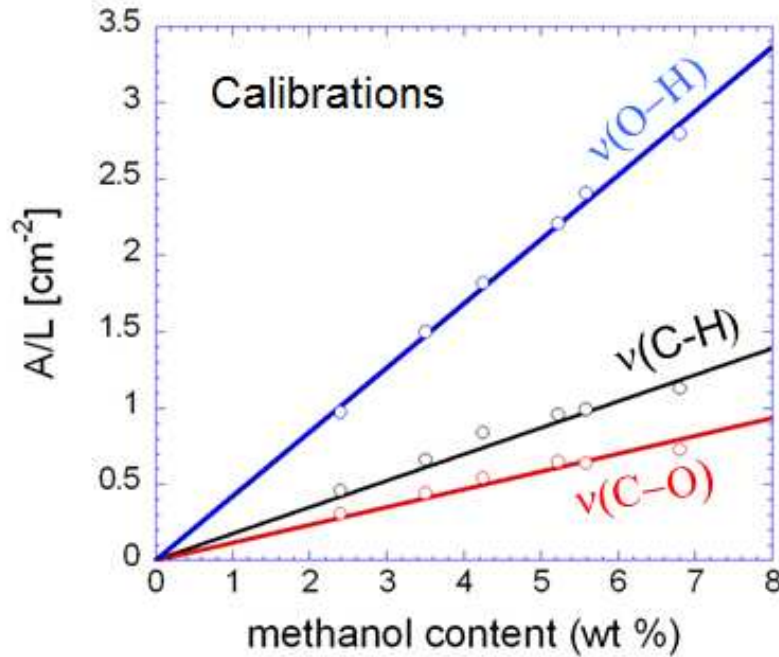


Figure 4.12: Calibration curve of IR data

in intensity located at 3576 , 2944 and 2832cm^{-1} , the peak located at 3576cm^{-1} being the one which is subject to the biggest change. The peaks appearing in the synchronous spectrum are all positive: that means that all IR signals change in the same direction, all increasing or decreasing in intensity. The asynchronous spectrum clearly show that the points of coordinates $(3576, 2944)$ and $(3576, 2832)$ are both positive, meaning that the change in intensity of the peak 3576cm^{-1} is greater than the other two. The situation is the opposite during the desorption test, the peak at 3576cm^{-1} being the one that decreases with the smallest velocity. The 2D FTIR analysis confirmed the presence of at least two methanol species: one fastest then the other during a sorption test and slower during a desorption test. The same result can be obtained if the absorbance areas of the two compo-

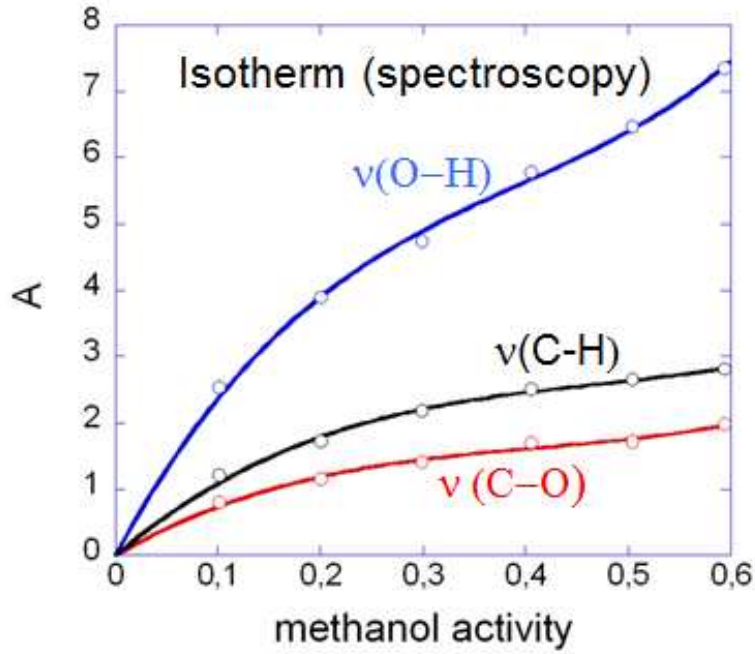


Figure 4.13: Spectroscopic isotherm of absorption

nents peaks of the fitting curve in the area of ν_{OH} are plotted (figure 4.4) as it is shown in figures 4.19 and 4.20.

ν_1	ν_2	Sign	Type
3576	3576	+	AP
2944	2944	+	AP
3456	3576	+	CP
2944	3576	+	CP
2912	3576	+	CP
2832	3576	+	CP
2832	3576	+	CP

Table 4.1: Peaks in the synchronous spectrum in the range $3800 - 2600\text{cm}^{-1}$

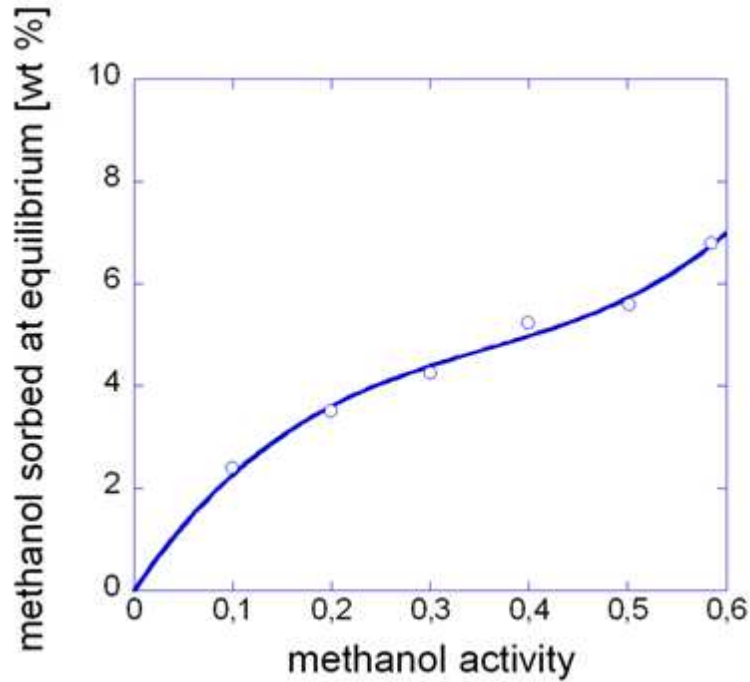


Figure 4.14: Gravimetric isotherm of absorption

ν_1	ν_2	Sign	Type
3426	3580	-	CP
2944	3580	-	CP
2823	3580	-	CP
2944	3426	+	CP
2823	3426	+	CP

Table 4.2: Peaks in the asynchronous spectrum in the range $3800 - 2600\text{cm}^{-1}$

4.4 IR spectra of methanol in CCl_4

In fig 4.21 are shown the IR spectra of methanol in CCl_4 at three different methanol concentration, i.e. $0.012M$, $0.05M$ e $0.1M$. At the two lowest concentrations a well defined methanol absorption band, correspondent to the OH stretching ν_{OH}

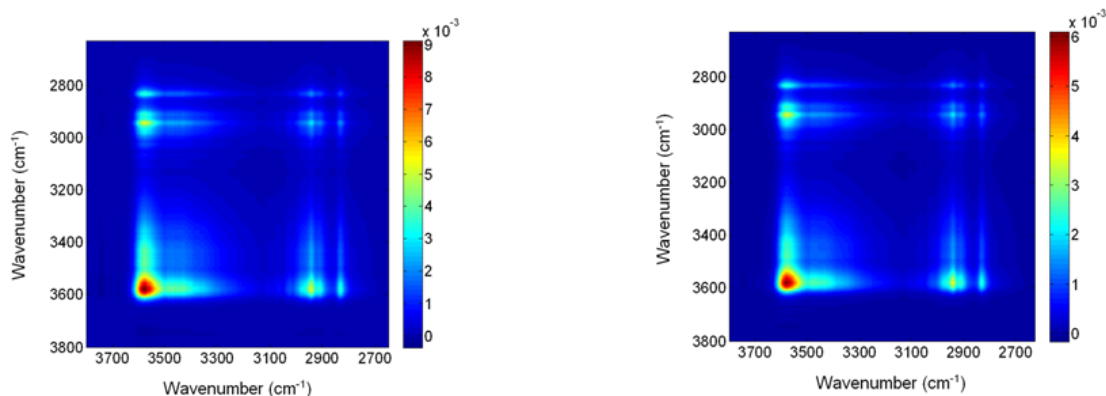


Figure 4.15: 2DFTIR synchronous spectrum for absorption and desorption test at $a_{met} = 0.6$ in the range $3800 - 2600\text{cm}^{-1}$

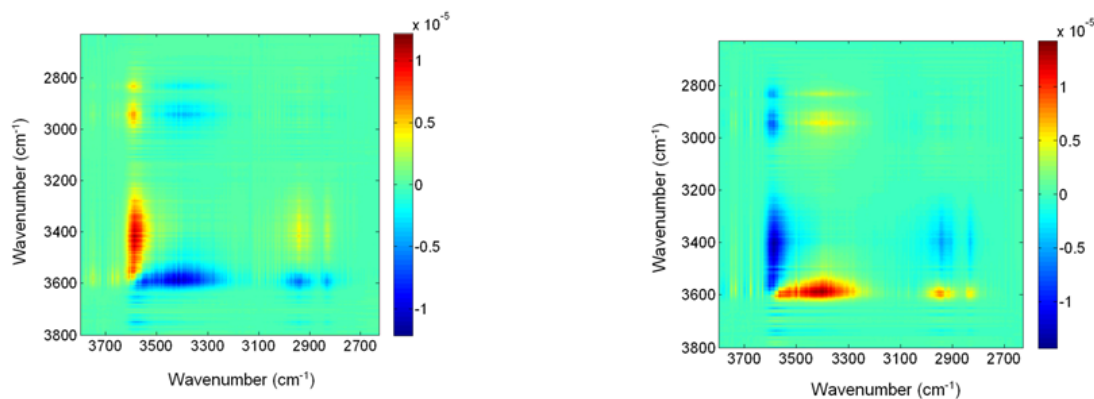


Figure 4.16: 2DFTIR asynchronous spectrum for absorption and desorption test at $a_{met} = 0.6$ in the range $3800 - 2600\text{cm}^{-1}$

is present; that band is attributable to OH group not bonded in hydrogen bonds, hence to monomeric form of methanol and to “open” polymeric forms. At higher concentrations, at lower wavenumbers a broad absorption band is present; different methanol polymeric forms contribute to the total absorbance of this band. As it is possible to see in figure 4.21, a curve fitting of the ν_{OH} band at the highest concentration ($0.1M$) results in four components centered at 3674cm^{-1} , 3643cm^{-1} , 3510cm^{-1} e 3348cm^{-1} . Reasonably these bands can be assigned as follows:

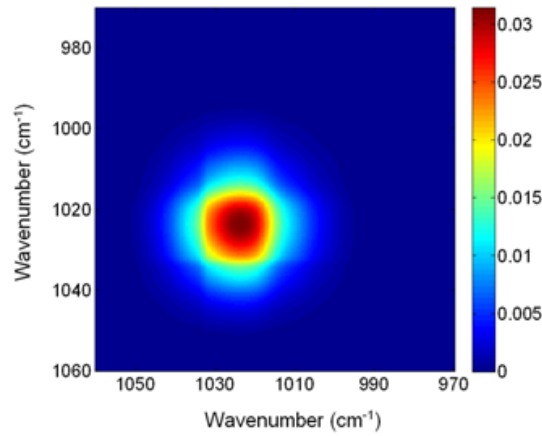


Figure 4.17: 2DFTIR synchronous spectrum for absorption and desorption test at $a_{met} = 0.6$ in the range $1060 - 960\text{cm}^{-1}$

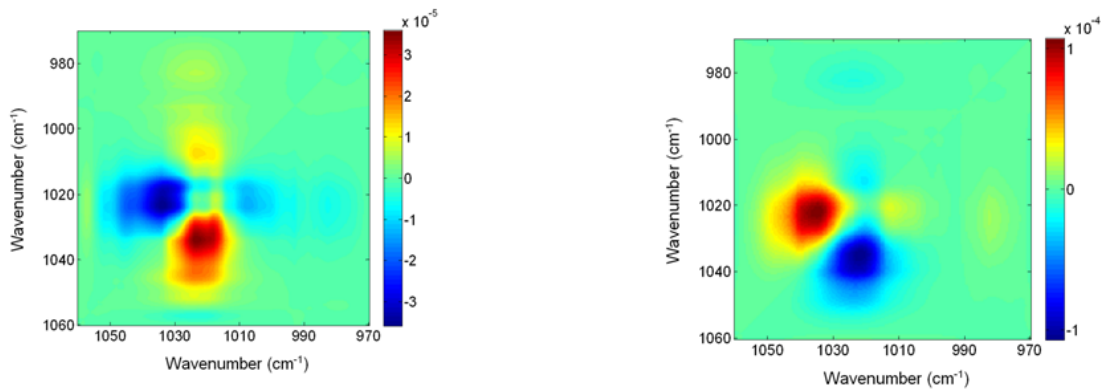


Figure 4.18: 2DFTIR asynchronous spectrum for absorption and desorption test at $a_{met} = 0.6$ in the range $1060 - 960\text{cm}^{-1}$

- the first to the $O - H$ of an open dimer not bounded with hydrogen bonds;
- the second to the $O - H$ of a monomer;
- the third to the $O - H$ of a cyclic dimer bounded with hydrogen bonds;
- the fourth to the $O - H$ of cyclic polymeric forms (above all trimers and tetramers)

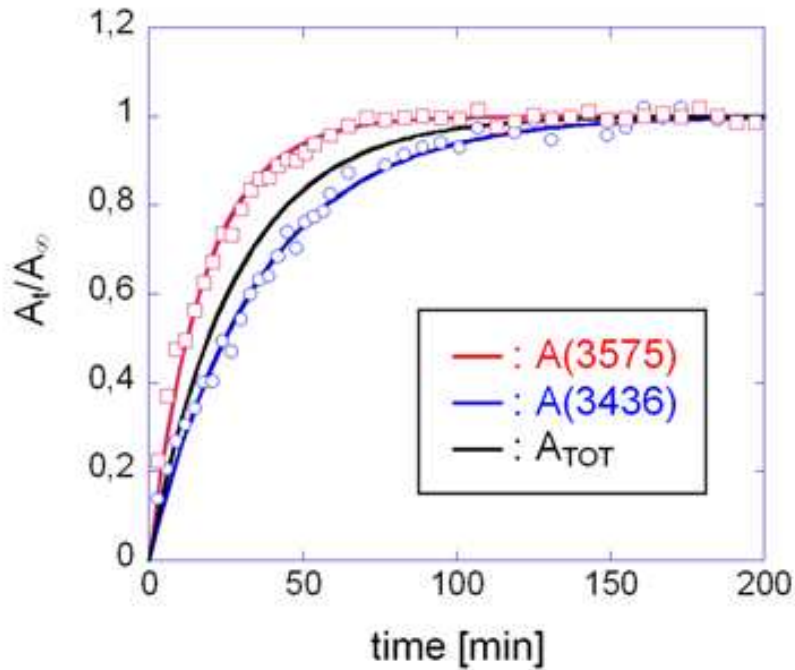


Figure 4.19: Sorption dynamic of the components of the ν_{OH} absorption band

In figure 4.22 the IR spectrum of methanol condensed in PMDA ODA is shown. Regarding the peaks in that figure, it is reasonable to assume that the peak at 3571cm^{-1} is attributable to the OH stretching of a methanol molecule bonded to the $C=O$ group of the polyimide and that the peak at 3420 is due to the OH stretching of self-associated methanol molecules.

4.5 Conclusions

The transport of methanol into polyimide films has been investigated by means of time-resolved FTIR spectroscopy with the aim of elucidating the molecular mechanism of diffusion. Several approaches have been employed to analyze the

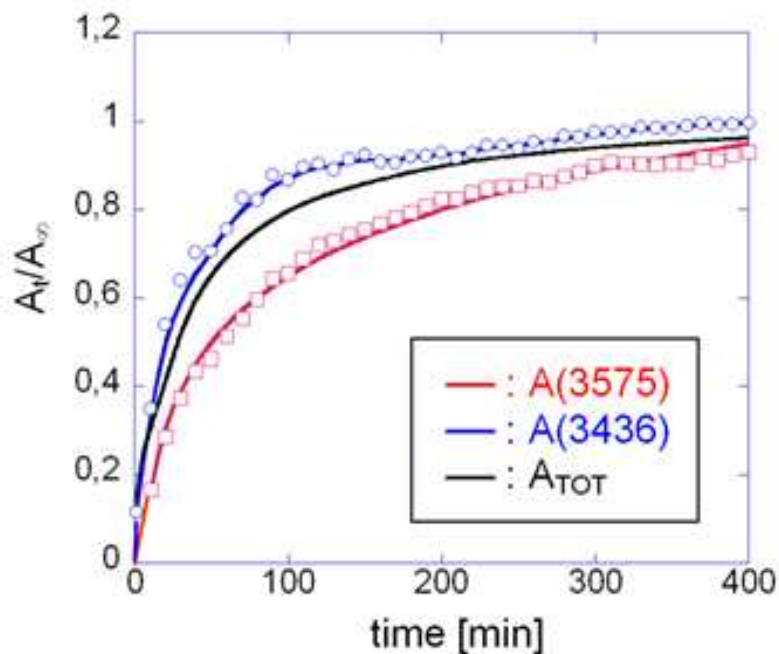


Figure 4.20: Desorption dynamic of the components of the ν_{OH} absorption band

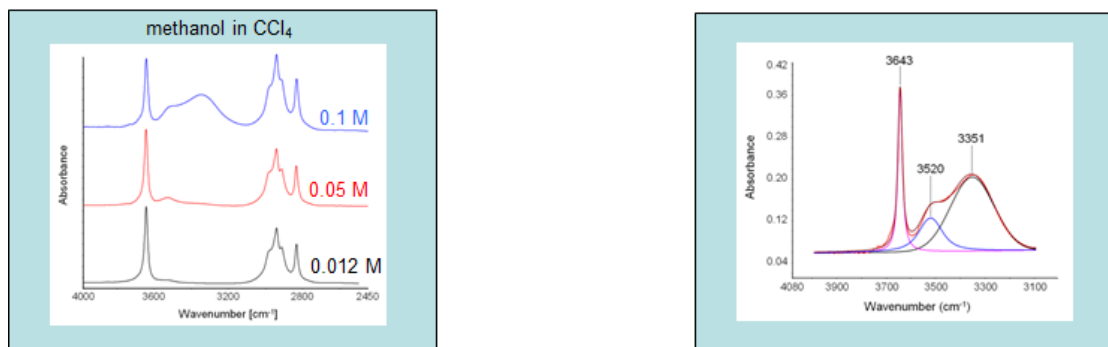


Figure 4.21: IR spectra and fitting of methanol in CCl_4

spectral data, namely, difference spectroscopy, least-squares curve fitting and 2D correlation spectroscopy. The main findings may be summarized as follows:

- two distinct methanol species have been identified in the system, correspond-

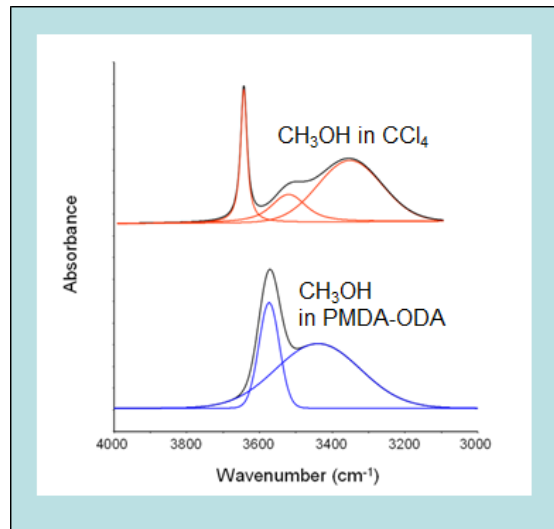
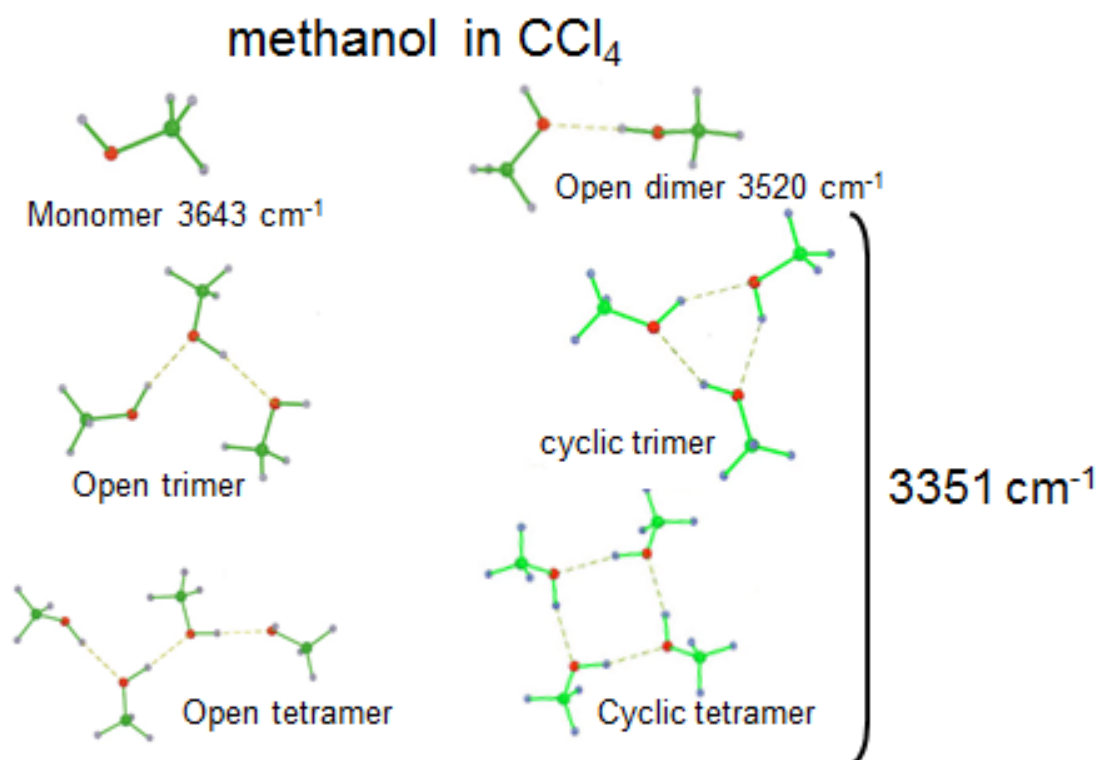
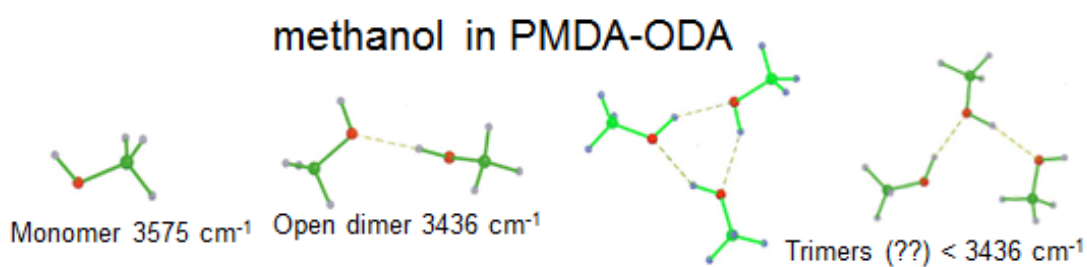


Figure 4.22: Comparison between methanol in CCl_4 and in PMDA ODA

ing to CH_3OH molecules interacting with the polymer matrix and to self-associated methanol, predominantly dimers and trimers;

- the two species display different and peculiar dynamic behaviors, i.e., on sorption, the methanol molecules bound to PMDA ODA enter the system at a faster rate than the self-interacting molecules, while the opposite occurs on desorption.

Figure 4.23: Methanol aggregate forms in CCl_4 Figure 4.24: Methanol aggregate forms in $PMDAODA$

Chapter 5

Pervaporation And Vapor Permeation

5.1 Fundamentals

Pervaporation (PV) and vapor permeation (VP) have attracted much interest because of their ability to separate aqueous organic mixtures with reduced energy consumption [27]. In both processes the permeate side is a vapor while the feed side is a liquid in the pervaporation case and a vapour in the vapor permeation case. Mass transport through the membrane is induced by the vapor pressure difference in the former case and by the partial pressure difference in the latter. In both cases the pressure difference can be maintained in several ways [11]. In the laboratory, a vacuum pump is usually used to draw a vacuum on the permeate side of the system. Industrially the permeate vacuum is most economically generated by cooling the permeate vapor, causing it to condense; condensation spontaneously creates a partial vacuum [5].

Transport in pervaporation membranes occurs by the solution-diffusion mechanism [36]. Classic transport models [38] describe pervaporation as a three steps-process:

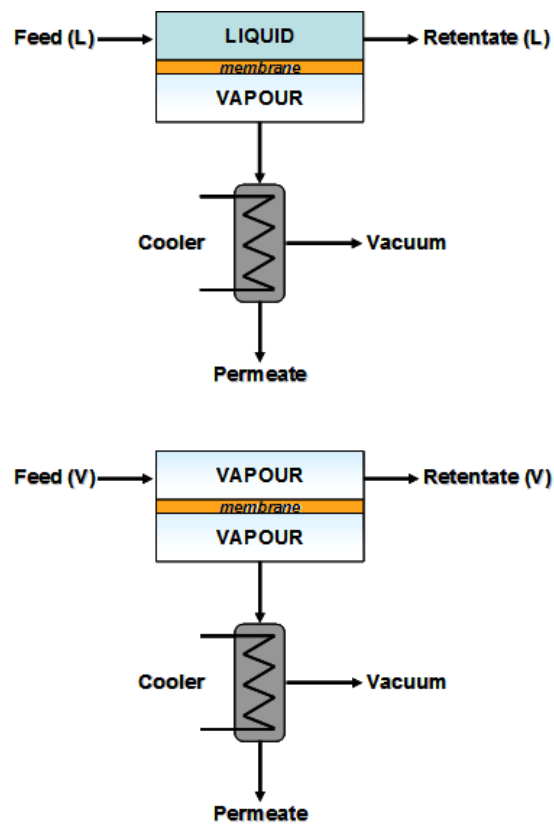


Figure 5.1: Pervaporation and vapor permeation processes

- sorption equilibrium between the liquid feed side and the membrane;
- diffusion through the membrane driven by a chemical potential gradient;
- desorption into the vapor permeate side.

Unlike reverse osmosis, pervaporation transport is not limited by osmotic pressure because the driving force for mass transfer through the membrane is provided by lowering the chemical potential of the permeate stream on the downstream side, and consequently, the feed pressure is not critical. As in reverse osmosis, the liquid in contact with the membrane causes membrane swelling. Swelling tends to alter the membrane properties and generally leads to higher permeability and lower

selectivity. Unlike reverse osmosis and membrane gas separation, pervaporation involves a phase change of permeating species from the liquid to the vapor state. Consequently, energy is needed for the vaporization of the permeate. Thus, from an energy consumption point of view, pervaporation is especially promising when the concentration of the preferentially permeating species in the feed is low. A common issue in pervaporation operations is the so called *Concentration Polarization Effect*: due to retention of the slow permeating component on the membrane surface, the concentration of the fast permeating component the membrane surface is lower than that in the bulk phase, while the opposite is true for the slow component [20]. This is shown schematically in figure 5.2 Concentration polarization generally leads to a lower productivity and a lesser extent of separation However compactness, flexibility, simplicity, and versatility are some strong properties of the pervaporation process.

Vapor permeation is very similar in principle to pervaporataion; as we have said the only important difference is the physical nature of the feed side. Vapor permeation has attracted increasing attention because of the following characteristics in comparison with pervaporation [15]:

- heat equivalent to the enthalpy of vaporization not required (there is no change of phase involved and so no temperature drop across the membrane);
- membranes have longer service life because of low swelling;
- higher fluxes can be achieved due to higher temperatures involved in the process;
- operation in the vapor phase eliminates the effect of the concentration polarization, prevalent in liquid phase separations;

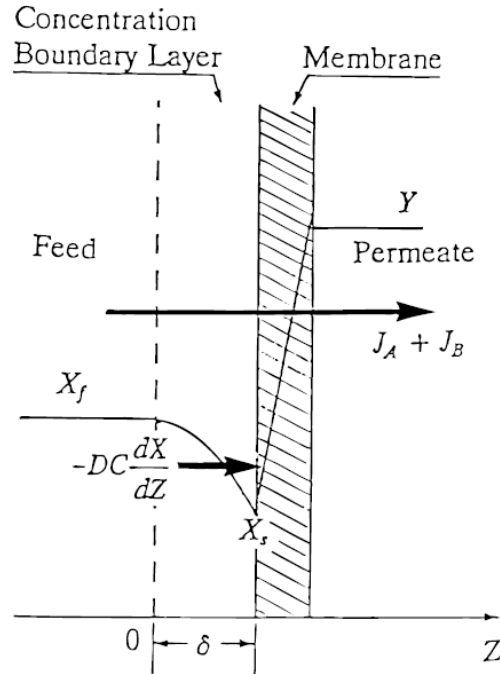


Figure 5.2: Concentration polarization effect

- a hybrid process with distillation can be effectively realized.

5.2 Flux Equations for PV and VP processes

A binary mixture of components i (preferentially permeating species) and j is discussed in this work. VP through a nonporous polymeric membrane is interpreted according to the solution-diffusion model. For component i , the permeation flux, q_i , is given by following equation 8.1

$$q_i = P_i \frac{(p_{i1} - p_{i2})}{l} \quad (5.1)$$

where P_i is the permeability coefficient, p_i the partial pressure of component

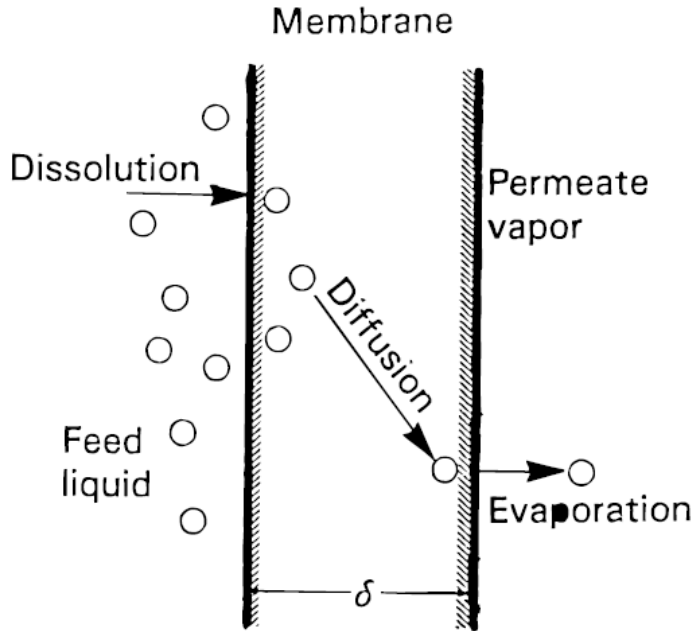


Figure 5.3: Solution-diffusion theory

i , l the thickness of the membrane, and subscripts 1 and 2 denote the feed and permeate sides of the membrane respectively. The separation factor for VP, α_{VP} is given by equation 5.2

$$\alpha = \frac{p_{i2}/p_{j2}}{p_{i1}/p_{j1}} \quad (5.2)$$

PV may be also interpreted according to the solution-diffusion model. Each membrane surface is in equilibrium with the fluid on that side of the membrane. The concentrations of the components i and j in the membrane at each interface will be proportional to the chemical potentials of the components in the adjacent fluids. On the feed side of the membrane, the chemical potentials for a feed solution of mole concentrations c_i and c_j can be expressed as the partial pressures p_{i1} , and

p_j , of the vapor in equilibrium with the feed solution. Then, we can express the permeation flux for PV by equation 8.1. The partial pressures of the components of the vapor in equilibrium with the feed solution are given by equation 5.3 . For component i ,

$$p_{i1} = \gamma_i x_{Mi} p_i^0 \quad (5.3)$$

where γ_i is the activity coefficient, x_{Mi} , the mole fraction in the feed solution, p_i^0 the saturated vapor pressure at temperature T . The γ and p^0 for water-ethanol mixtures are calculated by Margules's equation and Antoine's equation, respectively

$$\begin{aligned} \ln \gamma_W &= (1.0574 + 0.7209x_{MW})x_{ME}^2 \\ \ln \gamma_E &= (1.4177 - 0.7209x_{ME})x_{MW}^2 \end{aligned} \quad (5.4)$$

$$\begin{aligned} \log p_W^0 &= 8.07131 - \frac{1730.670}{T + 233.426} \\ \log p_E^0 &= 8.1120 - \frac{1592.864}{T + 226.184} \end{aligned} \quad (5.5)$$

where p^0 and T are in the units of mmHg and °C, respectively, and subscripts W and E denote water and ethanol components, respectively.

Beside Antoine's equation, many equations have been proposed for the relation between activity coefficients and mole fractions and new ones keeps on be formulated. Among these, the NRTL (Non Random Two Liquids) is one of the most used. The NRTL equation for the excess Gibbs energy is

$$\frac{g^E}{RT} = x_1 x_2 \left(\frac{\tau_{21} G_{21}}{x_1 + x_2 G_{21}} + \frac{\tau_{12} G_{12}}{x_2 + x_1 G_{12}} \right) \quad (5.6)$$

where

$$\begin{aligned}\tau_{12} &= \frac{g_{12} - g_{22}}{RT} \\ \tau_{21} &= \frac{g_{21} - g_{11}}{RT} \\ G_{12} &= \exp(-\beta_{12}\tau_{12}) \\ G_{21} &= \exp(-\beta_{12}\tau_{21})\end{aligned}\quad (5.7)$$

Parameter β_{12} is related to the nonrandomness in the mixture; when β_{12} is zero, the mixture is completely random and equation 5.6 reduces to the Margules equation. The NRTL equation contains three parameters, but reduction of experimental data for a large number of binary system indicates that β_{12} varies from about 0.20 to 0.47. The activity coefficients are:

$$\ln \gamma_1 = x_2^2 \left[\tau_{21} \left(\frac{G_{21}}{x_1 + x_2 G_{21}} \right)^2 + \frac{\tau_{12} G_{12}}{(x_2 + x_1 G_{12})^2} \right] \quad (5.8)$$

$$\ln \gamma_2 = x_1^2 \left[\tau_{12} \left(\frac{G_{12}}{x_2 + x_1 G_{12}} \right)^2 + \frac{\tau_{21} G_{21}}{(x_1 + x_2 G_{21})^2} \right] \quad (5.9)$$

Separation factor for PV, α_{PV} , is given by following equation:

$$\alpha_{PV} = \frac{(p_{i2}/p_{j2})}{c_i/c_j} \quad (5.10)$$

To understand the difference between PV and VP, it is convenient to consider the overall separation factor as the product of the separation factor at the evaporation

separation step, α_{evap} and that at the membrane separation step

$$\alpha_{mem}, \quad (5.11)$$

$$\alpha_{PV} = \alpha_{evap}\alpha_{mem} \quad (5.12)$$

$$\alpha_{evap} = \frac{(p_{i1}/p_{j1})}{c_i/c_j} \quad (5.13)$$

$$\alpha_{mem} = \frac{(p_{i2}/p_{j2})}{p_{i1}/p_{j1}} \quad (5.14)$$

When the total pressure on the permeate side p_2 is sufficiently low, as in this study, the above equations reduce to:

$$\alpha_{VP} = P_i/P_j \text{ for low } p_2 \quad (5.15)$$

$$\alpha_{mem} = P_i/P_j \text{ for low } p_2 \quad (5.16)$$

Using both P_i and α_{mem} rather than q_i and α_{PV} , membrane performance for PV may be compared with that for VP (P_i and α_{PV}).

5.3 Membranes and Membrane Modules for PV and VP

Pervaporation and vapor permeation are rate-controlled separation processes. In developing PV and VP membranes, three issues must be addressed:

1. membrane *productivity*
2. membrane *selectivity*
3. membrane *stability*

Membrane *productivity* is a measure of the quantity of the component which permeates through the membrane per unit of area and unit of time. It is frequently characterized by permeation flux J which depends on both the intrinsic permeability and the effective thickness of a membrane. Generally speaking, the *selectivity* is the capability of a membrane of permeating preferentially one of the feed mixture components, at higher rate with respect to the others. The *separation factor* is defined as

$$\alpha = \left(\frac{Y}{1-Y} \right) \left(\frac{1-X}{X} \right) \quad (5.17)$$

where X and Y are the molar fractions of the more permeable component in the feed and permeate, respectively. When the separation factor is equal to 1 no separation occurs; when it approaches infinity, the membrane becomes 'perfect', letting permeate only one of the two components. It should be pointed out that only when the concentration polarization effect is negligible the selectivity expressed by eq 5.17 will be an intrinsic property of the membrane. In general, membrane permeability and selectivity have to be determined experimentally. Since there is a trade-off between membrane permeability and selectivity, Huang and Yeom (1990) introduced a parameter to valuate the performance of a membrane: the pervaporation separation index (PSI), which was expressed as the product of permeation flux and separation factor. Consider that when $\alpha = 1$, no separation occurs, but the corresponding PSI may still be very large if the flux is high, as is the case of a highly porous membrane. Therefore, PSI is redefined as J multiplied by $R - 1$. When PSI is equal to zero it means either zero flux or zero separation. Membrane stability is the ability of a membrane to maintain both the permeability and selectivity under specific system conditions over an extended period

of time. For pervaporation membranes, stability means essentially low swelling in liquid mixtures at different compositions. On the other hand, stable vapour permeation membranes do not have to show degradation at high temperatures and high pressures (up to, respectively, 140°C and 5 bars for ethanol/water separations). Membrane stability is affected by the chemical, mechanical, and thermal properties of the membrane. Since higher operating temperatures lead to higher fluxes (in this sense vapor permeation is preferred to pervaporation process), the membrane stability is of prime importance. Three types of polymer membranes can be used for vapour permeation and pervaporation processes: glassy polymer membranes, rubbery polymer or elastomeric membranes, and ionic polymer membranes. By tendency, glassy polymers are suitable for making water-selective membrane used for solvent dehydration, and rubbery polymer membranes are favorable to the selective removal of organic compounds from water. For the separation of organic mixtures, it is not yet very clear whether glassy or rubbery polymers are more appropriate, and both types of polymers show some pervaporation selectivity. Ionic polymers contain ionic groups that are neutralized by counterions. They may be viewed as crosslinked polyelectrolytes. Ionic membranes, which can be subdivided into cationic and anionic, are normally water selective due to their affinity to water. Ionic polysaccharides have been shown to be potential materials for making dehydration membranes. A membrane with low hydrophilicity generally exhibits a low water flux in dehydration, but some membranes made of polymers with very high hydrophilicity such as poly(vinyl alcohol) (PVA) and poly(acrylic acid) (PAA) need cross-linking for improved stability and selectivity. The polymer materials for dehydration membranes should maintain a proper balance of hydrophilicity and hydrophobicity.

Improvement in membrane performance can often be achieved by polymer modification, for which several techniques have been developed, including cross-linking, grafting, blending, copolymerization, and incorporation of adsorbent materials. Feng (1995) conducted an extensive survey of the pervaporation membranes and separation systems studied in the journal literature during the past half decade; the research work reported in the pre-1990 literature has been documented by Neel (1991). It is shown that currently silicone rubber based polymers (primarily poly(dimethylsiloxane)) are mainly used for the selective permeation of organic compounds from aqueous solutions, and PTMSP and other siliconecontaining polyacetylene derivatives are under development as potential membrane materials. To improve permselectivity, it has been attempted to fill the membrane with organophilic adsorbent. As such, the sorption capacity and/or sorption selectivity will be enhanced due to the adsorbent fillers. However, strong adsorption will cause immobilization of the permeating species, leading to a reduction in permeation flux. Thus, a suitable adsorbent filler should have proper organophilicity, hydrophobicity, and pore size characteristics. Poly(1-(trimethylsilyl)-1-propyne) is an extraordinary glassy polymer. It has $\approx 25\%$ voids which may be linked through chain-to-chain gaps at least 3\AA wide. Gas permeabilities through the polymer are orders of magnitude larger than in other glassy polymers due to its loose microstructure and high mobility of the pendant groups. However, during pervaporation operations, both permeability and selectivity decline with operation time. The problem associated with membrane stability sustained applicability of this unique material for producing industrial pervaporation membranes.

Selection of Polymer Membrane Materials According to the solution-diffusion model, membrane permeability is determined by diffusivity and solubility, and

thus, membrane selectivity is determined by sorption selectivity and diffusion selectivity. While smaller permeating molecules normally exhibit larger diffusivity, the solubility is often influenced by the chemical affinity of the permeating species to the membrane material. Consider the separation of aqueous-organic mixtures where the water molecules are smaller than organic compounds. A hydrophilic membrane favors both solubility and diffusivity for selective permeation of water, while an organophilic membrane must have a large solubility to the organic compound in order to permeate the organic compound preferentially because of the unfavorable diffusion selectivity. This may be the reason that many polymers are selective to water permeation, while only a few are selective to the permeation of organic compounds. Currently, there is no well-established criterion for the selection of membrane materials, and the materials for pervaporation membranes are normally selected empirically. Polymers with high selectivity are often preferred for further study because the disadvantage associated with low permeability can be partly compensated by introducing asymmetry to the membrane structure, thereby reducing the effective thickness of the membrane.

The choice of the membrane strongly depends on the type of application. It is important which of the component should be separated from the mixture and whether this component is water or an organic liquid. Looking at the mixtures to be separated and their compositions, the following different kinds of pervaporation and vapor permeation processes can be distinguished

- Dehydration of organic liquids. For the removal of water from water/organic liquid or vapor mixtures hydrophilic polymers have to be chosen. The hydrophilicity is caused by groups present in the polymer chain that are able to interact with water molecules. Examples of hydrophilic polymers are: ionic

polymers, polyvinylalcohol (PVA), polyacrylonitrile (PAN), polyvinylpyrrolidone (PVPD).

- Removal of organics from water or air streams. For the removal of an organic liquid from water/organic or organic/air mixture hydrophobic polymers are the most suitable polymers as membrane materials. These polymers possess no groups that show affinity for water. Examples of such polymers are: polydimethylsiloxane (PDMS), polyethylene (PE), polypropylene (PP), polyvinylidene fluoride (PVDF), polytetrafluoroethylene (PTFE).
- Separation of two organic solvents. For the mixture of two organic liquids or vapors, again three kinds of mixtures can be distinguished: polar/apolar, polar/polar and apolar/apolar mixtures. For the removal of the polar component from polar/ apolar mixture polymers with polar groups should be chosen and for the removal of the apolar component completely apolar polymers are favorable. The polar/polar and apolar/apolar mixtures are very difficult to separate, especially when the two components have similar molecular sizes. In principle all kinds of polymers can be used for these systems, the separation has to take place on the basis of differences in molecular size and shape, since no specific interaction of one of the two components can take place.

Chapter 6

Bioethanol dehydration

6.1 Bioethanol

Due to an emerging scarcity of the oil resources, it is generally accepted that the fossil sources for our energy supply have to be gradually replaced by renewable substrates. It will complement solar, wind, and other energy sources. One of the most immediate and important renewable of biomass energy systems could be in the fermentation of ethanol from biomass. Biomass has been taken as an interesting energy source for several reasons, among which its important role in reducing the emission of greenhouse gas. Since produced and utilized in a sustainable way, the use of biomass for energy will offset the emission of greenhouse gas from the fossil fuel. Ethanol represents one of the more important resources of renewable energies; moreover the market for fuel grade ethanol is projected to double in the next ten years [2]. Ethanol fuel is widely used in Brazil and in the United States, and together both countries were responsible for 88 percent of the world's ethanol fuel production in 2010 [21]. Most cars on the road today in the U.S. can run on blends of up to 10% ethanol [1], and the use of 10% ethanol gasoline is mandated in some U.S. states and cities. Since 1976 the Brazilian government

has made it mandatory to blend ethanol with gasoline, and since 2007 the legal blend is around 25% ethanol and 75% gasoline (E25). Bioethanol is a form of renewable energy that can be produced from agricultural feedstocks. It can be made from very common crops such as sugar cane, potato, manioc and corn. However, there has been considerable debate about how useful bioethanol will be in replacing gasoline. Concerns about its production and use relate to increased food prices due to the large amount of arable land required for crops,[3] as well as the energy and pollution balance of the whole cycle of ethanol production, especially from corn. Recent developments with cellulosic ethanol production and commercialization may overcome some of these concerns [19]. Cellulosic ethanol could be a really good opportunity because cellulose fibers, a major and universal component in plant cells walls, can be used to produce ethanol [13]. According to the International Energy Agency, cellulosic ethanol could allow ethanol fuels to play a much bigger role in the future than previously thought.

6.2 Conventional distillation

Conventional ethanol production produces 10-15%wt ethanol in water, but to use this ethanol for fuel, its concentration must be greater than 99%wt [6], [16], [9], [10]. The separation of ethanol from water is complicated by the azeotrope that exists at about 95 weight percent ethanol. Distillation is the conventional separation process used for bioethanol dehydration. Distillation consists in separating the constituents of a liquid mixture by partial vaporization and subsequent condensation, taking advantage of differences in volatility. Modern distillation systems are multi-stage, continuous, countercurrent, vapor-liquid contacting systems that are based essentially on the physical laws that state that different materials boil

at different temperatures. Currently, removal of water from ethanol is performed by first distilling the 10 percent ethanol to about 50%wt using a beer still. The ethanol is then distilled in a second column to a concentration of approximately 93%wt [3]. Molecular sieves are typically used to further dehydrate the ethanol to a final concentration of about 99.7%wt ethanol [3]. This separation process has high energy costs and a large footprint.

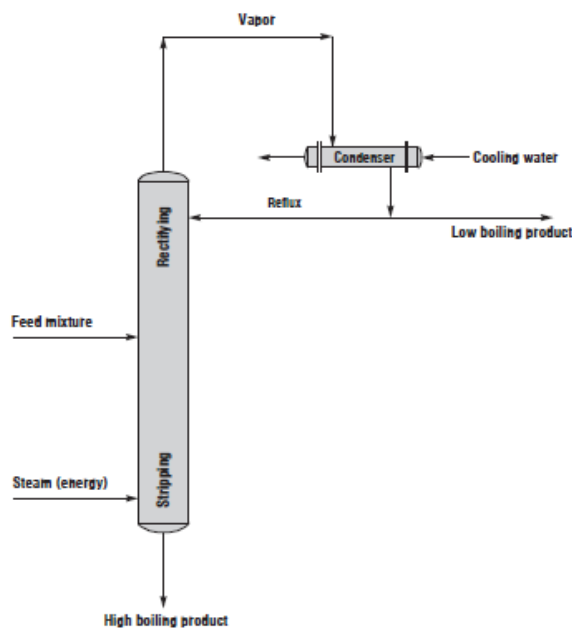


Figure 6.1: Ideal distillation system

An ideal distillation system (figure 6.1) would contain the following elements:

- a feed composed of the two components to be separated,
- a source of energy to drive the process (in most cases, this energy source is steam, either directly entering the base of the tower or transferring its energy to the tower contents through an indirect heat exchanger called a reboiler),

- an overhead, purified product consisting primarily of the feed component with the lower boiling point,
- bottoms product containing the component of the feed possessing the higher boiling point,
- an overhead heat exchanger (condenser), normally water-cooled, to condense the vapor resulting from the boiling created by the energy input. The overhead vapor, after condensation, is split into two streams. Onestream is the overhead product; the other is the reflux which is returned to the top of the tower to supply the liquid down flow required in the upper portion of the tower.

The portion of the tower above the feed entry point is defined as the rectifying section of the tower. The part of the tower below the feed entry point is referred to as the stripping section of the tower. The system shown in figure 6.1 is typical for the separation of a two component feed consisting of ideal, or nearly ideal, components into a relatively pure overhead product containing the lower boiling component and a bottoms product containing primarily the higher boiling component of the original feed. If energy was cheap and the ethanol-water system was ideal, then this rather simple distillation system would suffice for the separation of the beer feed into a relatively pure ethanol overhead product and a bottoms product of stillage, cleanly stripped of its ethanol content [33]. Unfortunately, the ethanol-water (beer) mixture is not an ideal system.

Proven industrial technologies are available for distillation of various grades of ethanol from grain, sugarcane, molasses and other feedstocks. Improvements have been made over the years, particularly during development of the motor fuel grade

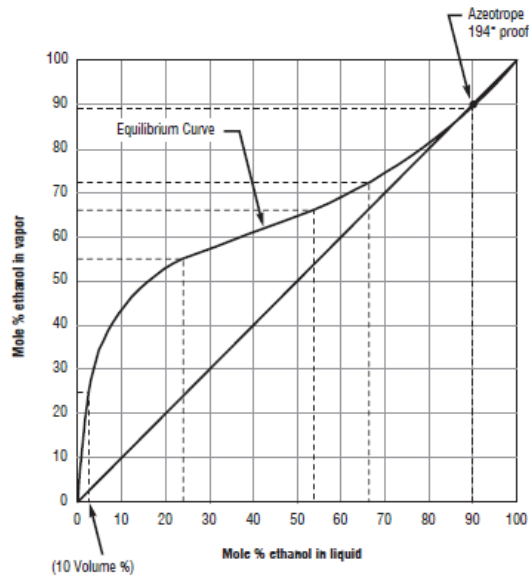


Figure 6.2: Vapor/liquid equilibrium for ethanol-water system at atmospheric pressure ethanol industry. In such installations, a key requirement is the minimization of total energy usage.

Production of industrial ethanol Prior to the emphasis on motor fuel grade ethanol, the major ethanol product utilized worldwide was high purity, hydrous industrial ethanol [22], [23], [25]. Efficient systems have been in commercial operation for many years for the production of such high grade ethanol from ethylene, grain, molasses and sulfite waste liquor. The basic distillation system is shown in figure 6.3. In the case of synthetic ethanol, the beer stripping tower is not required and the refining system is a simple three tower unit, which achieves 98% recovery of the ethanol in the crude feed as a first grade product. The final product may contain less than 5ppm total impurities. For the production of industrial or beverage spirit products made by fermentation of grain, molasses or sulfite liquor, the system utilizes the full complement of equipment shown in figure 6.3 The beer

feed is preheated from the normal fermentation temperature in several stages, recovering low level and intermediate level heat from effluent streams and vapors in the process. This preheated beer is degassed and fed to the beer stripper, which has stripping trays below the beer feed point and several rectifying trays above it. The condensed high wines from the top of this tower are then fed to the extractive distillation tower, which may operate at a pressure of 6 – 7 bars. In this tower, most of the impurities are removed and carried overhead to be condensed as a low grade ethanol stream, from which a small purge of heads (acetaldehyde and other low boiling impurities) may be taken while the primary condensate flow is fed to the concentrating tower. The purified, diluted ethanol from the bottom of the extractive distillation tower is fed to the rectifying tower, which has an integral stripping section. In this tower, the high grade ethanol product, whether industrial or potable, is taken as a side draw from one of the upper trays. A small heads cut is removed from the overhead condensate. Fusel oils (mixtures of higher alcohols such as propyl, butyl, and amyl alcohols and their isomers, which are fermentation by-products or 'congeners') are drawn off at two points above the feed tray but below the product draw tray to avoid a buildup of fusel oil impurities in the rectifying tower. The overhead heads cut and the fusel oil draws are also sent to the concentrating tower. It should be noted that the rectifying tower is heated by vapors from both the pressurized extractive distillation tower and the pressurized concentrating tower. In the concentrating tower, the various streams of congener-containing draws are concentrated. A small heads draw is taken from the overhead condensate, which contains the acetaldehyde fraction along with a small amount of the ethanol produced. This may be sold as a by-product or burned as fuel. A fusel oil side draw is taken at high fusel oil concentrations through a cooler to a

washer. In the washer, water is utilized to separate the ethanol from the fusel oil, with the washings being recycled to the concentrating tower. The decanted fusel oil may be sold as a by-product. The ethanol recovered from the crude streams is taken as a side draw from the concentrating tower and fed back to the extractive distillation tower for re-purification and recovery of its ethanol content.

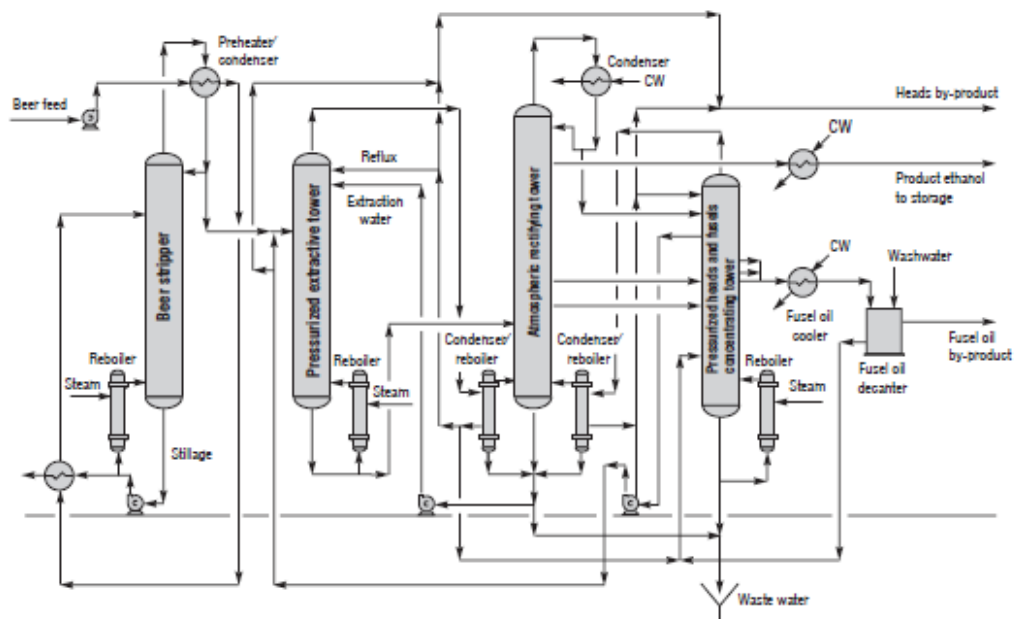


Figure 6.3: Low energy-consuming high grade hydrous ethanol distillation

Production of anhydrous ethanol Systems have been designed and installed for production of extremely dry and very pure anhydrous ethanol for food and pharmaceutical use, primarily in aerosol preparations. These systems, as shown in figure 6.4, yield ethanol containing less than 200 ppm water. The two tower dehydrating system has been operated in two super-anhydrous plants in Canada, and was used to produce motor fuel grade ethanol [18]. The dehydrating tower and the entrainer recovery tower are operated at atmospheric pressure. Thus, they may utilize either low pressure steam, hot condensate or hot waste streams

from other parts of the ethanol process to minimize steam usage. To simplify equipment and minimize investment, a common condensing and decanting system is used for the two towers. The entrainer used to remove water as a ternary (three component) azeotrope may be benzene, heptane (*C6 – C8* cut), cyclohexane, n-pentane, diethyl ether or other suitable azeotropic agents. The entrainer serves to create a three component azeotrope that boils at a temperature lower than any of the three individual components and lower than the ethanol/water binary (two component) azeotrope. Therefore the ternary mixture will pass overhead from the tower, carrying the water upward. Upon condensing, the mixture separates in a decanter into an entrainer-rich layer and a water-rich layer. The hydrous ethanol feed enters the dehydrating tower near the top. The feed contacts the entrainer in the upper section of the tower. The three component mixture in this section of the tower seeks to form its azeotrope, but is deficient in water and contains more ethanol than the azeotrope composition. Therefore, the ethanol is rejected downward in the liquid and is withdrawn as an anhydrous product from the bottom of the tower. The water joins the entrainer, passing upward as vapor to form a mixture that is near the azeotrope composition for the three components. The condensed mixture separates into two layers in the decanter and the entrainer-rich layer is refluxed from the decanter back to the top of the tower. The aqueous layer is pumped from the decanter to the entrainer-recovery tower, in which the entrainer and ethanol are concentrated overhead in the condenser-decanter system. The stripped water, emerging from the base of the tower, may go to waste. If it has substantial ethanol content, it may be recycled to the spirit unit, but this introduces the risk of traces of the entrainer in the hydrous ethanol which may not all be sent to the dehydration system. This system operates with a steam

consumption of 1 – 1.5kg/liter of anhydrous ethanol depending on the quality of product required. As indicated above, a major part of the equivalent steam energy can be provided by hot condensate and hot waste streams from the spirit unit.

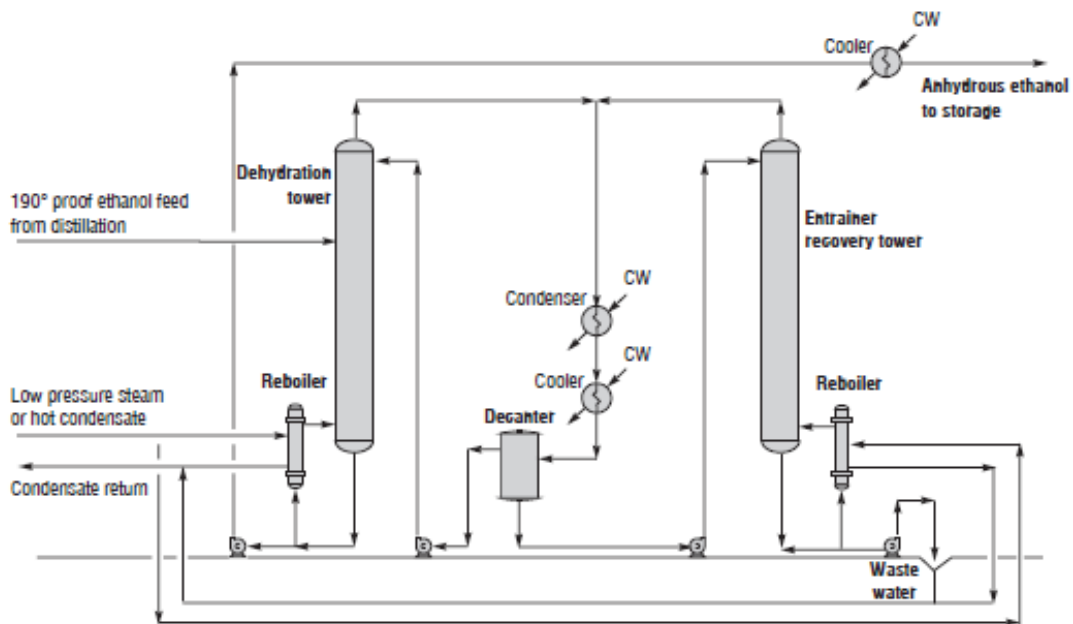


Figure 6.4: High grade anhydrous ethanol system.

6.3 Membrane-based Processes

Conventional separation techniques have high energy costs, so replacing key portions of the process with membranes could provide energy savings [17]. Unfortunately most of current membranes suffer from both plasticization and degradation which negatively impact the membrane performance over time. Polymeric membranes could provide an attractive alternative to the conventional separation techniques. Membrane processes can offer many advantages over traditional separations, namely, higher flexibility, reduced energy requirement, ease of process integration, lower capital and operating costs and small footprint. Both the

molecular sieves and the second distillation column have been targeted as specific components of the process that could be replaced with membrane modules. The estimated energy savings of replacing the current molecular sieve towers with membranes are approximately 3.8%. If the second distillation tower could also be replaced with a membrane module, either the same membrane, or more likely a second membrane module, the energy savings are predicted to grow to approximately 43% over that of current technology. Membranes have been used in ethanol purification plants to break the azeotrope. The membranes typically used for azeotropic separation, such as poly(vinyl alcohol), PVA, cannot be used for lower higher water contents due to plasticization. Plasticization occurs when a considerable amount of a penetrant, such as water or alcohol, is sorbed by the polymer, which swells and dilates, with a consequent increase in the mobility of the polymer chains. The higher chain mobility compromises the size-sieving ability of the polymer, reducing its selectivity. This is particularly true in glassy polymers, whose selectivity is mainly a result of the large differences in the mobility of the penetrants due to the stiffness of the polymer chains. Thus, to achieve an efficient membrane separation, membranes that resist plasticization are needed. For a given ethanol/water mixture a large variety in membrane performance can be observed with various polymers. Table 6.1 gives the selectivity and fluxes of various homogenous membranes for ethanol-water mixtures. It is seen that both the selectivity and flux can range from extremely high to very low. When a highly selective material is selected, membrane performance can be optimized further by reducing the effective membrane thickness. It is best to use a thin film of the discriminating layer deposited on a highly porous support structure. This means that either asymmetric or composite membranes have to be developed with a dense toplayer and

an open porous sublayer. The requirements for the sublayer are such that the resistance for permeate transport must be neglectable compared to the resistance of the toplayer. Therefore, optimization of the sublayer is very important [12]. It might even be worthwhile to develop a three layer membrane consisting of a very porous sublayer, than a nonselective intermediate layer and dense toplayer.

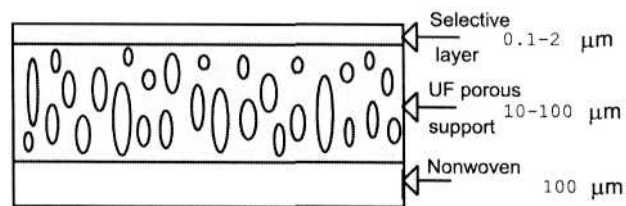


Figure 6.5: Morphology of the pervaporation composite membrane.

Polymer	Flux [$kgm^{-2}h^{-1}$]	α
polyacrilonitrile	0.03	12500
polyacrylamide	0.42	2200
polyvinylalcohol	0.38	140
polyethersulfone	0.72	52
polyhydrazide	1.65	19

Table 6.1: Flux and selectivity of ethanol/water mixture through different homogeneous membranes. Feed: 90% ethanol, temperature: 70°C, membrane thickness= 50 μm

For dehydration, where the small molar volume favors the preferential sorption of water, materials have to be selected with a higher affinity for water than for the other component. For instance, the commercial dehydration membrane PERVAP 1000(SULZER Chemtech Membrantechnik AG, Germany) is a composite membrane with a PAN sublayer and a thin crosslinked PVA skin as a selective layer. Both PVA and PAN show a much higher affinity for water than for ethanol. The

composite membranes can be produced either in a flat configuration (figure 6.6) or in a tubular configuration (figure 6.7).

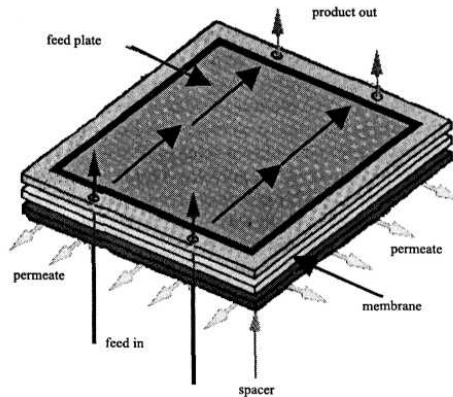


Figure 6.6: Schema of a plate-and-frame module.

Membranes have to be incorporated into modules in order to be used in the process. The main module designs are the plate-and-frame system and the spiral-wound system that are based on the flat membranes and the tubular, capillary and hollow fiber modules that are based on the tubular membrane configuration. Plates made of stainless steel form the feed channels and compartments, which are sealed to the membranes by gaskets. The membranes are supported by stainless steel perforated plates and spacers, which form the permeate channels. The latter ones are open to all sides, allowing for a fast and easy removal of the permeate. The arrangement assures a uniform, parallel flow of the feed mixture over all membranes in a module. The spiral wound modules are flat sheets arranged in parallel to form a narrow slit for fluid flow. In a typical construction two flat membrane sheets are placed together with active sides facing the feed spacer. The feed spacer is placed outside the membrane and forms the feed channel. The whole

assembly is roled around the centre tube in a spiral and fitted inside the appropriate housing. Such configuration is compact and relatively inexpensive. Spiral wound modules are used mainly for organic extraction, with low organic concentration and lower temperatures. Hollow fiber modules are made for a small scale but their applications are limited because of the concentration polarization inside the fibres. All type of modules are commercially available today from several companies The market leader is Sulzer Chemtech Membrantechnik AG (former GFT Company) with over 100 pervaporation plants installed worldwide to a mash containing 80 to 85% ethanol followed by vacuum pervaporation to 96wt.%. In the late 1970s and early 1980s other integrated distillation/pervaporation plants were built in Europe and Asia.

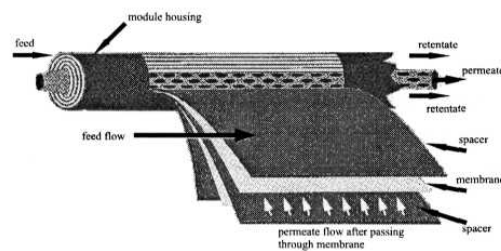


Figure 6.7: Schema of a spiral-wound module.

Chapter 7

Thermally Rearranged Polyimides

Aromatic polybenzoxazoles (PBOs) display excellent thermal stability and very good solvent and chemical resistance. They have a rigid-rod structure with high-torsional energy barriers to rotation between two individual phenylene-heterocyclic rings; these features are interesting for separation membranes since they yield very stiff polymer chains which could lead to high differences in mobility of penetrants based on size which would yield high selectivities. Unfortunately the synthesis of these materials is very difficult; they are soluble only in strong acids (e.g., sulfuric, methane sulfonic, triflic, and polyphosphoric acids). In 1999 Tullos and his coworkers found [37] that an aromatic polyimide containing a hydroxyl group positioned in ortho to the heterocyclic imide nitrogen, rearranged to another structure with a loss of carbon dioxide, upon heating above 400°C in an inert atmosphere. Elemental analysis, solid state n.m.r. and infrared spectroscopy suggested that the most likely formed structure was a polybenzoxazole. Furthermore the formation of benzoxazoles from the hydroxy-containing imide model compound and polyimide supported the generality of the reaction. The resulting thermally rearranged (TR) film, like polybenzoxazole films, displayed excellent solvent resistance and very good thermal stability.

Thermal conversion of hydroxy-containing polyimides to polybenzoxazoles could provide an alternative and powerful method for producing polybenzoxazole films and fibers, difficult to obtain otherwise. Infact in the past years the application of this class of materials as gas separation membranes was limited, as we have said, by their lack of solubility in common solvents, which effectively prevents them from being prepared as thin membranes by solvent casting, which is the most widely practiced method for membrane preparation. Ho Bum Park [28] has found by small angle X-ray scattering (SAXS) that TR polyimides are generally amorphous and that they also show a very particular free volume distribution due to the spatial rearrangement of the rigid polymer chain segments in the glassy phase.

It is known that a rearrangement, such as intramolecular cyclization, in glassy polymers could lead to changes in polymer structure for gas transport. In particular, phenyleneheterocyclic ring units in TR polyimides have a flat, rigid-rod structure with high torsional energy barriers to rotation between two rings. The stiff, rigid ring units in such flat topologies pack efficiently, leaving very small free-volume elements accessible to penetrant molecules. During the thermal rearrangement, two types of change in chain structure occur that alter chain packing:

- random chain conformations resulting from the formation of meta- and para-linked chains;
- relatively flexible, twisting pairs of short flat planes (A and B figure 7.1) that convert to single long flat planes that are much more rigid than those of the parent moieties.

It is worth to point out that the structural rearrangements occurring during this process do not correspond to partial burning (or carbonization) of the initial

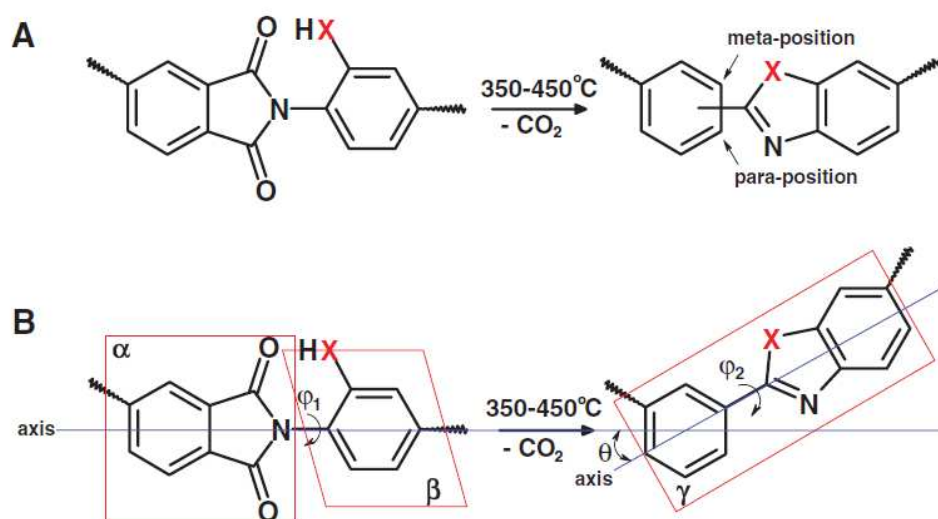


Figure 7.1: Thermal rearrangement process

polymer structure, a process that has been used in other cases to enhance gas separation properties of polymers. If managed properly, these changes in chain conformation and topology create wellconnected, narrow size distribution free-volume elements (also known as cavities) appropriate for molecular separations. Dense membranes prepared from TR polyimides have shown excellent CO_2/CH_4 separation characteristics with both high selectivity and permeability due this unusual microstructure, high free volume and rigid chains. These TR polymers also exhibit extremely high plasticization resistance in mixed gas experiments which is expected due to their PBO/PBT structure. The performance of these materials is between that of typical polymer films and carbon molecular sieves. They are tough, ductile and robust unlike carbon molecular sieves which are brittle, fragile materials.

There are two big advantages to TR polyimides. First, the original initial polyimides are soluble in common solvents; that is, they can be prepared in the form of hollow fibers and then exposed to heat treatment to rearrange in TR polymers. Second, it is much easier and simpler to coat these polymers without any defects or cracks onto microporous ceramic support membranes than to coat zeolite, silica, and carbon membranes onto such supports. The excellent gas separation results of Park's work are promising for ethanol-water systems. The size-sieving microstructure should allow a high rate of water transport while retaining the ethanol on the upstream side of the membrane, permitting energy efficient dehydration of ethanol. Furthermore, the high CO_2 plasticization resistance confirms the expected PBO/PBT stability and suggests that the membranes should also show high resistance to water plasticization. Finally the PBO/PBT structures are expected to have a high resistance to hydrolysis even at elevated temperatures and

pressures. However, there are no known reports of using such materials for ethanol dehydration. In applying this polymer system to the dehydration of ethanol, there are several variables that can be used to optimize performance. First, the structure of the polyimide or polyamide precursor, and thus the resulting PBO/PBT, can be changed to increase the water flux of the membrane while retaining high water/ethanol selectivity. Second, the synthesis route of precursor polymers of the same chemical structure has been shown to influence the gas separation properties and may also influence water-ethanol transport properties. Finally, the thermal treatment method used to convert to the final PBO or PBT will influence the fraction of the polyimide units that rearrange. The optimum combination of structure, synthesis route and rearrangement conditions have to be determined.

Chapter 8

Materials And Methods

8.1 Polymer Synthesis

Polyimides were prepared by a conventional two-step process involving formation of the polyamic acids followed by thermal dehydration to the polyimides in solution. Polyimides which became insoluble upon solution dehydration were manipulated as polyamic acid solutions to form films. PMDA ODA, BPDA ODA and BTDA ODA polyimides were synthesized by solid state thermal imidization, KAPTON commercial film was used as received; HAB BPDA gave insoluble polyimide and so thermal imidized in solid state; HAB 6FDA gave soluble polyimide so thermal imidized in solution. All the monomers were purified before polymerization. BPDA, BTDA and PMDA dianhydrides were purified in a vacuum oven at different temperatures between 180°C and 220°C over night; ODA diamine was dried at 95°C under full vacuum over night; APAF diamine was purified by recrystallization in methanol and water and then dried at 95°C under full vacuum over night. DMAC (N,N-dimethylacetamide) and NMP (N-Methyl-2-pyrrolidone) were distilled over calcium hydride just prior to use. Diamines and dianhydrides were added in 1 : 1 molar ratio. For example, to a 500 ml flask purged with nitrogen were added

4.004 g of ODA (20.00 mmol) and 20.5 ml of DMAC; the mixture was mechanically stirred at room temperature until the diamine was completely dissolved and a clear solution was formed. To this solution were added 4.3624 g of PMDA (20.00 mmol) and 20.5 ml of DMAC in order to achieve 20% (weight/volume) solids content. The reaction was carried out at room temperature for 24 h to give a viscous polyamic acid solution. In the case of APAF ODPA, 7.32 g (20 mmol) of APAF were dissolved in 33.81 ml of NMP; when APAF was dissolved, the three-necked flask containing the monomer and the solvent was put in an ice bath. After diamine dissolution 6.204 g of ODPA and 33.81 ml of NMP were added and the solution was stirred one night at room temperature; 27.048 ml of ODB (o-dichlorobenzene) and 40.572 ml of NMP were added to the flask to achieve 10% (weight/volume) solids content in an ODB/NMP (20/80 volume/volume) mixed solvent. The polyamic acid was thermally cyclized to the corresponding polyimide by heating the mixture to 180°C for 24 h under reflux. Water was removed as the ODB/water azeotrope using a Dean-Stark trap. The cooled polymer solution was precipitated in a blender using a 50/50 by volume methanol/water solution. The precipitated polyimide was filtered, washed several times with water, allowed to dry at room temperature for 24 h, and then finally dried under vacuum at 200°C for at least 2 days.

8.2 Membrane Preparation

Dense polyimide films were prepared by controlled solvent evaporation. In the case of PMDA ODA, BPDA ODA, BTDA ODA and HAB BPDA the correspondent polyamic acid solutions were diluted with DMAC to a final concentration of 5% polyamic acid in DMAC; for APAF ODPA a polymer solution approximately 3wt%

in DMAC was prepared. The solutions were filtered through a $5\mu\text{m}$ PTFE syringe filter and cast onto a clean glass plate previously leveled inside a vacuum oven; upon the plate, a glass circumference (12cm diameter) was sealed with some silicon to prevent the solution spillage out of the glass plate. The solvent was slowly evaporated according to the following heat treatment:

- at least 5h at 80°C ;
- 100°C overnight;
- 2h at 150°C under full vacuum;
- 2h at 200°C under full vacuum;
- 2h at 250°C under full vacuum;
- 280°C overnight under full vacuum.

Upon cooling, the round membranes were removed from the glass plates. Finally, the homogeneous polyimide membranes with uniform thickness were obtained and cut to fit the pervaporation cell. The final film thickness, measured with a digital micrometer (Mitutoyo, Model ID-C112E) readable to $\pm 1\mu\text{m}$ ranged from $25\mu\text{m}$ to $40\mu\text{m}$. For each film sample, thickness was measured at a minimum of 20 different points within the effective permeation area, and the average value was used for calculation. APAF ODPA and HAB BPDA polyimides films were thermally rearranged into the corresponding polybenzoxazole film in a Carbolite Split-Tube Furnace (see figure 9.1) with N_2 purge maintained throughout rearrangement. The furnace was programmed to the heating cycle shown in figure 8.2: the sample was maintained 1h at 300°C to let residual solvent to evaporate

and then thermally rearranged to the desired temperature for a desired period of time. The following naming convention states: $TRT_2 - t_2$, i.e. TR sample maintained for time t_2 at temperature T_2 .

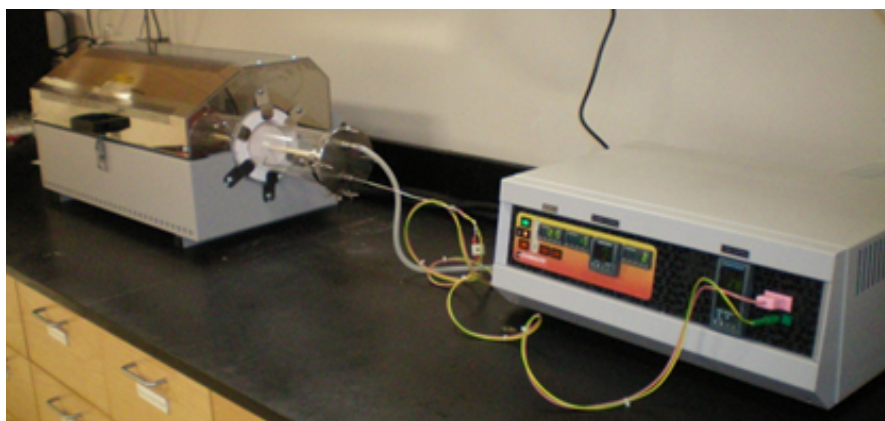


Figure 8.1: Furnace used for thermal treatment

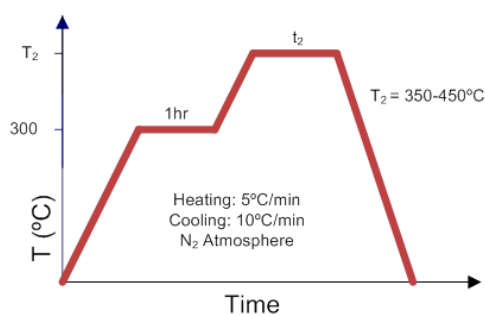


Figure 8.2: Heating protocol

Tables 8.1 and 9.1 summarize all membranes tested.

8.3 Characterization Techniques

In this section the principal characterization techniques with relative conditions adopted are described. FTIR, TGA and DSC analysis were used both to charac-

Polyimides	thickness [micron]
BTDA ODA	40.0 ± 1.8
BPDA ODA	28.5 ± 1.9
PMDA ODA	34.8 ± 2.1
KAPTON	25.0 ± 0

Table 8.1: Polyimide membranes

BPDA HAB and corresponding TR	thickness [micron]
BPDA HAB	25.8 ± 2.7
BPDA HAB TR 4501h	33.3 ± 3.2
BPDA HAB TR 4502h	34.4 ± 2.7
BPDA HAB TR 4504h	33.9 ± 2.6
BPDA HAB TR 5001h	29.2 ± 1.8
ODPA APAF and corresponding TR	thickness [micron]
ODPA APAF	33.0 ± 2.1
ODPA APAF TR400 1h	40.0 ± 1.4
ODPA APAF TR450 15 min	36.0 ± 1.8

Table 8.2: Thermally rearranged membranes

terize the chemistry and the thermal behaviour of the membranes and to confirm, in the case of TR polyimides, the thermal rearrangement to polybenzoxazoles.

8.3.1 Attenuated Total Reflectance Infrared Spectroscopy (FTIR-ATR)

Fourier-transform Infrared Spectroscopy (FTIR) studies were performed using the Attenuated Total Reflectance (ATR) technique with a Nexus 470 Fourier-Transform Infrared Spectrometer from Thermo Nicolet. A total of 256 scans were made for each spectrum, with the resolution of the spectrometer set to 2cm^{-1} .

8.3.2 Differential Scanning Calorimetry (DSC)

Differential scanning calorimetry or DSC is a thermo analytical technique in which the difference in the amount of heat required to increase the temperature of a sample and reference is measured as a function of temperature. Both the sample and reference are maintained at nearly the same temperature throughout the experiment. Generally, the temperature program for a DSC analysis is designed such that the sample holder temperature increases linearly as a function of time. The reference sample should have a well-defined heat capacity over the range of temperatures to be scanned. The basic principle underlying this technique is that when the sample undergoes a physical transformation such as phase transitions, more or less heat will need to flow to it than the reference to maintain both at the same temperature. Whether less or more heat must flow to the sample depends on whether the process is exothermic or endothermic. For example, as a solid sample melts to a liquid it will require more heat flowing to the sample to increase its temperature at the same rate as the reference. This is due to the absorption of

heat by the sample as it undergoes the endothermic phase transition from solid to liquid. Likewise, as the sample undergoes exothermic processes (such as crystallization) less heat is required to raise the sample temperature. By observing the difference in heat flow between the sample and reference, differential scanning calorimeters are able to measure the amount of heat absorbed or released during such transitions. DSC may also be used to observe more subtle phase changes, such as glass transitions.

8.3.3 Thermogravimetric Analysis (TGA)

Thermogravimetric analysis is a type of thermal analysis performed on samples that determines changes in weight in relation to change in temperature. Such analysis relies on a high degree of precision in three measurements: weight, temperature, and temperature change. As many weight loss curves look similar, the weight loss curve may require transformation before results may be interpreted. A derivative weight loss curve can identify the point where weight loss is most apparent. Again, interpretation is limited without further modifications and deconvolution of the overlapping peaks may be required. TGA is commonly employed in research and testing to determine characteristics of materials such as polymers, to determine degradation temperatures, absorbed moisture content of materials, the level of inorganic and organic components in materials, decomposition points of explosives, and solvent residues. It is also often used to estimate the corrosion kinetics in high temperature oxidation.

Simultaneous TGA-DTA/DSC measures both heat flow and weight changes (TGA) in a material as a function of temperature or time in a controlled atmosphere. Simultaneous measurement of these two material properties not only

improves productivity but also simplifies interpretation of the results. The complementary information obtained allows differentiation between endothermic and exothermic events with no associated weight loss (e.g. melting and crystallization) and those that involve a weight loss (e.g. degradation). Thermogravimetric analysis (TGA) scans were obtained in a Q500 thermogravimetric analyzer from TA Instruments, using a heating rate of $5^{\circ}\text{C}/\text{min}$ under nitrogen atmosphere.



Figure 8.3: Thermal Gravimetric Analyzer

8.3.4 Wide Angle X-Ray Scattering (WAXS)

X-ray diffraction probes the structure of the materials at a distance of few \AA . According to this method the sample is scanned in a wide angle X-ray goniometer, and the scattering intensity is plotted as a function of the 2θ angle. X ray diffraction is a non destructive method of characterization of solid materials. When X-rays are directed in solids they will scatter in predictable patterns based upon the in-

ternal structure of the solid. The amorphous domains give rise to diffuse X-ray patterns whereas the crystalline domains yield well-defined sharp peaks, which are characteristic of the crystal geometry. Therefore, the X-ray diffraction is widely used to distinguish between ordered and disordered structures. WAXS measurements were used to justify different pervaporation behaviour of PMDA ODA and its commercial version KAPTON, due to different crystalline domains contents.

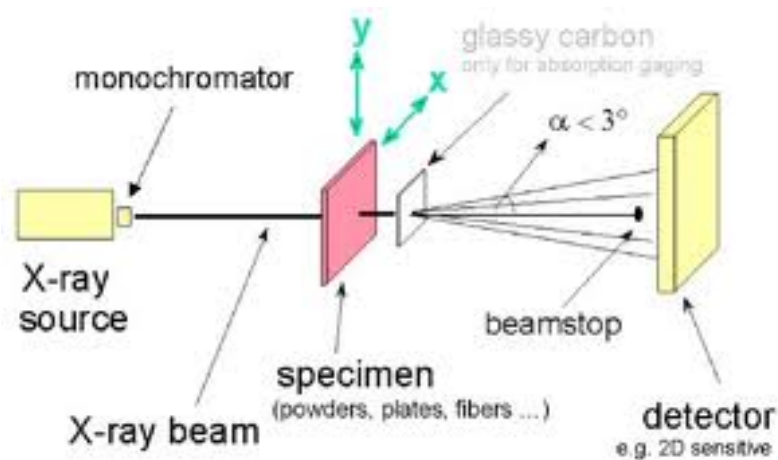


Figure 8.4: Wide Angles X-Rays Scattering

8.4 Experimental Setups and Procedures

8.4.1 Pervaporation tests

Pervaporation apparatus of liquid feeds through flat-sheet membranes is shown schematically in figure 8.5. In the membrane cell, the membrane sample was supported on a porous sintered stainless plate and its active surface area was 42cm^2 . TR polyimides were too brittle and so they were cut from membrane cell edges. Hence, in these cases impermeable aluminum tape was used to mask the film, leaving around 8cm^2 area for permeation. Five minute epoxy (Devcon, Danvers,

MA) was applied at the interface of the tape and the film to prevent any feed leak. This assembly was finally placed in the membrane cell. Vacuum was produced by a vacuum pump in the permeation compartment of the membrane cell. In each permeation test, the feed solution was circulated between the membrane cell and a large feed vessel of about 1.8 litres, whose temperature was kept constant thanks to a thermostated oil circulation bath. A thermocouple positioned on the membrane cell permitted to accurately control the temperature of the feed in contact with the membrane. Pervaporation test were conducted at a feed composition of 90% ethanol by weight and a temperature of 75°C (realized by setting the oil bath temperature at 80°C .) The upstream pressure was the atmospheric pressure (the feed side was liquid) and the downstream pressure was kept inferior to 0.1 torr. The permeate sample was drawn out by the vacuum pump and collected in a cold trap immersed in liquid nitrogen, then analyzed by the gas chromatogram (Agilent 6890 Gas Chromatograph, HP) to obtain the mass fraction of each penetrant component. Once steady-state was achieved, which took different periods of time depending on the polymer, the permeate flux (J) was computed based on the mass of permeate (m_p) collected within a given time interval Δt according to the following equation:

$$J = \frac{m_p}{A\Delta t} \quad (8.1)$$

where A is the membrane area, whose value, as specified above, is different for polyimides and TR polymers. The samples were first weighted and then analyzed by the gas chromatography, to determine the concentrations of water and ethanol. These concentrations were then used to calculate the separation factor of the membrane for components i and j , B_{ij} according to equation 8.2:

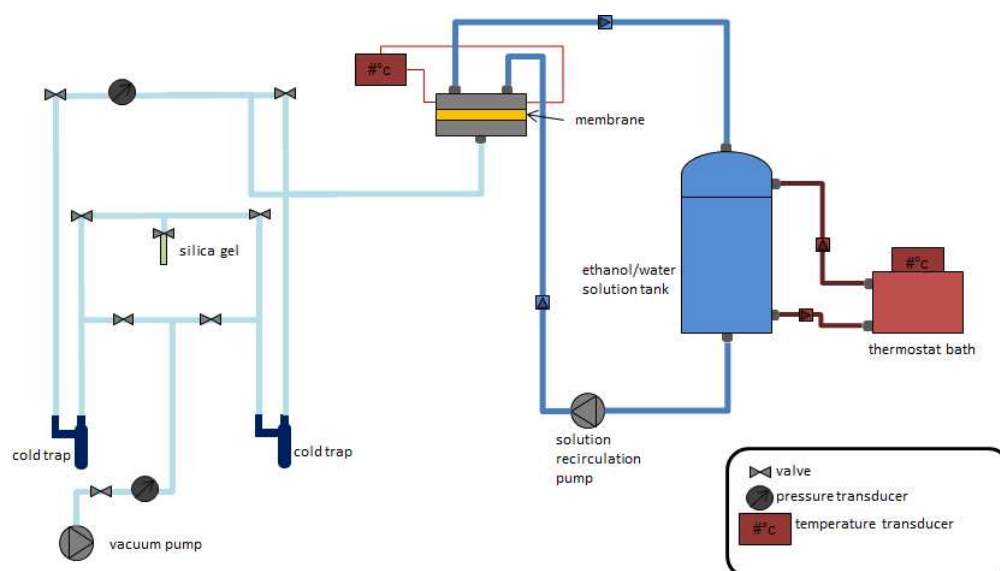


Figure 8.5: Schema of pervaporation apparatus



Figure 8.6: Picture of pervaporation apparatus

$$B_{ij} = \frac{C_i^p/C_j^p}{C_i^f/C_j^f} \quad (8.2)$$

where C is the ethanol concentration expressed in mass fraction. The superscripts p and f refer to permeate and feed samples, respectively. Each sample was analyzed three times. At a given operating condition, feed samples were collected at the beginning and at the end of each run, while 4 – 5 permeate samples were collected, and the results were averaged to determine the membrane flux and separation factor. Traditionally, in the pervaporation literature, different membranes are compared in terms of their flux and separation factor values ([35], [34], [29]). However, these parameters depend not only on the membrane material but also on the adopted operating conditions ([31], [4], [24]). Therefore, to minimize the influence of the operating conditions, different materials can be compared in terms of permeability and permselectivity values. Once the flux and permeate composition are known, the permeability of ethanol in the membrane can be calculated according to the following equation 8.3:

$$\Lambda_i = \frac{JC_i^p L}{MW_i x_i^f \gamma_i P_i^{sat}} \quad (8.3)$$

where L is the membrane thickness, MW_i and P_i^{sat} are the molecular weight and the vapor pressure of component i , respectively, x_i^f is the mole fraction of component i in the feed, and γ_i the activity coefficient of component i in the feed stream, whose value was computed using the NRTL model with parameters given by Gmehling et al [12].

The permselectivity, α , is defined as follows:

$$\alpha_{ij} = \frac{\Lambda_i}{\Lambda_j} \quad (8.4)$$

8.4.2 Stability tests

Chemical and thermal stability of the polymers towards ethanol and water was assessed by exposure to a 50wt% ethanol solution at 120°C and 3 bars (absolute pressure) for four weeks; these exposure conditions simulate the aggressive conditions the membranes might experience in use. Pervaporation tests were repeated after exposure to test the stability of membranes pervaporation properties. Some samples were tested for another week (fifth week) at even more aggressive conditions: a 50wt% ethanol solution at 140°C and 5 bars (absolute pressure). An exposure cell designed for this test is shown in figure 8.7 and schematized in figure 8.8. The exact amount of ethanol-water mixture to obtain the desired pressure at the decided temperature was determined experimentally. Before putting the cell in the oven (at 120°C for the first four weeks and then at 140°C for the fifth week) and everytime it was opened to take the samples and repeat the pervaporation experiments, the cell itself was evacuated to remove the air inside so as to exclude any oxidization effect of the membranes inside. In this way any possible degradation could be attributed only to the effect of the ethanol/water mixture combined with the heat. In addition to the membranes used for pervaporation tests, small pieces of the same polymers (cut from the original round film) were put inside the exposure cell. These pieces were used to perform some TGA and DSC tests after the exposure time. Pictures of this pieces before and after the exposure were taken to record any visual changes (8.9).



Figure 8.7: Exposure cell

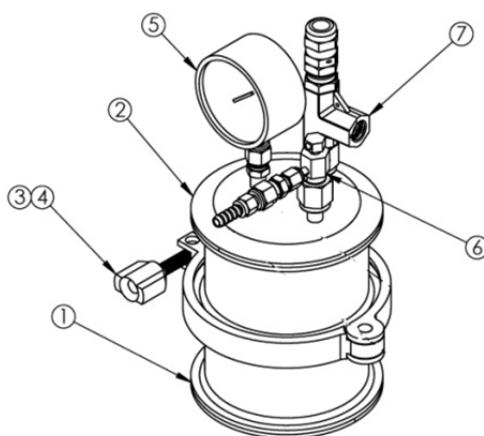


Figure 8.8: Schema of exposure cell: (1) cell bottom; (2) cell top; (3) clamp; (4) Viton gasket with 10 mesh screen; (5) 0 – 100 psig pressure gauge; (6) bleed valve; (7) relief valve

8.4.3 Liquid sorption tests

Liquid sorption tests for pure ethanol and water were measured at 35°C for all polyimides and TR polymers to provide information about the swelling (measured as absorbed amount of pure liquid). A known amount of the polymer film was placed in a sealed glass jar containing the liquid (water or ethanol). The jar was kept in a temperature-controlled circulation water bath. At different times, the film sample was quickly removed from the jar and weighed on an analytical balance after the excess liquid on its surfaces had been wiped off with filter paper. The film sample was placed back into the jar and returned to the water bath. This procedure was repeated until the mass of the film remained constant as a function of time. Before each test, the film samples were degassed overnight at 50°C in a vacuum oven.

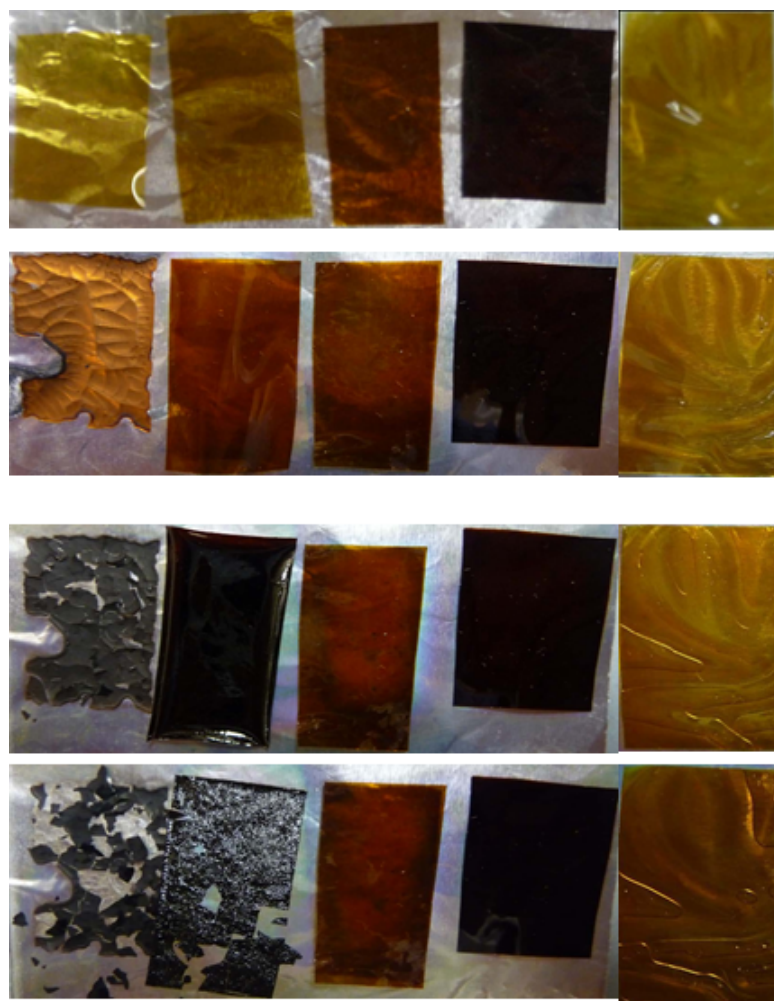


Figure 8.9: Picture of polymeric films before and after exposure

Chapter 9

Results

9.1 Polyimides

In this section results of pervaporation tests, sorption liquids uptake and exposure test for polyimides will be presented.

Polyimides exposed to high temperatures and humidities might be expected to undergo hydrolysis reactions. This hydrolysis reaction results in the formation of polar hygroscopic groups which could degrade the separation properties of the membranes, as we show in this chapter.

9.1.1 Exposure effect on pervaporation properties

Polyimide membranes were tested in the described pervaporation apparatus at the following experimental conditions:

- Feed composition: 90% ethanol by weight
- Feed temperature: $75^{\circ}C$
- Upstream pressure: atmospheric
- Downstream pressure: < 0.1 torr



Figure 9.1: Polyimide membranes tested

Pervaporation tests were performed before and after exposure to a 50/50 by weight ethanol/water mixture at time intervals of 1 week. Exposure conditions were $T = 120^{\circ}\text{C}$ and $p = 3$ bars (absolute pressure) for the first four weeks and $T = 140^{\circ}\text{C}$ and $p = 5$ bars (absolute pressure) for the fifth week. Pervaporation test procedure was as follow: wait until steady state was reached, collect the permeate, weigh it to calculate total permeate flux and calculate permeate composition thanks to a Gas Chromatographer. In table 9.2 all the results are summarized.

As the reader can see from the table above, BPDA ODA and BTDA ODA were tested for four weeks (the last one at different exposure conditions), while PMDA ODA and KAPTON broke after 4 weeks of exposure. Figure 9.3 show the exposure effect on polyimide membranes. A dramatic decrease of selectivity is observed for BPDA ODA and BTDA ODA. Selectivity of BTDA ODA is 11630 ± 1482 before exposure and 514 ± 44 after five week of exposure; it is 3668 ± 416 for BPDA ODA before exposure and 371 ± 39 after the fifth week. A small decrease of selectivity is

Membrane	Exposure period [weeks]	Water permeability [Barrer]	Ethanol Permeability [Barrer]	Selectivity
BTDA ODA	0	$1.17 \pm 0.10 \times 10^3$	$1.00 \pm 0.09 \times 10^{-1}$	11630±1482
	1	$1.00 \pm 0.06 \times 10^3$	$2.87 \pm 0.17 \times 10^{-1}$	3596±306
	2	$1.00 \pm 0.06 \times 10^3$	$7.16 \pm 0.41 \times 10^{-1}$	1420±115
	4	$0.87 \pm 0.05 \times 10^3$	$6.68 \pm 0.40 \times 10^{-1}$	1305±110
	5*	$0.80 \pm 0.05 \times 10^3$	1.55±0.09	514±44
BPDA ODA	0	$5.43 \pm 0.44 \times 10^2$	$1.46 \pm 0.12 \times 10^{-1}$	3668±416
	1	$7.55 \pm 0.56 \times 10^2$	1.03±0.07	735±78
	2	$7.41 \pm 0.55 \times 10^2$	0.91±0.07	813±85
	4	$7.53 \pm 0.55 \times 10^2$	1.83±0.13	412±43
	5*	$7.15 \pm 0.53 \times 10^2$	1.93±0.14	371±39
PMDA ODA	0	$1.67 \pm 0.18 \times 10^3$	2.94±0.31	569±85
	1	$1.60 \pm 0.11 \times 10^3$	3.96±0.28	405±40
	2	$1.60 \pm 0.10 \times 10^3$	3.63±0.44	412±38
	4	---	---	---
KAPTON	0	$5.02 \pm 0.21 \times 10^2$	$7.71 \pm 0.32 \times 10^{-1}$	651±38
	1	$5.21 \pm 0.19 \times 10^2$	$8.95 \pm 0.32 \times 10^{-1}$	583±30
	2	$5.34 \pm 0.19 \times 10^2$	$8.90 \pm 0.32 \times 10^{-1}$	600±31
	4	---	---	---

Figure 9.2: Pervaporation results of polyimides before and after exposure

observed also for PMDA ODA after two weeks of exposure and a selectivity almost constant after the second week of exposure is seen for KAPTON. Both the last two membranes broke during a pervaporation test after four weeks of exposure.

As it is possible to see from figures 9.4 and 9.5, water permeability is almost constant over the whole period of exposure for BTDA ODA and BPDA ODA membranes, while ethanol permeability increases by an order of magnitude. From figure 9.7 and 9.6 it is evident that water and ethanol permeabilities are constant after two weeks of exposure. The difference in permeability values of the two membranes (which are chemically identical) are due to a different cristallinity content (see figures 9.7 and 9.6). KAPTON is partially crystalline, while even if PMDA ODA show some indication of cristallinity, the cristallinity content is clearly less than in KAPTON film.

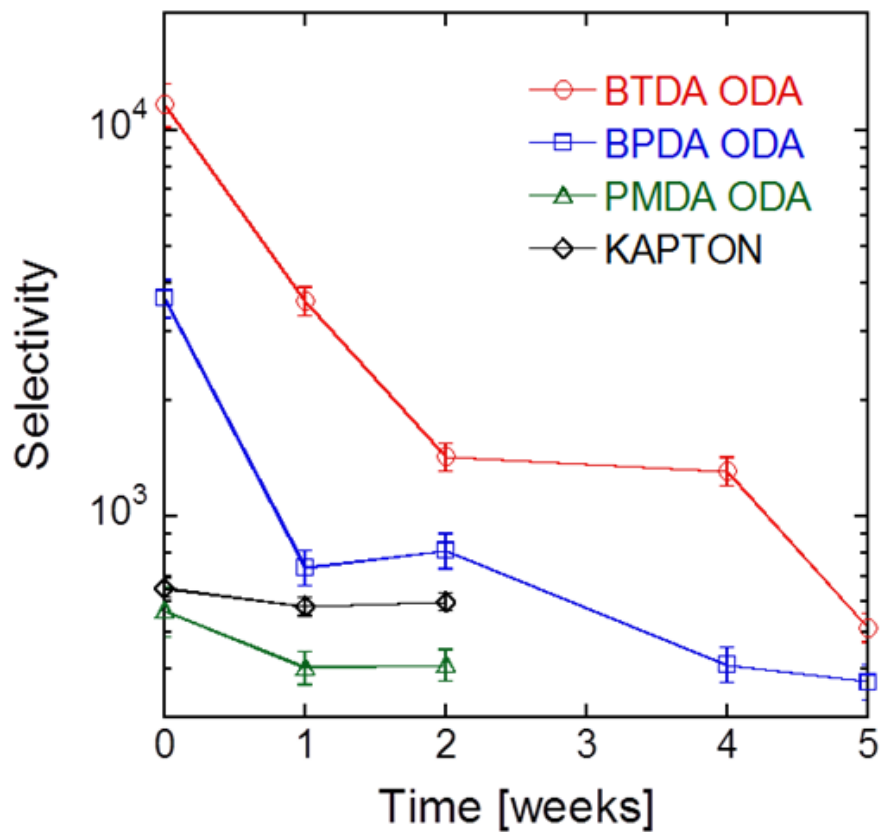


Figure 9.3: Exposure effect on selectivity of polyimide membranes

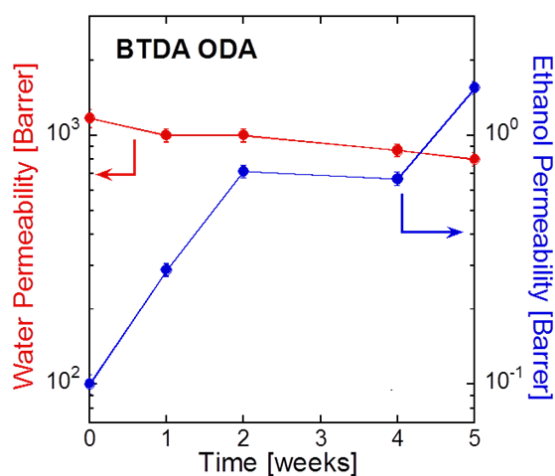


Figure 9.4: Exposure effect on water and ethanol permeabilities of BTDA ODA

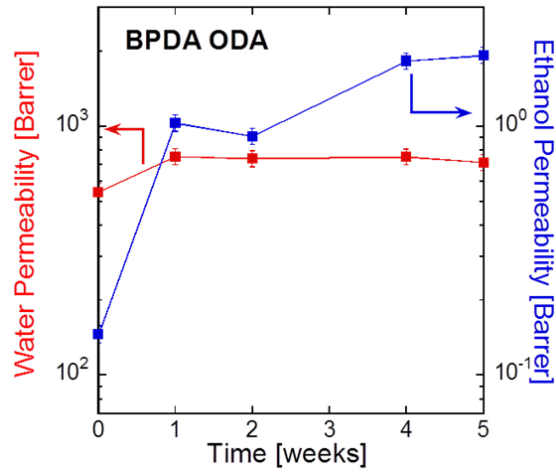


Figure 9.5: Exposure effect on water and ethanol permeabilities of BPDA ODA

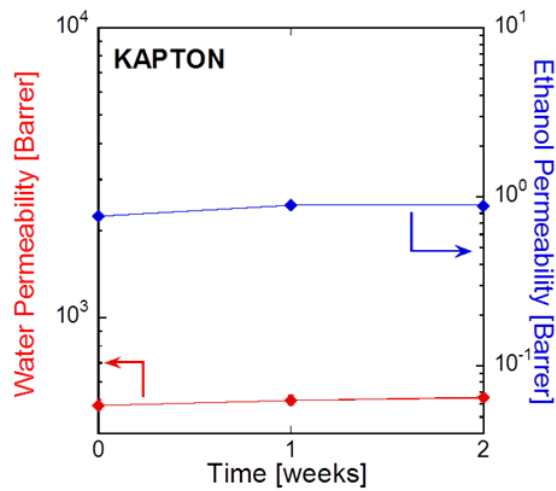


Figure 9.6: Exposure effect on water and ethanol permeabilities of KAPTON

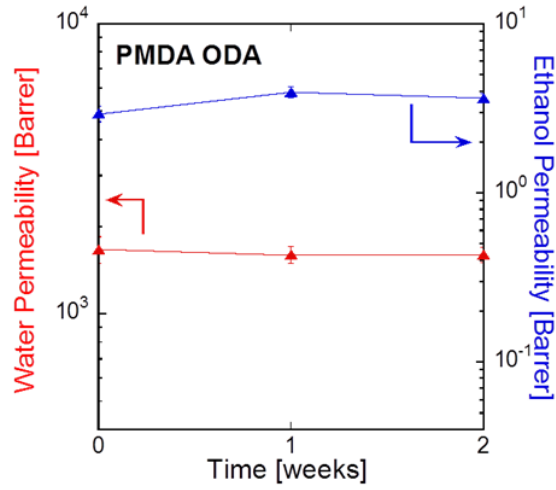


Figure 9.7: Exposure effect on water and ethanol permeabilities of PMDA ODA

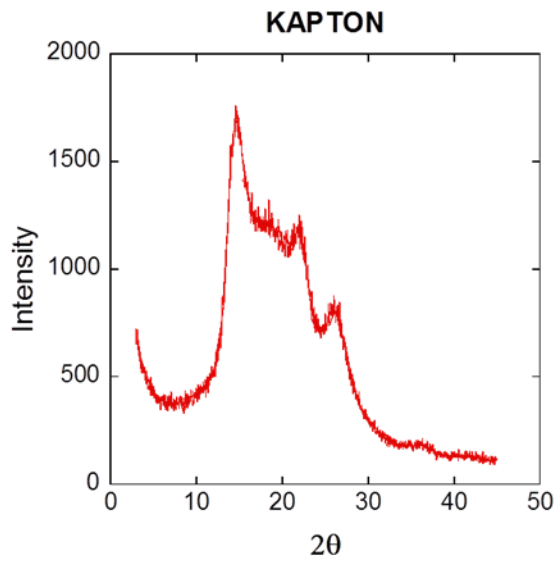


Figure 9.8: WAXS results on KAPTON membrane

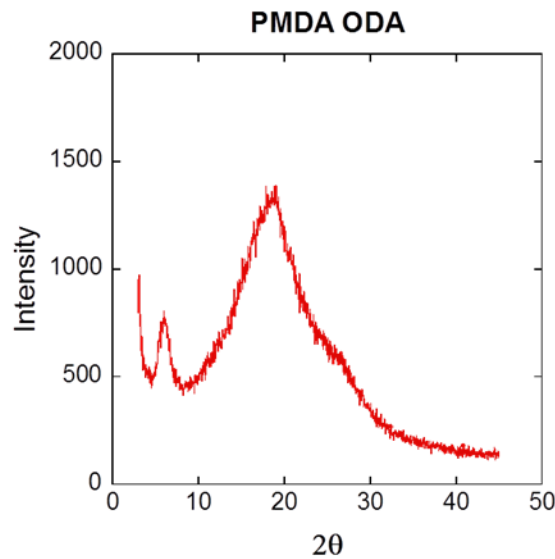


Figure 9.9: WAXS results on PMDA ODA membrane

9.1.2 Exposure effect on chemical stability

TGA results confirm polymer chemical degradation: a peak in the weight derivative curves due to reimidization is seen at temperatures between 150°C and 200°C (figures 9.10 and 9.11).

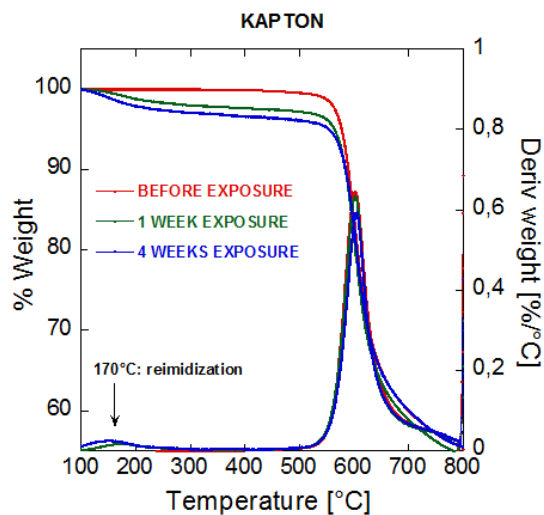


Figure 9.10: TGA results on KAPTON before and after exposure

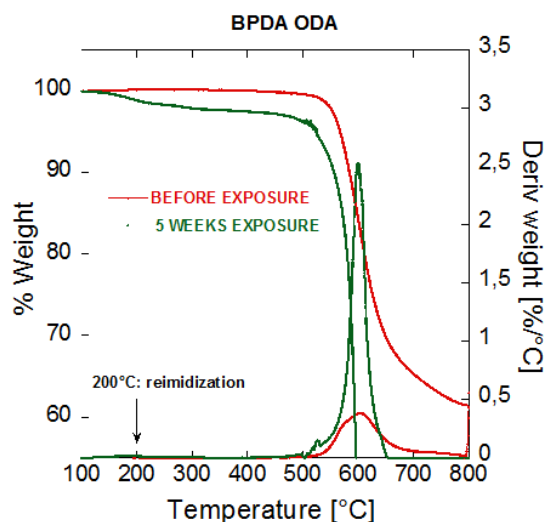


Figure 9.11: TGA results on BPDA ODA before and after exposure

9.1.3 Pure liquids sorption

Polyimides immersed in water reached equilibrium in less than 24h, while at least 100h were needed for samples immersed in pure ethanol. All the polyimides absorbed much more ethanol than water. PMDA ODA and KAPTON can take more ethanol with respect to BPDA ODA and BTDA ODA.

9.2 TR Polyimides

Desired membranes for pervaporation and vapor permeation have high selectivity and permeability. However membranes exhibit a permeability/selectivity tradeoff; commercial polymers, in fact, show properties below the upper bound limit. As we have said polyimides with ortho-positioned functional group can undergo rearrangement at elevated temperatures in an inert atmosphere. These thermally rearranged polymers show very interesting pervaporation and vapor permeation properties, showing both high permeability and high selectivity. The first poly-

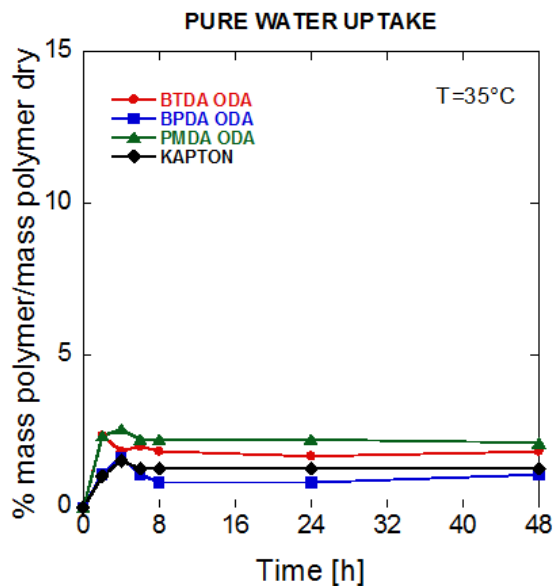


Figure 9.12: Water sorption of polyimides

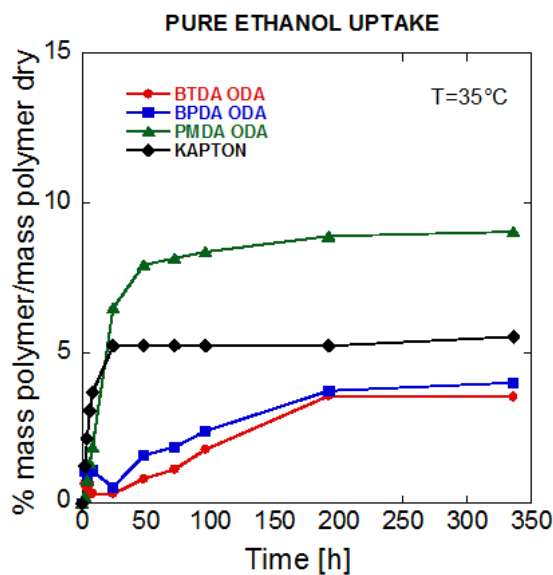


Figure 9.13: Ethanol sorption of polyimides

imide with an *ortho*-positioned *OH* group we tested is BPDA HAB. The thermal conversion was followed thanks to TGA (figure 9.14).

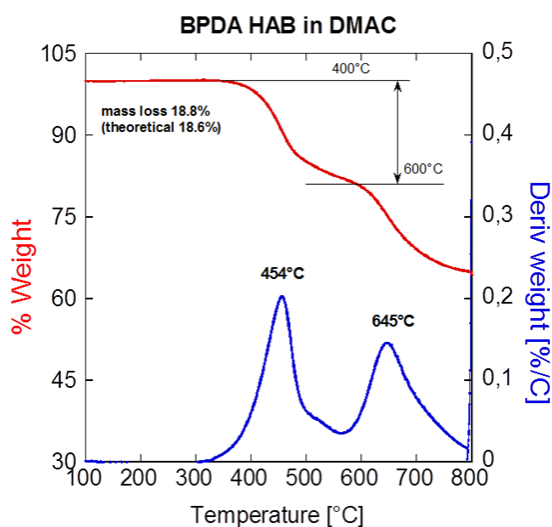


Figure 9.14: TGA evidences of thermal rearrangement of BPDA HAB

In TGA curve, two clear mass loss regions are observed: a thermal rearrangement window between 400°C and 600°C and a decomposition process which begins at very high T (600°C). Theoretically, 2 CO_2 per repeating unit will be removed when the polyimide is completely converted to the polybenzoxazole. Therefore the theoretical mass loss can be calculated using the following equation:

$$\text{theoretical weight loss} = \frac{2 * \text{mol. weight of } \text{CO}_2}{\text{mol. weight of HAB BPDA repeating unit}} \quad (9.1)$$

TR conversion can be controlled by temperature and time. For HAB BPDA, actual mass loss (18,8%) is very close to the theoretical one (18,6%). Only at temperature above the peak temperature (413°C), the TR conversion can approach completion. At very high temperatures (above 450°C), polymer degradation may start: in this case shorter time should be used. High percentage of conversion can

be obtained by holding the polymer at least at 450°C for 1h ;from TGA results there is no evidence of beginning of the decomposition even holding the polymer at 500°C for 1h So high temperatures and long exposure time at these temperature are needed to convert the HAB BPDA. Four different TR membranes were realized (see table 1reftab:TR. In two cases (TR 450 4h and TR 500 1h) extreme conditions of time and temperature were used to ascertain the highest conversion can be reached. As a result, small polyimide residues should exist in these two samples. Assuming that only the rearrangement reaction happens at such processing conditions, the degree of conversion can be calculated from TGA data using the following equation: The conversion results are summarized in table 9.1.

$$\% \text{conversion} = \frac{\text{actual mass loss}}{\text{theoretical mass loss}} \quad (9.2)$$

Temperature [$^{\circ}\text{C}$]	Time [h]	Conversion estimated from TGA
400	1	34%
450	1	78%
450	2	80%
450	4	86%
500	1	96%

Table 9.1: Conversion grade estimated from TGA for BPDA HAB

It should be noted that polymer degradation and carbonization could be occurring at rearrangement temperatures. Moreover, because the polyimide has a very high glass transition (actually no glass transition is visible up to 500°C), it would be very difficult to completely get the solvent out from the membrane. The residual solvent or any kind of degradation result in extra mass loss beyond rearrangement reaction. Therefore the calculated conversion by TGA can be slightly

overestimated. Evidence of thermal rearrangement can be seen also from FTIR, figure 9.16.

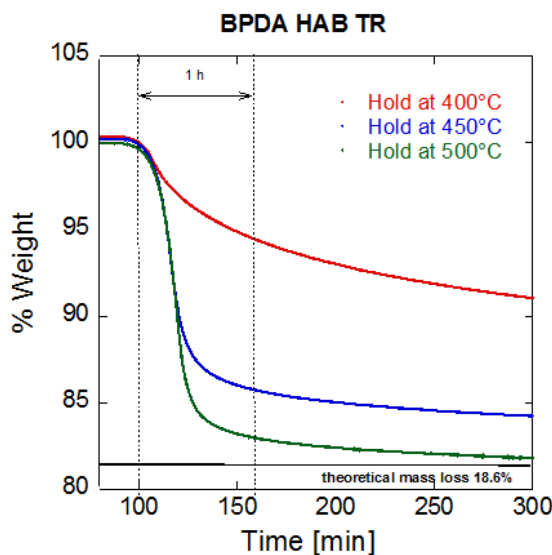


Figure 9.15: Mass loss during thermal rearrangement of BPDA HAB

From FTIR spectra, it is possible to see that increasing time and temperature of TR:

- carbonyl peaks absorbance (1776cm^{-1} and 1716cm^{-1}) decrease;
- benzoxazole ring absorbance (1058cm^{-1}) start to appear after 2 hours at 450°C .

From figure 9.18 it is evident that the higher the thermal conversion, the lower the density of the samples: TR density decreases linearly with conversion. Thermal rearrangement does not move transport properties following a typical permeability/selectivity tradeoff behaviour (figure 9.17)

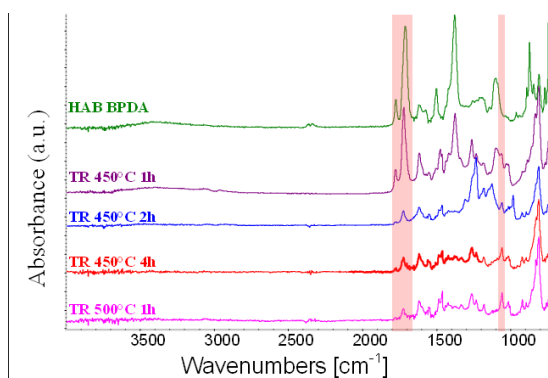


Figure 9.16: Mass loss during thermal rearrangement of BPDA HAB

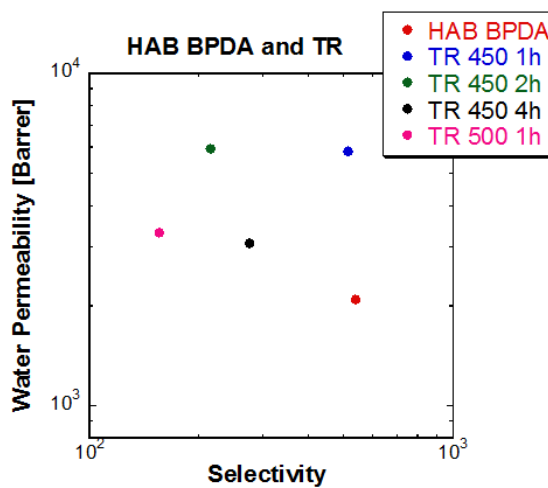


Figure 9.17: Permeability vs selectivity graph of BPDA HAB before exposure

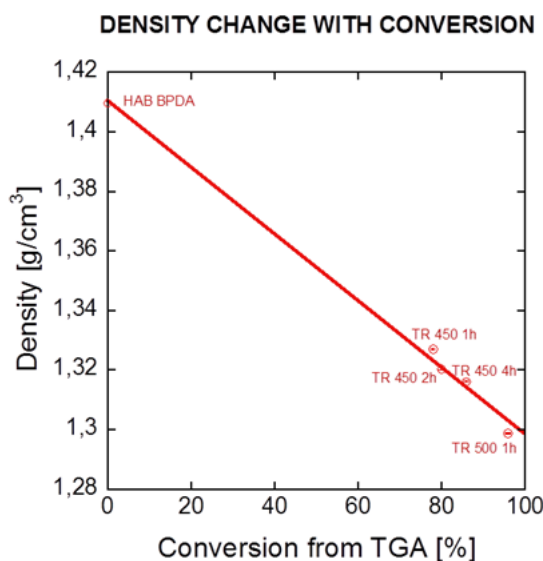


Figure 9.18: Density change of BPDA HAB with thermal rearrangement

9.2.1 Exposure effect on pervaporation properties

TR polyimides were exposed to a 50/50 by weight ethanol/water mixture; exposure conditions used were the same used for polyimide, i.e. 120°C and 3 bars (absolute pressure). HAB BPDA sample was too brittle to make a test after 1 week of exposure. TR 450 1h and TR 450 2h showed poor mechanical properties after 1 week of exposure; they became so brittle that was impossible to perform a pervaporation test after one week of exposure. The only two sample tested after one week and after two weeks of exposure were TR 450 4 h and TR 500 1 h.

For TR 450 4 h and TR 500 1 h selectivity remains constant after one week of exposure and decrease after two weeks.

9.2.2 Exposure effect on chemical stability

TGA curves after one week and after two weeks of exposure are superimposed for TR $500^{\circ}\text{C}1\text{h}$, showing that the two samples seem to show the same grade of

Membrane	Exposure period [weeks]	Water permeability [Barrer]	Ethanol Permeability [Barrer]	Selectivity
HAB BPDA	0	$2.08 \pm 0.09 \times 10^3$	3.85 ± 0.16	540 ± 32
HAB BPDA TR 450 1h	0	$5.82 \pm 0.79 \times 10^3$	11.3 ± 1.5	515 ± 99
HAB BPDA TR 450 2h	0	$5.91 \pm 0.63 \times 10^3$	27.4 ± 2.9	216 ± 33
HAB BPDA TR 450 4h	0	$3.07 \pm 0.40 \times 10^3$	11.1 ± 1.4	276 ± 51
	1	$2.61 \pm 0.35 \times 10^3$	11.8 ± 1.6	241 ± 41
	2	$2.85 \pm 0.33 \times 10^3$	29.7 ± 3.4	96 ± 15
HAB BPDA TR 500 1h	0	$3.31 \pm 0.34 \times 10^3$	21.2 ± 2.2	156 ± 22
	1	$3.88 \pm 0.53 \times 10^3$	21.5 ± 2.9	181 ± 35
	2	$3.27 \pm 0.38 \times 10^3$	34.0 ± 3.9	96 ± 16

Figure 9.19: Pervaporation results of TR polyimides before and after exposure

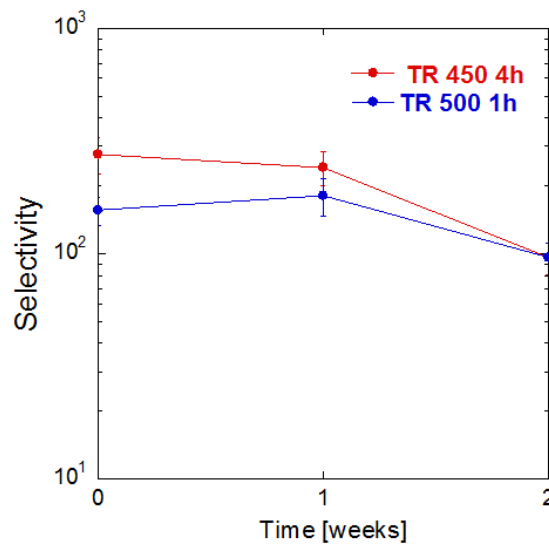


Figure 9.20: Exposure effect on selectivity of TR polyimides

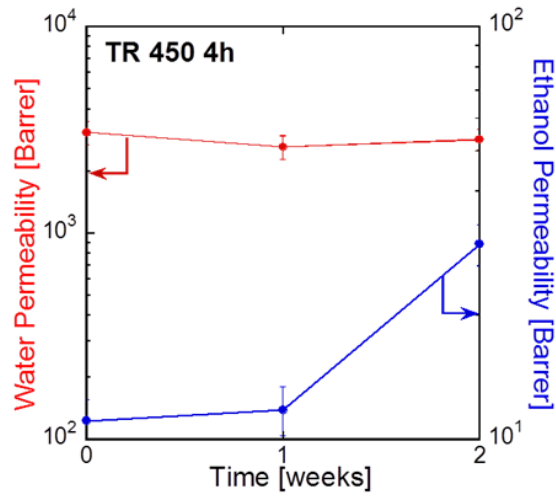


Figure 9.21: Exposure effect on permeability of TR4504h

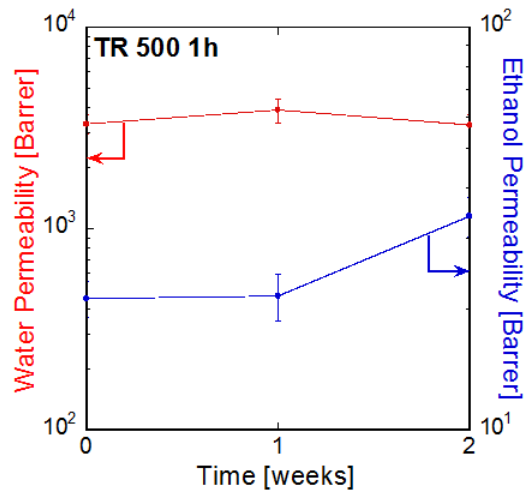


Figure 9.22: Exposure effect on permeability of TR5001h

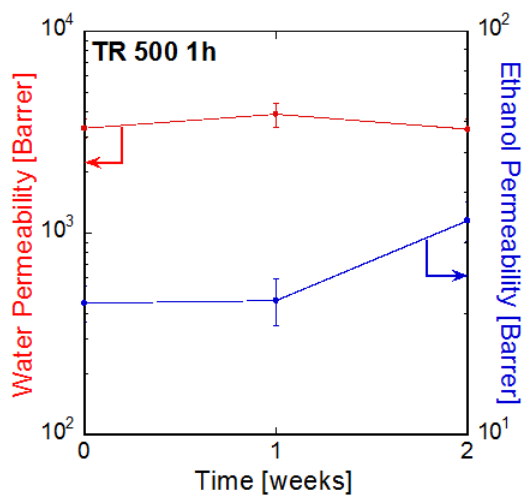


Figure 9.23: Exposure effect on permeability of TR5001h

degradation.

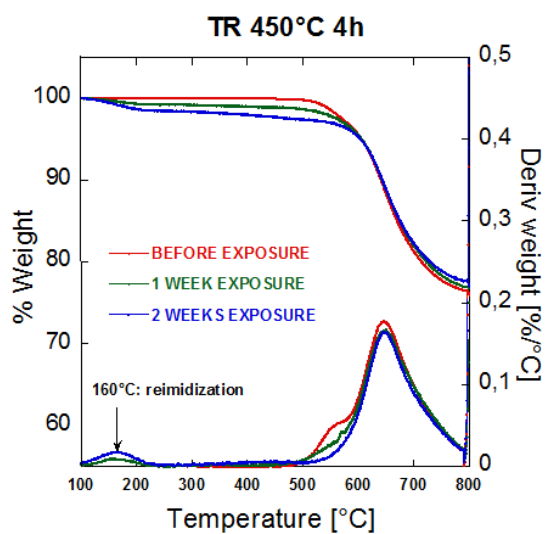


Figure 9.24: Exposure effect on chemical stability of TR 450

9.2.3 Pure liquids sorption

TR polymers can take much more ethanol than water. Among all TR polymers, TR 450°C 4h is the best one in terms of pure ethanol uptake

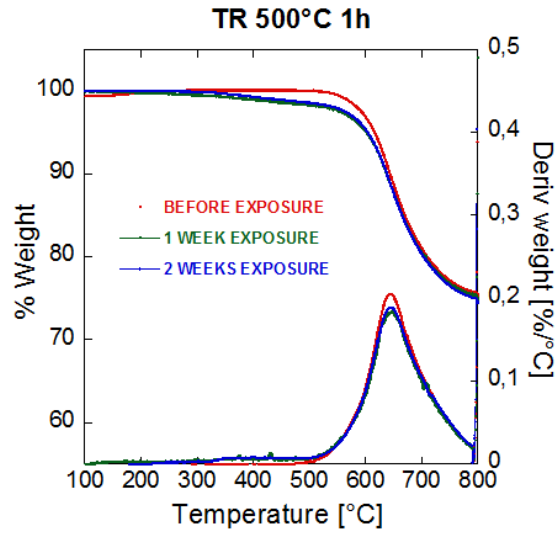


Figure 9.25: Exposure effect on chemical stability of TR 500

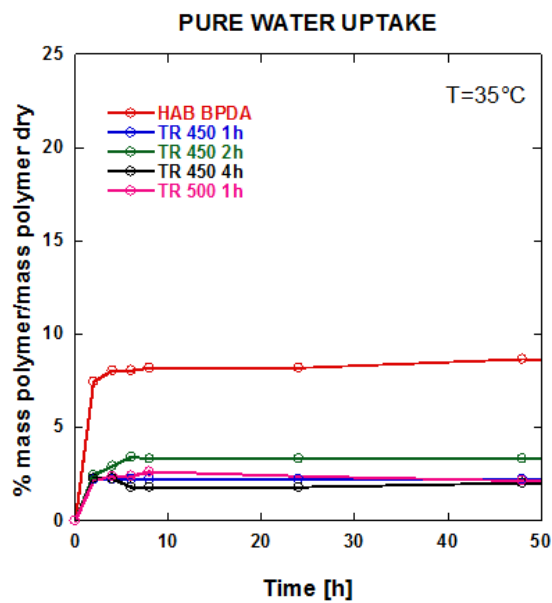


Figure 9.26: Water sorption of TR polyimides

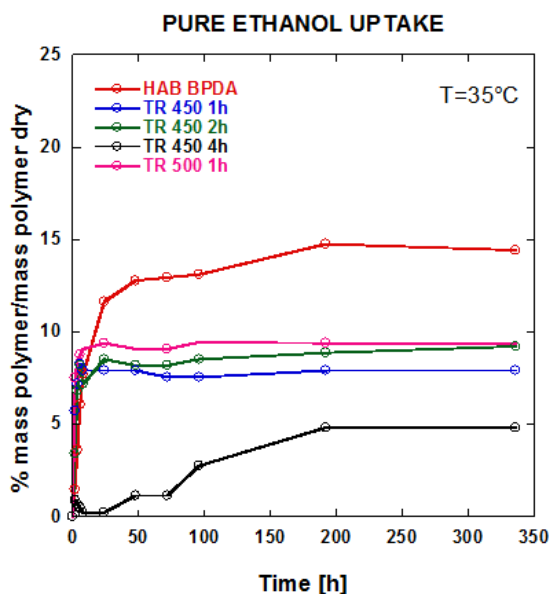


Figure 9.27: Ethanol sorption of TR polyimides

9.3 Conclusions

All polyimides tested (BPDA ODA, BTDA ODA, PMDA ODA and KAPTON) suffered from hydrolysis reaction at high temperature and humidity: in particular polyimides with BTDA dianhydried show the biggest decrease in selectivity, while polyimides with PMDA dianhydried seem to be more stable. All polyimides can take more ethanol than water: BPDA ODA and BTDA ODA can take less water ($< 2\%$) and less ethanol ($< 4\%$) with respect to PMDA-based polyimides. TR polyimides show very high water-permeability and enough water-ethanol selectivity for practical purposes. HAB BPDA TR 450°C 4h show the smallest water ($< 2\%$) and ethanol ($< 5\%$) uptake; However they suffer from hydrolysis at high temperature and humidity due to the presence of residual precursor. More easily convertible hydroxy-containing polyimides (APAF ODPA, HAB 6FDA) should not suffer from this stability issue. Preliminary studies about APAF ODPA as

potential candidate for bioethanol dehydration membranes are shown below.

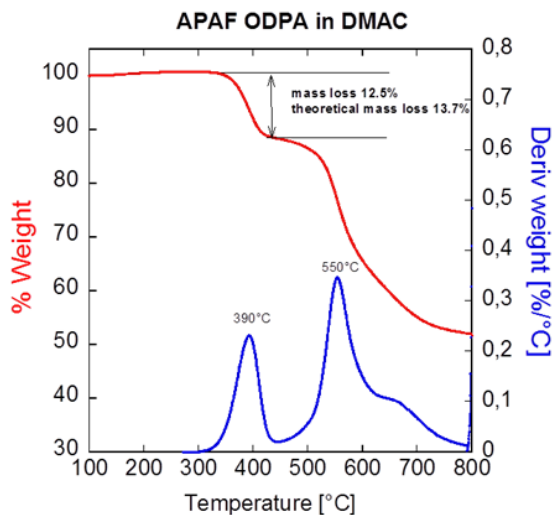


Figure 9.28: Mass loss evidence of thermal rearrangement of APAF ODPA

TGA show a peak temperature at 390°C , and a thermal conversion almost complete holding the sample at 400°C for 1h. At 450°C polymer degradation can occur

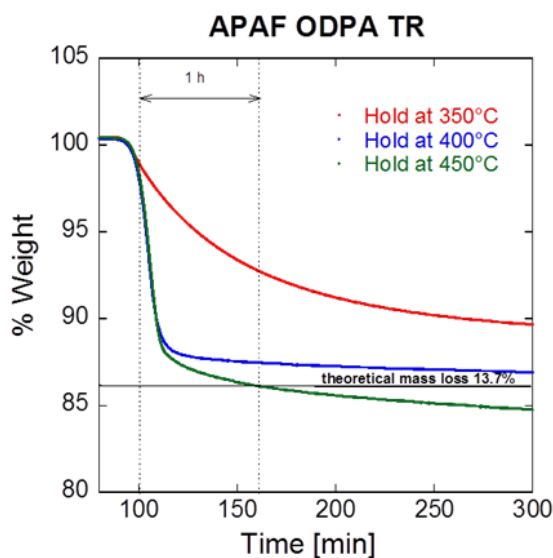


Figure 9.29: Thermal rearrangement of APAF ODPA

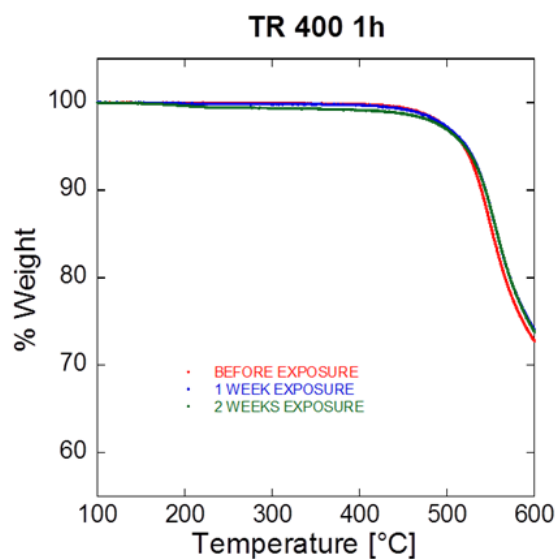


Figure 9.30: Exposure effect on chemical stability of APAF ODPA TR 400 1h

TGA after exposure at usual conditions (120°C and 3 bars at 50/50 by weight ethanol/water mixture), show very small or no evidence at all of chemical degradation after 2 weeks of exposure.

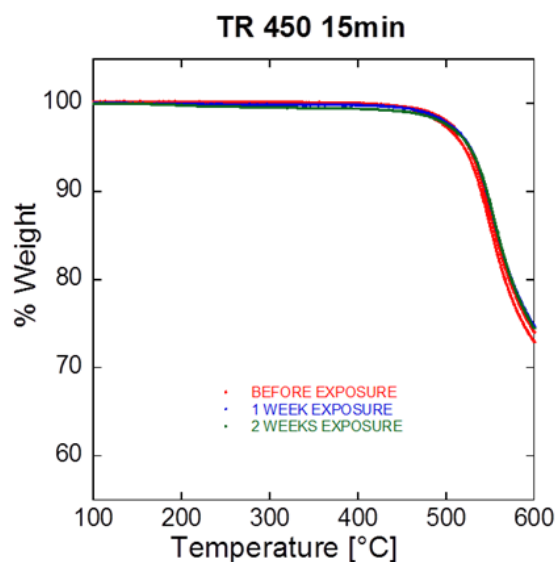


Figure 9.31: Exposure effect on chemical stability of APAF ODPA TR 450 15 min

Bibliography

- [1] American energy: The renewable path to energy security, 2006.
- [2] The energy independence and security act, 2007.
- [3] The madness of biofuel. *Deforestation diesel*, 2011.
- [4] R. W. Baker, J. G. Wijmans, and Y. Huang. Journal of membrane science. 348, 2010.
- [5] R.W. Baker. *Membrane Technology and Applications*. Wiley, 2nd edition, 2004.
- [6] J.L. Bravo. Hydrocarbon proc. jan. page 91, 1985.
- [7] N.B. Colthup, Daly L.H., and S.E. Wiberley. *Introduction to Infrared and Raman Spectroscopy*. Academic Press, United States of America, 3rd edition, 1990.
- [8] J. Crank. *The Mathematics of Diffusion*. Oxford University Press, Oxford, 2nd edition, 1975.
- [9] J.R. Fair. Chem. eng. prog. nov. page 78, 1977.
- [10] J.R. Fair. Chem. eng. prog. jan. page 19, 1990.

-
- [11] Xianshe Feng and Robert Y.M. Huang. Industrial engineering chemical research. 36:1048–1066, 1997.
- [12] J. Gmehling, U. Onken, and W Arlt. *Vapor-liquid Equilibrium Data Collection*. Dechema, Frankfurt, 1st edition, 1977.
- [13] O.R. Inderwildi and D.A. King.
- [14] Lan Ying Jiang, Yan Wang, Tai-Shung Chung, Xiang Yi Qiao, and Jun-Yih Lai. Progress in polymer science. 34:1135–1160, 2009.
- [15] K. K. Okamoto, N. Tanihara, H. Watanabe, K. Tanaka, H. Kita, A. Nakamura, Y. Kusuki, and K. Nakagawa. Journal of chemical engineering of japan. 25:388–396, 1992.
- [16] R. Katzen. Chem. eng. nov. page 209, 1955.
- [17] R Katzen. *Low energy distillation systems. Bio-Energy Conference*. Atlanta, GA, United States of America, 1990.
- [18] Raphael Katzen. Grain motor fuel alcohol technical and economic assessment study, 1978.
- [19] Mark Kinver. Biofuels look to the next generation, 2006.
- [20] W. Kujawski. Polish journal of environmental studies. 9:13–26, 2000.
- [21] F.O. Lichts. Industry statistics: 2010 world fuel ethanol production, 2011.
- [22] S. et al Lynn. Ind. & eng. chem. 25, 1986.
- [23] R. L Martin. Hydrocarbon proc. page 149, 1970.

- [24] S Matsui and D. R. Paul. *Journal of membrane science*. 195, 2002.
- [25] T.J. et al Mix. *Chem. eng. prog.* page 49, 1978.
- [26] Kanji Nakagawa, Yoshio Asakura, Shunsuke Nakanishi, Harutoshi Hoshino, Hiroyuki Kouda, and Yoshihiro Kusuki. *Kobunshi robunshu*. 46:405–411, 1989.
- [27] K. Okamoto, N. Tanihara, H. Watanabe, K. Tanaka, H. Kita, A. Nakamura, Y. Kusuki, and Nakagawa K. *Journal of membrane science*. 68:53–63, 1992.
- [28] Ho Bum Park, Chul Ho Jung, Young Moo Lee, Anita J. Hill, Steven J. Pas, Stephen T. Mudie, Elizabeth Van Wagner, Benny D. Freeman, and David J. Cookson. *Science*, 318, 2007.
- [29] C. C. Pereira, C. P. Ribeiro, R. Nobrega, and C. P. Borges. *Journal of membrane science*. 274, 2006.
- [30] Wulin Qiu, Madhava Kosuri, Fangbin Zhou, and William J. Koros. *Journal of membrane science*. 327:96–103, 2009.
- [31] C. P. Ribeiro and Borges C. P. *Brazilian journal of chemical engineering*. 21, 2004.
- [32] C.P. Ribeiro and C.P Borges. *Brazilian journal of chemical engineering*. 21:629–640, 2004.
- [33] Robinson and Gilliland. *Elements of Fractional Distillation*.
- [34] S. I. Semenova. *Journal of membrane science*. 231, 2004.

-
- [35] B. Smitha, D. Suhanya, S. Sridhar, and M. Ramakrishna. *Journal of membrane science*. 241, 2004.
- [36] B. Smitha, D. Suhanya, S. Sridhar, and M. Ramakrishna. *Journal of membrane science*. 241:1–21, 2001.
- [37] G.L. Tullos and L.J. Mathias. *Polymer*. 40, 1999.
- [38] J.G. Wijmans and R.W. Baker. *Journal of membrane science*. 79:101–113, 1993.
- [39] Yexin Xu, Cuixian Chen, and Jiding Li. *Chemical engineering science*. 62:2466–2473, 2007.